AN EXPERIMENTAL MULTI-SCALE ASSESSMENT OF MECHANICAL PROPERTIES OF ORGANIC-RICH MUDROCKS, AND IMPACT OF THE VARIABILITY OF THEIR MINERALOGICAL AND ORGANIC COMPONENTS IN THEIR MECHANICAL ANALYSIS

A Dissertation

by

CLOTILDE RAQUEL CHEN VALDES

Submitted to the Office of Graduate and Professional Studies of
Texas A&M University
in partial fulfillment of the requirements for the degree of

DOCTOR OF PHILOSOPHY

Chair of Committee,	Zoya Heidari
Co-Chair of Committee,	Robert Lytton
Committee Members,	Walter Ayers
	Eduardo Gildin
Head of Department,	Valerie Taylor

August 2017

Major Subject: Interdisciplinary Engineering

ABSTRACT

Reliable evaluation of rock mechanical properties in organic-rich mudrocks is challenging due to their heterogeneity, anisotropy, and complex lithology. It is important to assimilate variable elastic properties and distribution of individual mudrock components, as well as rock fabric in the evaluation of elastic properties of organic-rich mudrocks. Failure to take into consideration their physical and mechanical properties, can result in unreliable geomechanical characterization for wellbore studies and stress prediction for completions design.

The objectives of this dissertation are to (a) investigate the impact of anisotropic poroelastic parameters for stress prediction in organic-rich mudrocks; (b) quantify the uncertainties involved in well-log-based evaluation of effective elastic properties of mudrocks using micro-scale mechanical testing; and (c) evaluate the impacts of thermal maturity on elastic properties of kerogen and on effective elastic properties of mudrocks.

First, I demonstrated that a thorough depth-by-depth estimation of anisotropic poroelastic parameters is required to estimate stress profile for organic-rich mudrocks. I observed variabilities of up to 30% in estimates of minimum horizontal stress due to vertical heterogeneity, mechanical anisotropy and anisotropic poroelasticity assumptions in organic-rich formations. Next, I evaluated the uncertainties involved in the assessment of effective elastic properties of organic-rich mudrocks. I used nanoindentation tests to quantify the variability in elastic properties of individual rock components, caused by differences in their spatial distribution, size, and rock fabric within the formation. I reported a variability of 25% in Young's moduli of clay minerals due to their location

within the mudrock. I also quantified differences up to 33% between estimates of elastic stiffness coefficients from core measurements and well-log-based estimates of effective elastic stiffness coefficients obtained from nanoindentation tests. Finally, I demonstrated that elastic properties of kerogen vary as the thermal maturity of the formation changes. I evaluated the impacts of thermal maturity on elastic properties of kerogen at the micron-scale by using synthetic thermal maturation. I reported differences of up to 44% in magnitudes of Young's moduli of kerogen at different levels of thermal maturity. Furthermore, I observed that effective elastic properties of the formation varied up to 25% as thermal maturity of kerogen changes from room temperature to 425ºC.

DEDICATION

To my mother, Elia Valdes Camargo, for her unconditional love and support.

To my role model and mentor, Bishop Carlos María Ariz CMF, in memoriam. Thank you for making my education a reality.

ACKNOWLEDGEMENTS

My sincere gratitude goes to my supervisor and chair of my dissertation committee, Dr. Zoya Heidari. Her motivation, generosity and unconditional support inspired me to continue pursuing every goal set throughout my doctoral studies. I would like to give special thanks to my committee co-chair Dr. Robert Lytton. His enthusiasm, selflessness and expertise motivated me to gain interest in the field of micromechanics, since I was a student in the field of soil mechanics. I would also like to express my sincere gratitude to Dr. Eduardo Gildin for serving on my Masters of Science and Doctor of Philosophy committees. I would like to thank Dr. Walter Ayers for sharing his expertise in unconventional formations, for his insightful feedback during the course of my PhD; and for serving on my committee.

I would like to thank my teammates in the Multi-Scale Formation Evaluation research group at Texas A&M for their friendship and support throughout these years. Special gratitude to Alvaro Aranibar, Aderonke Aderibigbe, Mehrnoosh Saneifar and Angie Yang for their collaboration and technical contribution in our joined research efforts. I also thank the associate editors and anonymous reviewers of the Interpretation and Geophysics journals, for their insightful feedback on my research.

A special note of gratitude goes to John Maldonado, for his great support in my experimental work during my master and doctoral degrees. Thanks to Eleanor Schuler, John Winkler, and Sarah Morgan for their availability and support with administrative matters at Texas A&M University. I acknowledge W.D. Von Gonten Laboratories for facilitating the use of their instruments to complete the work presented in this

dissertation. Special thanks to Mr. Nicholas Nelson, Mr. Eric Carter, and Mr. Steve Mraz, for their technical support in SEM imaging, geochemistry and mechanical testing, respectively at their facilities.

My summer internship at Chevron USA, with the Energy Technology Company was a valuable experience that helped me develop in the area of petrophysics and rock physics. I appreciate my supervisor Emmanuel Toumelin, and my mentor Kurt Hilarides, for their time and this enriching opportunity.

I would like to express gratitude to the sponsors of the research conducted in this dissertation. The work reported was supported by the Joint Industry Research Program on Multi-Scale Formation of Unconventional and Carbonate Reservoirs at Texas A&M. I am also grateful to the Unconventional Resources Special Interest Group (URSIG) from the Society of Petrophysicists and Well Log Analysts (SPWLA) for awarding me a scholarship during my doctoral studies. I would also like to thank SPWLA for selecting me as a Distinguisher Speaker for the 2015-2016 period, and for providing the travel funds to present my research to local SPWLA chapters.

CONTRIBUTORS AND FUNDING SOURCES

Contributors

This work was supported by a dissertation committee consisting of Professors Zoya Heidari, Walter Ayers and Eduardo Gildin of the Department of Petroleum Engineering, and Professor Robert Lytton of the Department of Civil Engineering.

All other work conducted for this dissertation was completed by me independently.

The nanoindentation experiments completed in Chapters III and IV were carried out at the W.D. Von Gonten Laboratories facilities by me. The kerogen resistivity measurements displayed in Chapter IV were performed by Angie Yang.

Funding Sources

Graduate study was supported by the Joint Industry Research Program on Multi-Scale Formation of Unconventional and Carbonate Reservoirs at Texas A&M, formed by Aramco Services Company, BHP Billiton, BP, Chevron, ConocoPhillips, and Devon Energy. The Unconventional Resources Special Interest Group (URSIG) from the Society of Petrophysicists and Well Log Analysts (SPWLA) also supported this dissertation with a scholarship.

NOMENCLATURE

C_{ij}	Elastic Stiffness Coefficients of Compliance Tensor, GPa
C_{ij}^{eff}	Effective Elastic Stiffness Coefficients Tensor, GPa
C_{ij}^{0}	Effective Elastic Stiffness Tensor of Isotropic Background in Eshelby-Cheng Effective Model, GPa
C_{ij}^{1}	Modified Effective Elastic Stiffness Tensor of Isotropic Background in Eshelby-Cheng Effective Model, GPa
E	Young's Modulus from Nanoindentation Tests, GPa
E_{eff}	Effective Young's Modulus of the Formation
E_{eff_ht}	Effective Young's Modulus of the Formation (Heat-treated Samples)
E_{eff_nht}	Effective Young's Modulus of the Formation (Non Heat-treated Samples)
$E_{kerogen}$	Young's Modulus of Kerogen, GPa
E_H	Young's Modulus in the Direction Parallel to the Bedding Plane, GPa
E_{pack}^{V}	Upper Voigt Bound for Young's Modulus of the Kerogen Pack
E_{test}^{R}	Measured Young's Modulus of the Kerogen Pack after Pyrite

	Removal, GPa
E_{pyrite}	Young's Modulus of Pyrite
E_V	Young's Modulus in the Direction Normal to the Bedding Plane, GPa
$f_{kerogen}$	Volumetric Concentration of Kerogen
$f_{kerogen}^{*}$	Fractions of Pyrite and Kerogen in Micro- CT Images
f_{pyrite}	Volumetric Concentration of Pyrite
H	Hardness, GPa
K	Bulk Modulus, GPa
K_0	Earth stress coefficient
K_i	Bulk modulus of component *i*, (GPa)
$K_{kerogen}$	Bulk Modulus of Kerogen, GPa
K_s	Grain bulk modulus, (GPa)
K^*_{sc}	Rock Effective Bulk Modulus, GPa
N	Total number of Rock Components
P_p	Pore pressure, (kPa)
P^{*i}	Shape Factor for Component *i*
Q^{*i}	Shape factor for component *i*

V_f	Drilling fluid velocity
$V_p(0^o)$	P-wave velocity parallel to the bedding plane, (m/s)
$V_p(90^o)$	P-wave velocity normal to the bedding plane, (m/s)
$V_s(0^o)$	S-wave velocity parallel to the bedding plane, (m/s)
$V_s(90^o)$	S-wave velocity normal to the bedding plane, (m/s)
W_e	Recoverable Work
W_p	Non-recoverable Work
W_t	Total Work
V_T	Stoneley-wave velocity, (m/s)
α	Aspect Ratio for Spherical Inclusions in Eshelby-Cheng Model.
α_h	Biot's parameter of effective stress in the horizontal direction
α_v	Biot's parameter of effective stress in the vertical direction
x_i	Volumetric Concentration of Rock Component *i*
δ	Thomsen parameter of anisotropy
$\phi_{k,pack}$	Porosity in the Compacted Kerogen Pack
v	Poisson's Ratio from Nanoindentation
v_h	Poisson's Ratio in the Direction Parallel to the Bedding Plane

v_v	Poisson's Ratio in the Direction Normal to the Bedding Plane
v	Poisson's Ratio from Nanoindentation Tests
μ	Lamé Constant
μ_i	Shear Modulus of Rock Component *i*, GPa
$\mu_{kerogen}$	Shear Modulus of Kerogen, GPa
μ^*_{sc}	Rock Effective Shear Modulus, GPa
σ_h	Minimum horizontal stress, (kPa)
σ_h'	Horizontal effective stress, (kPa)
σ_v	Overburden stress, (kPa)
σ_v'	Vertical effective stress, (kPa)
ρ	Bulk density, (g/cc)
ρ_f	Drilling fluid density, (g/cc)

ACRONYMS

AFM	Atomic Force Microscopy
ECS	Elemental Capture Spectroscopy
EDS	Energy Dispersive Spectroscopy
GR	Gamma Ray
HCl	Hydrochloric Acid
HI	Hydrogen Index
HF	Hydrofluoric Acid
LVDT	Linear Displacement Variable Transformer
Micro-CT	X-Ray Micro Computed Tomography
PEF	Photoelectric Factor
SCA	Self-Consistent Approximation
SE	Secondary Electron
SEM	Scanning Electron Microscopy
TEM	Transmission Electron Microscopy
TOC	Total Organic Content

VTI	Vertical Transverse Isotropy
XRD	X-Ray Diffraction
XRF	X-Ray Fluorescence

TABLE OF CONTENTS

Page

LIST OF FIGURES

Page

LIST OF TABLES

Page

CHAPTER I

INTRODUCTION

This dissertation introduces a new method to assess elastic properties in organic rich mudrocks that uses experimental schemes at multiple scale levels of investigation, for improving fracture treatment. This dissertation introduces a workflow that enhances the assessment of anisotropic elastic and poroelastic properties in organic-rich mudrocks by using laboratory methods. It presents a new technique that uses experimental methods at the micro-scale level of investigation for multi-scale characterization of elastic properties in organic-rich mudrocks. Finally, it reports the impact of thermal maturity of kerogen on elastic properties of organic-rich mudrocks.

1.1 Background

Complex mineralogy, high organic content, and heterogeneity are characteristics in organic-rich formations, which impact their mechanical properties when evaluated in the elastic range of deformation. An adequate evaluation of mechanical properties in organic-rich mudrocks can help improve geomechanical evaluation for fracture treatment performance, which could ultimately result in favorable economic production in these formations. At the well log-domain, a major challenge in the assessment of elastic properties in organic-rich mudrocks is the evaluation of poroelastic parameters. Assuming isotropy in poroelastic parameters or assuming them equal to unity leads to uncertainties in stress estimates for fracture design. Furthermore, the evaluation of

elastic properties of individual mudrock components (i.e. minerals and organic matter) remains a challenge. The variability in estimates of elastic properties of individual mudrock components could lead to high uncertainties in estimates of effective elastic properties at the well-log domain. A good understanding of the mechanical properties at the micro-, core- and well-log domain could potentially improve mechanical characterization in organic-rich mudrocks for stress prediction.

1.2 Stress Prediction in Organic-Rich Mudrocks

Stress prediction is used to estimate the state of stress in the formation to design fracture stimulation, or in geomechanical applications such as pore pressure prediction and wellbore stability. The main stresses (minimum and maximum) are required to estimate hydraulic fracture propagation growth and initiation stress. Stress estimates are often performed using mechanical earth modelling under assumptions of a state of failure or elasticity. Failure models assume that the formation is in a state of shear failure equilibrium. The elastic models assume that the formation is in the elastic regime of deformation. Hence, elastic models are widely used for stress prediction; since elastic properties at the well-log domain can be obtained either from wireline data of acoustic logs or core measurements (Thiercelin and Plumb, 1994). In organic-rich mudrocks, however, stress prediction remains challenging due to their complex lithology. Alignment of clay minerals and laminations (Sayers, 2013), in addition to natural fractures, induce strong acoustic and mechanical anisotropy. These traits are noticeable at well-log and pore-scale domains, which widely impacts stress prediction in organic-rich mudrocks. An existing limitation with elastic models is the error involved in stress

estimates, which could be introduced either by estimates of elastic properties, pore pressure, poroelastic properties and horizontal strains that are used as inputs for the geomechanical models. Core measurements are often used to measure elastic and poroelastic parameters. Measuring poroelastic parameters is challenging at the core-scale in organic-rich mudrocks due to factors such as difficulty monitoring pore pressures and achieving a state of fluid equilibrium within the core sample. Furthermore, core availability from depths of interests is commonly challenging due to low core recovery. Mechanical tests at the micro-scale are often more flexible due to the small volumes of mudrocks required that facilitates a more massive sampling. Therefore, assessment of mechanical properties at the micro-scale, core-scale and well-log domains can improve stress prediction in these formations.

1.3 Statement of the Problem

Reliable evaluation of rock mechanical properties is challenging in organic-rich mudrocks. It is required for geomechanical modelling and to achieve successful fracture treatments. However, traits observed in organic-rich mudrocks, such as heterogeneity, anisotropy, and their complex lithology introduces uncertainties that could potentially cause unreliable stress prediction and failure in completions design. In this dissertation, I propose using experimental methods at the micro- and core-scale, in addition to well-log-scale methods, to estimate elastic properties in organic-rich mudrocks at the well-log domain after petrophysical analysis.

In the well-log domain, to address the variability involved in stress estimates in organic-rich mudrocks using elastic models, I include the use of anisotropic

poroelasticity in the stress estimates workflow. This workflow uses a simplification of the three-dimensional orthotropic Biot's theory of poroelasticity for fractured-media, which resemble the effects of an organic-rich layered formation, geometrically represented as a transversely isotropic formation in the vertical axis of symmetry. Use of the simplified theory of anisotropic poroelasticity can potentially help to improve stress estimates using a combination of acoustic well logs and rock physics models, when there formation testing data is not available to estimate in-situ stresses.

In the next section of this dissertation, I report the use micro-scale mechanical tests to quantify the variability of elastic properties of individual rock components (i.e. minerals and kerogen). I used instrumented nanoindentation tests to measure and quantify the variability in elastic properties of rock components, according to their spatial distribution and size, at the micro-scale domain. Quantifying the variability of elastic properties of individual mudrock components enables better estimates of well-log-based elastic properties of mudrocks that are based on rock physics models and lithology composition.

Finally, I investigate the effects of thermal maturation in elastic properties of kerogen. I use heat-treated samples of compacted kerogen powder extracted from four different mudrock formations, to investigate the impact of thermal maturation in effective elastic properties of the formation using joint interpretation of acoustic and conventional well logs. Investigating the effects of thermal maturation on elastic properties of kerogen can help clarify the variability of elastic properties of kerogen at different levels of thermal maturation.

1.4 Research Objectives

The motivation of this dissertation resides on the need to enhance evaluation of mechanical properties of mudrocks to increase accuracy of stress estimates, when limited information is available for geomechanical analysis in mudrocks. Hence, I encompass three main objectives for this dissertation. The first objective suggests the mechanical coupling of solid, fluid, and pore space by applying anisotropic poroelasticity in mudrock formations. The second objective addresses the variability involved in estimates of elastic properties of mudrock components, and the effect of these uncertainties in well-log based evaluation of effective elastic properties. The last objective addresses the variability on mechanical properties of kerogen at different levels of thermal maturation and the impact of this variability in estimates of elastic properties in mudrocks with high organic content.

The three objectives for this dissertation are explained in detail as follows:

1. Improve elastic models for the assessment of minimum horizontal stress in organic-rich mudrocks. The methods to fulfill this goal include:
    a. Conduct direct measurements earth stress coefficient, K_0, in the geomechanical analysis for organic-rich mudrocks.
    b. Evaluate Biot's anisotropic poroelasticity parameters in formations with different degrees of mechanical anisotropy and heterogeneity.
    c. Investigate the validity of the ANNIE approximation model (Schoenberg et al., 1996) in organic-rich mudrocks, using

correlations of anisotropic elastic stiffness coefficients in formations where the anisotropy approximations are not valid.

2. Introduce an experimental multi-scale approach for variability assessment of elastic properties in organic-rich mudrocks. The methods to fulfill this approach includes:
    a. Conduct nanoindentation mechanical tests on rock samples obtained from two mudrock formations, to measure Young's modulus of individual and mixtures of rock components
    b. Quantify the variability of elastic properties in each mudrock component due to factors such as location in the rock sample, adjacent minerals, and particle size.
    c. Quantify the variability in well-log-based estimates of effective elastic properties of the rock, caused by variation in elastic properties of individual rock components at the micron-scale.
3. Investigate the impact of thermal maturity in elastic properties of kerogen. The methods to accomplish this objective include:
    a. Carry out nanoindentation tests in compacted kerogen samples, at four different levels of synthetic thermal maturation.
    b. Measure elastic properties of isolated kerogen samples at the micro-scale level of investigation, to evaluate the variability of elastic properties caused by chemical and structural changes due to thermal maturity.

c. Investigate the effects of the variability in elastic properties of kerogen due to thermal maturation in effective elastic properties of mudrocks with high organic content.

1.5 Method Overview

The following sections describe the methods applied to fulfill the three main objectives of this dissertation at the well-log, multi- and micro-scale domains of investigation for elastic properties.

1.5.1 Well-log domain: Impact of anisotropic poroelastic parameters and anisotropic model approximations on stress predictions in organic-rich mudrocks

Figure 1.1 shows the workflow for the study of the impact of anisotropic poroelastic parameters and anisotropic model approximations on stress predictions in organic-rich mudrocks. In the experimental method, I performed uniaxial strain tests and triaxial stress tests at the core-scale to estimate static and dynamic elastic stiffness coefficients and anisotropy poroelastic parameters. Well logs and geomechanical properties obtained at the core scale were then used to estimate dynamic elastic stiffness coefficients and compositional properties, to further carry out stress prediction.

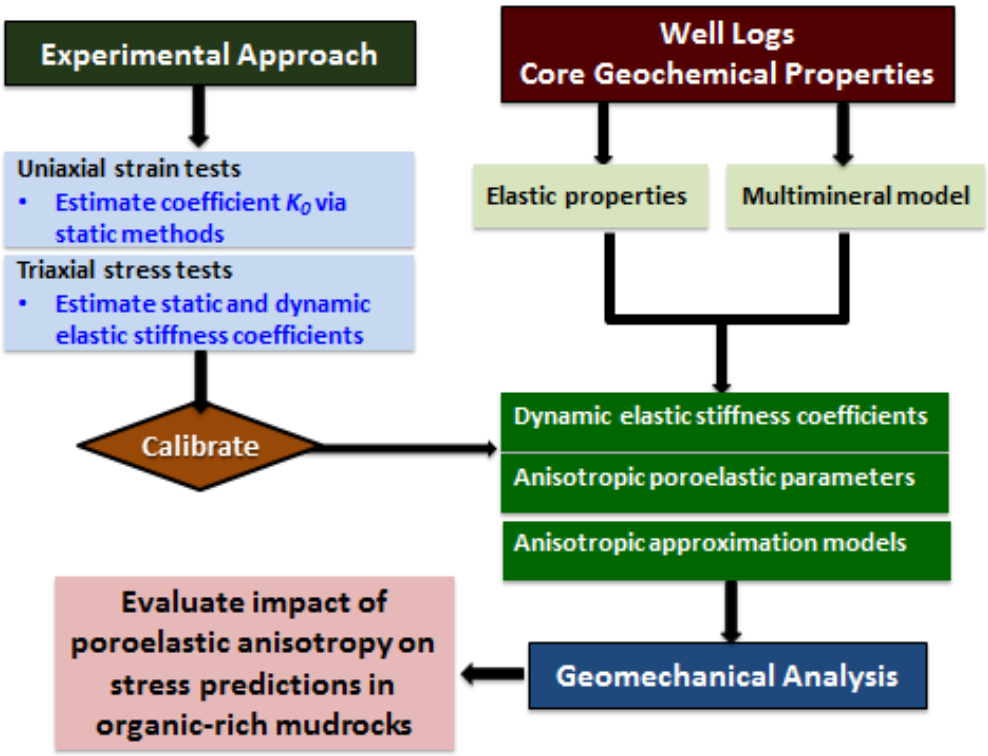

Figure 1.1: Workflow for the study of the impact of anisotropic poroelastic parameters and anisotropic model approximations on stress predictions in organic-rich mudrocks.

1.5.2 Multi-scale domain: Application of nanoindentation for variability assessment of elastic properties in mudrocks at the micro-scale and well-log domains

Figure 1.2 shows the workflow for the application of nanoindentation for variability assessment of elastic properties in mudrocks at the micro-scale and well-log domains. Experiments were performed at the micro-scale in order to measure and quantify the variability of elastic properties in (a) individual mudrock components and (b) mixtures of mudrock components. The measurements performed at the micro-scale were then used as inputs to estimate effective elastic properties of the formation at the well-log domain.

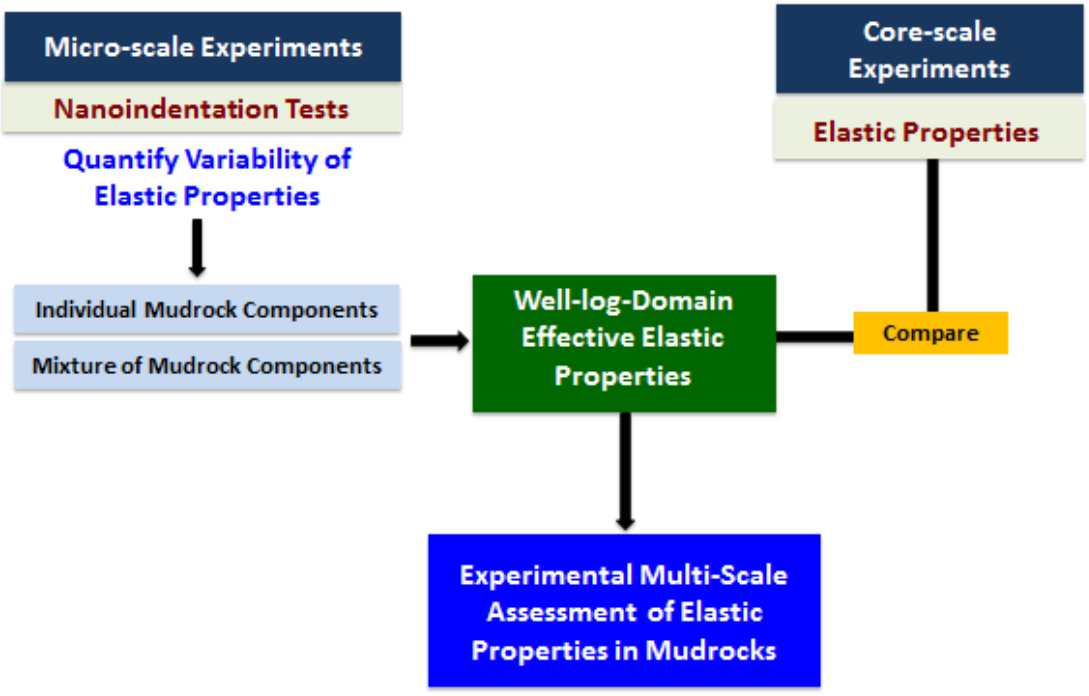

Figure 1.2: Workflow used for the application of nanoindentation for variability assessment of elastic properties in mudrocks at the micro-scale and well-log domains

1.5.3 Micro-scale domain: Impact of thermal maturation in elastic properties of kerogen

Figure 1.3 shows the workflow for the study of the impact of thermal maturation in elastic properties of kerogen. I used isolated and synthetically-matured kerogen to measure their mechanical properties at the micro-scale domain, via nanoindentation. Compositional properties at the well-log domain were then used to estimate effective elastic properties of the formation. Then, I performed sensitivity analysis to quantify the impact of the variability of elastic properties of kerogen on effective elastic properties of the formation due to the different levels of thermal maturation.

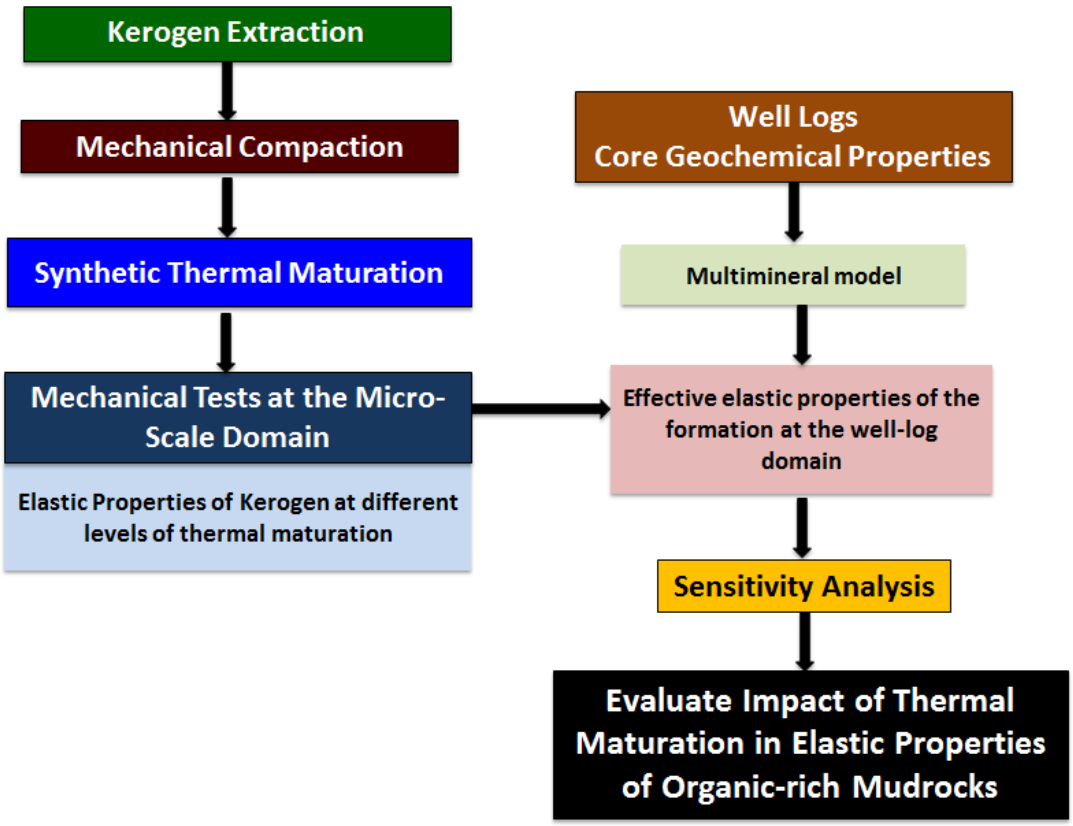

Figure 1.3: Workflow for the study of the impact of thermal maturation on elastic properties of kerogen

1.6 Outline of This Dissertation

This dissertation is divided into five chapters. Chapter I consists of the background of this investigation, literature review and a brief overview of the methods used to complete the objectives defined for this research.

Chapter II focuses on improving the assessment of minimum horizontal stress in organic-rich mudrocks by considering different levels of (a) vertical heterogeneity and (b) mechanical anisotropy in mudrock formations. The improved workflow is applied to field examples from the lower Eagle Ford, Haynesville, and upper Wolfcamp formations.

Chapter III introduces a multi-scale approach to estimate effective elastic properties at well-log domain in organic-rich mudrocks. This approach includes the use of measurements of elastic properties at the micro-scale domain. This chapter also focuses on quantification of the variability of effective elastic properties caused by factors such as size of mudrock components and location of the components.

Chapter IV introduces a novel technique to evaluate the impact of thermal maturation in mechanical properties of kerogen. This technique measures the variability of elastic properties of type II and III kerogen samples, at different levels of thermal maturation. Furthermore, I perform a sensitivity analysis to quantify the impact of variation in elastic properties of kerogen due to thermal maturity, on effective elastic properties of organic-rich mudrocks.

Chapter V presents the conclusions of this dissertations, current limitations, and future recommendations.

CHAPTER II

IMPACT OF ANISOTROPIC POROELASTIC PARAMETERS AND ANISOTROPIC MODEL APPROXIMATIONS ON STRESS PREDICTIONS IN ORGANIC-RICH MUDROCKS[*]

The evaluation of rock mechanical properties in organic-rich mudrocks is challenging due to their heterogeneity, anisotropy, and complex lithology. Hence, geomechanical analysis should include a complete definition of the anisotropic elastic stiffness coefficients for stress prediction. Furthermore, typical assumptions made for poroelastic parameters, such as assuming that Biot's parameter of equal to unity can result in unreliable geomechanical evaluation for stress prediction and failure in completion design. In this section, I introduced an improved assessment of minimum horizontal stress by (a) obtaining laboratory anisotropic elastic properties to validate and enhance the assessment of those drawn from well logs (b) evaluating Biot's anisotropic poroelasticity parameters in formations with different degrees of mechanical anisotropy and heterogeneity, and (c) investigating the validity of vertical transverse isotropy (VTI) approximation models in organic-rich mudrocks. The techniques used in this section include performing static and dynamic mechanical tests on core plugs, analyzing advanced acoustic well logs, estimating dynamic elastic stiffness coefficients in different

[*] Reprinted with permission from "Impact of anisotropic poroelastic parameters estimated using well logs and core measurements on stress prediction in organic-rich mudrocks" by Clotilde Chen Valdes, et al., 2016. Interpretation, 4, T359-T372, Copyright 2016 by the Society of Exploration Geophysicists and American Association of Petroleum Geologists.

mudrock formations and estimating stress profile under the assumption of transverse isotropy.

The improved assessment was applied in the lower Eagle Ford, Haynesville, and upper Wolfcamp formations, to quantify the effects of poroelastic parameters and the choice of the VTI approximation models on the estimates of minimum horizontal stresses. The results confirmed that transversely isotropic media require a thorough depth-by-depth estimation of anisotropic poroelastic parameters to estimate stress profile accurately. Furthermore, I also demonstrated in this section the importance of integrated interpretation of petrophysical, compositional, and mechanical properties in geomechanical evaluation in organic-rich mudrocks.

2.1 Introduction

Mudrocks can be classified as siltstone, mudstone, claystone, silt-shale, mud-shale, and clay-shale, depending on particle size and fissility (Stow, 1981; Horne, 2013). Evaluating rock mechanical properties in organic-rich mudrocks remains challenging and ambiguous because of their complex lithology and heterogeneity. The alignment of clay minerals and lamination of organic materials leads to strong anisotropy in organic-rich mudrocks (Sayers, 2013). These characteristics are inherent in lateral and vertical directions, at both the pore and the reservoir scale. They consequently influence rock elastic properties, and can, therefore, significantly impact stress prediction in organic-rich mudrocks. Furthermore, stress prediction plays a key role in wellbore stability, hydraulic fracture design, and completion optimization and design (Song and Hareland, 2012; Li and Purdy, 2010; Sebastian et al., 2015).

Stress prediction is conducted in reservoir geomechanics by using mechanical earth models under assumptions of either failure or elasticity. The failure model assumes that rocks are in an equilibrium state of shear failure, and requires core measurements in the non-elastic deformation regions. In the elasticity model, the parameters required for stress prediction can be obtained either from wireline or core measurements (Thiercelin and Plumb, 1994). As a result, the elasticity model is most commonly used for stress prediction in formations consisting of organic-rich mudrocks. The presence of laminations of organic material and partial alignment of plate-like clay minerals result in anisotropy in organic-rich mudrocks (Sayers, 2013). Therefore, the elastic properties in these rocks vary in the directions parallel and normal to the bedding plane (Amadei, 1988). Transverse isotropy symmetry has been applied in previous publications to describe the anisotropy in organic-rich mudrocks (Sayers, 1994). In transverse isotropy, the medium is characterized by the same properties in one plane (i.e., a single plane of isotropy), and different properties in the direction normal to the isotropy plane.

Several studies (Higgins et al., 2008; Waters et al., 2011; Song and Hareland, 2012) have estimated the minimum horizontal stress in formations exhibiting anisotropy by using the vertical transverse isotropy (VTI) model. The equilibrium equation (Thiercelin and Plumb, 1994) that takes into account pore pressure, overburden stresses, horizontal stresses, horizontal strains, and anisotropic elastic properties, is commonly used in the estimation of minimum horizontal stress assuming VTI. The conventional workflow applied in the estimation of minimum horizontal stress includes the use of acoustic logs to determine anisotropic elastic properties, as well as the application of

approximation models. Approximation models such as the ANNIE (Schoenberg, et al., 1996) and modified ANNIE models (Suarez-Rivera and Bratton, 2009; Quirein, et al., 2014), are commonly applied to estimate the five elastic stiffness coefficients required to define completely a VTI medium. Some shortcomings of the conventional workflows include the validity of the VTI approximation models in the formations being investigated, and the assumption that Biot's poroelastic parameter is equal to one.

Biot (1955) extended the isotropic theory of poroelasticity to anisotropic cases, resulting in more than one independent poroelastic parameter. Cheng (1997) introduced a simplification for transversely isotropic formations that assumes a state of micro-homogeneity and micro-isotropy. Cheng (1997) also stated that the poroelastic parameters are properties of the solid constituents exclusively, and defined the vertical and horizontal poroelastic parameters α_h and α_v, respectively. Researchers often assume these poroelastic parameters to be either equal to each other, or equal to one. Poroelastic parameters near or equal to one are characteristic of geomaterials that are highly compressible (low bulk modulus), such as soil and soft rocks. For less compressible rocks, especially in the presence of high pore pressures, these coefficients can vary significantly (Shafer et al., 2008). Therefore, these parameters should be taken into account when the formation is overpressured, and when the effective stresses are dominated by pore pressure, such as in passive margin basins (Dix et al., 2010; Hammes et al., 2011). Incorporating the anisotropic poroelastic effect into the transversely isotropic elastic model can potentially improve stress prediction in organic-rich mudrocks.

The objective of this chapter is to improve the assessment of minimum horizontal stress in organic-rich mudrocks by taking into account different levels of vertical heterogeneity and mechanical anisotropy of the formation. I applied the improved workflow for estimates of minimum horizontal stresses in the lower Eagle Ford, Haynesville, and upper Wolfcamp formations.

2.2 Method

The improved assessment of minimum horizontal stress includes: (a) measuring directly earth stress coefficient, K_0, in the geomechanical analysis for organic-rich mudrocks, (b) evaluating Biot's anisotropic poroelasticity parameters in formations with different degrees of mechanical anisotropy and heterogeneity, and (c) investigating the validity of the ANNIE approximation model in organic-rich mudrocks, using correlations of anisotropic elastic stiffness coefficients in formations where the anisotropy approximations are not valid. I conducted rock mechanical laboratory measurements under triaxial stress and uniaxial strain conditions on core plugs from organic-rich mudrocks, to obtain both static and dynamic elastic properties (i.e., Young's modulus and Poisson's ratio). I also analyzed well logs to estimate the volumetric concentrations of the minerals, and the anisotropic elastic stiffness coefficients of the three formations under investigation. The volumetric concentrations of minerals and the elastic stiffness coefficients serve to generate the anisotropic poroelastic parameters. Finally, I performed stress prediction under assumption of transverse isotropy, including the estimated anisotropic elastic properties and poroelastic parameters.

2.2.1 Review of assessment of elastic stiffness coefficients

The transverse isotropy model requires five independent elastic stiffness coefficients- C_{33}, C_{44}, C_{11}, C_{66} and C_{13}, to assess minimum horizontal stress. Stiffness coefficients C_{33}, C_{44}, C_{11}, and C_{66} can be obtained from triaxial tests on vertical (cored normal to the bedding plane) and horizontal (cored parallel to the bedding plane) rock samples through laboratory geomechanical measurements. C_{13} can be obtained from triaxial tests on samples cored at 45^{o} to the bedding plane. Coring organic-rich mudrocks at a 45^{o} angle is usually challenging because of their delicate nature. Yan et al. (2012) report a 50% error in assessment of C_{13} with a 5^{o} angle error in the core plugs. Hence, alternative testing methods are required to obtain laboratory measurements of C_{13}. In this study, I use uniaxial strain tests to estimate the earth stress coefficient, K_0, which can be further used to obtain the elastic stiffness coefficient C_{13}. Details of the estimation procedure are explained in the "Experimental assessment of stiffness coefficient" subsection.

Well-log-based methods can only estimate three out of five stiffness coefficients (C_{33}, C_{44}, and C_{66}) from advanced acoustic well logs. The ANNIE approximation model, a simplified anisotropic three-parameter model, is commonly used to estimate the remaining two stiffness coefficients (C_{11} and C_{13}) (Schoenberg et al., 1996). The ANNIE approximation model includes two constraints. In the first constraint, the Thomsen parameter, δ, is assumed to be small in shale formations, and, therefore, is set to zero, which enables the calculation of C_{13} via

$$\delta = \frac{\left(C_{13} + C_{44}\right)^2 - \left(C_{33} - C_{44}\right)^2}{2C_{33}\left(C_{33} - C_{44}\right)} = 0. \tag{2.1}$$

Equation 2.1 can be simplified to

$$C_{13} + 2C_{44} - C_{33} = 0. \tag{2.2}$$

The second constraint assumes that in the case of transversely isotropic formations the following equation is valid

$$C_{13} \equiv C_{12} = C_{11} - 2C_{66}, \tag{2.3}$$

which enables the calculation of C_{11}.

Suarez-Rivera and Bratton (2012) introduced a modified ANNIE approximation model by including additional parameters to obtain the stiffness coefficients C_{11} and C_{13}. In this modified ANNIE approximation model, C_{13} can be obtained by solving

$$C_{13} = \left(C_{33} - \chi C_{44}\right), \tag{2.4}$$

$$C_{13} = \zeta C_{33} - 2C_{44}, \tag{2.5}$$

and,

$$C_{12} = \xi C_{13}. \tag{2.6}$$

Thus, C_{11} can be obtained via

$$C_{11} = \xi\left(\zeta C_{33} - 2C_{44}\right) + 2C_{66}. \tag{2.7}$$

χ represents a characterization parameter determined from acoustic-wave velocities, while ζ and ξ represent characterization parameters obtained from the comparisons of **Equation 2.5** and **Equation 2.6** against core measurements.

Quirein et al. (2014) reported that the ANNIE approximation model predicts the vertical Poisson's ratio, υ_v, to be greater than the horizontal Poisson's ratio, υ_h, which is not always correct for all organic-rich mudrocks. They presented a modification of the ANNIE approximation model equations, which is applicable in the case of organic shales (i.e., for υ_v less than or greater than υ_h). In this modification, Quirein et al. (2014) proposed that the two stiffness coefficients C_{11} and C_{13} can be obtained by solving the sequence of equations given by

$$C_{11} = 1.12\left(2\left(C_{66} - C_{44}\right) + C_{33}\right), \tag{2.8}$$

$$C_{12} = C_{11} - 2C_{66}, \tag{2.9}$$

and

$$C_{13} = 0.76C_{12}. \tag{2.10}$$

The coefficient values of 1.12 and 0.76 are obtained through experiments, performed on core samples from Bakken, Bazhenova, and Niobara shales.

Horne (2013) carried out statistical analysis on a large database of mudrocks to test the validity of the ANNIE and modified ANNIE approximation models. The five-parameter modified ANNIE approximation model (Suarez-Rivera and Bratton, 2012) shows good correlation coefficients when regression techniques are applied to the

samples in the database. The analysis of 745 samples in the database also show that the distribution of Thomsen's parameter, δ, is close to zero. This observation provides an empirical justification for the first constraint in the three-parameter ANNIE approximation model. Hence, the four-parameter approximation model, in which the first constraint in the ANNIE approximation model is retained, can be used to estimate the stiffness coefficients C_{11} and C_{13}.

The next section includes descriptions of the methods used in this dissertation and their application to three field examples located in organic-rich intervals of the lower Eagle Ford, Haynesville, and upper Wolfcamp formations.

2.2.2 Experimental assessment of elastic stiffness coefficients

I improve an existing geomechanical method by including uniaxial strain tests in our interpretation workflow to obtain the earth stress coefficient, K_0. This parameter provides information about the in situ equilibrium state of stresses. The conventional triaxial tests to obtain the elastic stiffness coefficients are made under deformation mechanisms that do not resemble the state of the in situ stresses. K_0 represents the ratio of effective horizontal stress, σ_h', to vertical effective stress, σ_v', at rest conditions, expressed as

$$K_0 = \frac{\sigma_h'}{\sigma_v'}. \tag{2.11}$$

K_0, obtained from the uniaxial strain tests, can be applied to assess C_{13} via

$$K_0 = \frac{C_{13}}{C_{33}}. \tag{2.12}$$

I use only core samples drilled perpendicular to the bedding plane to perform the uniaxial strain tests. I also ensure that the sample is under uniaxial strain conditions (i.e., no radial deformation) by setting the radial strain control to zero. As a result, the confining pressure increases in a manner that prevents the sample from exhibiting lateral deformations.

In the conventional triaxial testing system, an axial load and confining pressures induce strains in core samples. The axial load represents the maximum in situ stress, and the confining pressure represents the intermediate and minimum in situ stresses. The strains in the core samples are measured with two axial and one circumferential linear displacement variable transformers (LVDTs). The top and bottom endcaps contain two piezoelectric compressional- and shear-wave ultrasonic transducers with a 0.2 MHz frequency. I use core plugs drilled in directions parallel and perpendicular to the wellbore orientation from the Haynesville and the upper Wolfcamp formations. I conduct dynamic (using the ultrasonic velocity system) and static triaxial tests on the core samples cut in the two perpendicular directions as described previously. The triaxial tests are performed under drained conditions, using a pore pressure of zero, with a constant axial loading rate of 4.2×10^{-6}/s, up to a maximum axial load of 80 MPa. The confining pressures are set as a function of the depths at which the samples were cored, and are held constant for each core sample during each experiment.

Then I obtain the dynamic stiffness parameters in both cases of vertical (i.e., cored normal to the bedding plane), and horizontal (cored parallel to the bedding plane) cylindrical core samples using compressional- and shear-wave velocities propagated parallel and normal to the bedding planes (Podio et al., 1968, Vernik and Nur, 1990)

$$C_{33} = \rho V_p^{\,2}\left(90^0\right), \tag{2.13}$$

$$C_{44} = \rho V_S^{\,2}\left(90^0\right). \tag{2.14}$$

$$C_{11} = \rho V_p^{\,2}\left(0^0\right), \tag{2.15}$$

and

$$C_{66} = \rho V_S^{\,2}\left(0^0\right). \tag{2.16}$$

where ρ is the bulk density, $V_p(90^o)$ and $V_s(90^o)$ are the compressional- and shear-wave velocities propagated normal to the bedding planes, respectively, and $V_p(0^o)$ and $V_s(0^o)$ are the compressional- and shear-wave velocities propagated parallel to the bedding planes, respectively.

Then I measure the static horizontal Young's modulus, E_h, and the static horizontal Poisson's ratio, υ_h, as well as the static vertical Young's modulus, E_v, and the vertical Poisson's ratio, υ_v. The static elastic properties measured in the vertical and horizontal directions are then converted to static stiffness coefficients by solving the system of equations given by Podio et al. (1968)

$$E_v = C_{33} - \frac{2C_{13}^{\ 2}}{C_{11} + C_{12}}, \tag{2.17}$$

$$E_h = C_{11} + \frac{C_{13}^{\ 2}\left(C_{12} - C_{11}\right) + C_{12}\left(C_{13}^{\ 2} - C_{12}C_{33}\right)}{C_{33}C_{11} - C_{13}^{\ 2}}, \tag{2.18}$$

$$\upsilon_v = \frac{C_{13}}{C_{11} + C_{12}}, \tag{2.19}$$

and

$$\upsilon_h = \frac{C_{33}C_{12} - C_{13}^{\ 2}}{C_{33}C_{11} - C_{13}^{\ 2}}. \tag{2.20}$$

In the next step, I obtain empirical correlations between the estimated dynamic and static elastic stiffness coefficients, estimated from the ultrasonic and static triaxial tests, respectively. Next, I use the static elastic properties to estimate the earth stress coefficient, K_0, which relates Young's moduli and Poisson's ratio parallel and normal to the bedding plane.

$$K_{0\_estimated} = \frac{\upsilon_v E_h}{\left(1 - \upsilon_h\right) E_v}. \tag{2.21}$$

Then I compare the measured K_0, obtained from the uniaxial strain tests, against the K_0 estimated from the elastic properties (i.e., Young's moduli and Poisson ratio), which are obtained from the static triaxial tests.

2.2.3 Well-log interpretation and depth-by-depth assessment of elastic stiffness coefficients

I also conduct well-log interpretation for the assessment of total porosity, water saturation, volumetric concentration of minerals, and organic matter. The input well logs for the petrophysical and compositional evaluation include gamma ray (GR), electrical resistivity, density, neutron porosity, photoelectric factor (PEF), elemental capture spectroscopy (ECS), and compressional-wave slowness. I use the ΔlogR technique (Passey et al., 1990) to estimate the total organic content (TOC). The estimates of mineral concentrations are cross-validated using X-Ray Diffraction (XRD) measurements.

Next, I analyze the density and cross-dipole sonic slowness logs to calculate three of the five dynamic elastic stiffness coefficients C_{33}, C_{44}, and C_{66}. Stiffness coefficients C_{33} and C_{44} are estimated using **Equation 2.13** and **Equation 2.14**. C_{66} is estimated using the Stoneley wave-slowness (Frydman, 2010) via

$$C_{66} = \rho_f \frac{V_T^{\,2}\left(0^o\right) V_f^{\,2}}{V_f^{\,2} - V_T^{\,2}\left(0^o\right)}, \tag{2.22}$$

where V_T is the Stoneley-wave velocity, V_f is the velocity of the drilling fluid, and ρ_f is the drilling fluid density.

I estimate the remaining two dynamic elastic stiffness coefficients, C_{13} and C_{11}, by investigating the validity of the ANNIE approximation model for each of the formations. I evaluate the Thomsen's parameter, δ, to validate the assumption of the first constraint in the ANNIE approximation model. Then I compare the C_{13} estimates

obtained from the ANNIE approximation model to the C_{13} estimates obtained from static measurements, using the core samples from the Haynesville, Eagle Ford, and upper Wolfcamp formations. I apply the ANNIE approximation model in the formations where (a) the estimate of Thomsen's parameter, δ, is small, (b) ANNIE C_{13} estimates are in agreement with the C_{13} static measurements, and (c) υ_v/υ_h is greater than one. In formations where the aforementioned conditions do not apply, I use experimentally-derived correlations between the stiffness coefficients to obtain C_{13} and C_{11}. Static stiffness coefficients are required for mechanical earth modelling (Holt et al. 2013). Hence, I obtained empirical correlations between laboratory-derived dynamic and static elastic stiffness coefficients for well-log-based assessment of static stiffness coefficients.

2.2.4 Well-log-based assessment of anisotropic poroelastic parameters

Biot's poroelastic parameter, α, only approaches the value of one in unconsolidated soils and soft materials. There is significant variability in estimates of this parameter in consolidated porous media. Previous experiments on welded tuff, Indiana limestone, Westerly granite, and low-permeability sandstones (Richin, 1995; Hart, 2000; Chen Valdes, 2013), provide α measurements in the range of 0.27 to 0.96. The Biot's poroelastic parameter can be expressed in terms of the bulk modulus of the rock, K, and the effective grain bulk modulus, K_s, according to the micromechanical approach of the theory of poroelasticity (Detournay and Cheng, 1993),

$$\alpha = 1 - \frac{K}{K_s}. \tag{2.23}$$

The laboratory procedures for direct measurements of K_s require the use of unjacketed tests, in which the confining fluid migrates into the pore space of the core sample, and the deformations are measured in the solid phase instead of the bulk rock. The deformation measurements are made under the assumption that the core sample is fully saturated. It is, however, challenging to achieve the fully saturated and drained conditions in organic-rich mudrock samples. Furthermore, it is challenging to monitor the pore pressure, because the volume of fluid contained in the pore space is small, compared to the dead volume of fluid contained in the hydraulic system.

Because of the uncertainties in the estimation of Biot's poroelastic parameter from laboratory measurements, I carry out well-log-based assessment to obtain this value. The anisotropic Biot's poroelastic parameter can be estimated from the dry rock-stiffness tensor and effective grain bulk modulus, K_s, (Cheng, 1997) via

$$\alpha_h = 1 - \frac{\left(C_{11}{}^d + C_{12}{}^d + C_{13}{}^d\right)}{3K_s} \tag{2.24}$$

and

$$\alpha_v = 1 - \frac{\left(2C_{13}{}^d + C_{33}{}^d\right)}{3K_s}, \tag{2.25}$$

where α_v and α_h represent the vertical and horizontal Biot's poroelastic parameters, respectively, and C_{11}^d, C_{12}^d, C_{13}^d, and C_{33}^d are dry stiffness coefficients. Havens (2012) carried out well-log-based assessment of the Biot's poroelastic parameters in the Bakken formation using **Equation 2.24** and **Equation 2.25**.

In my assessment of Biot's poroelastic parameters, I obtain K_s by applying the elastic Self-Consistent Approximation (SCA) (Berryman, 1995) that falls within the Hashin-Shritkman bounds (Mavko, 2009), described as

$$\sum_{i=1}^{N} x_i \left(K_i - K_{sc}^{*} \right) P^{*i} = 0, \tag{2.26}$$

where N is the total number of rock components i, x_i is volumetric concentration of the i-th rock component, and K_i is the bulk modulus of the rock component i. P^{*i} is a function of the aspect ratios assigned to each rock component. The aspect ratios take into account the shape of different inclusions in the rock and are expressed as

$$P_i^{*} = \frac{1}{3} T^{(i)}_{jjll}. \tag{2.27}$$

The volumetric concentrations of minerals are obtained from the well-log interpretation results. **Table 2.1** lists the assumed bulk moduli for the mineral components.

Table 2.1: Values assumed for bulk moduli of the mineral components in the field examples**.**

Rock Component	K_i **(GPa)**
Calcite	73.3
Dolomite	94.9
K-feldspar	37.5
Plagioclase	76.0
Quartz	37.8
Illite	60.0
Kaolinite	1.5
Chlorite	21.0
Kerogen	2.9
Pyrite	142.7
Apatite	85.4

2.2.5 Assessment of minimum horizontal stress

I estimate minimum horizontal stress, assuming a transversely isotropic formation, via (Thiercelin and Plumb, 1994; Savage et al., 1992)

$$\sigma_h = \alpha_h P_p + \frac{C_{13}}{C_{33}}\left(\sigma_v - \alpha_v P_p\right) + \left(C_{11} - \frac{C_{13}^{\,2}}{C_{33}}\right)\varepsilon_h + \left(C_{12} - \frac{C_{13}^{\,2}}{C_{33}}\right)\varepsilon_H, \tag{2.28}$$

where σ_h is the minimum horizontal stress, σ_v is the overburden stress, P_p is the pore pressure, and ε_h and ε_H are the minimum and maximum horizontal strains, respectively. I integrate the density log to obtain the overburden stress, and assume constant pore pressure gradients. I assume that the formation is under uniaxial strain conditions (i.e., $\varepsilon_h = \varepsilon_H = 0$). The tectonic strains (ε_h and ε_H) can be estimated by

matching the closure stresses observed from field well test analyses, such as minifracture tests, to the stress prediction using geomechanical models.

Furthermore, I compare the estimates of minimum horizontal stress obtained by applying the ANNIE approximation model to those obtained using experimentally-derived correlations between elastic stiffness coefficients. I also investigate the effect of the assumptions made for Biot's poroelastic parameters on estimates of minimum horizontal stress in three cases. In the first case, I use the well-log-based estimates of the anisotropic poroelastic parameters. In the second and third cases, I assume $\alpha_v = \alpha_h = 0.7$ and $\alpha_v = \alpha_h = 1$, respectively.

2.3. Field Examples

I applied the proposed stress prediction workflow to field datasets and core samples from wells located in facies A and B of the lower Eagle Ford, Haynesville, and upper Wolfcamp formations. I also used lower Eagle Ford outcrop samples from facies B located at the Lozier Canyon, west of Del Río, Texas.

2.3.1 Geological description

The lower Eagle Ford formation is composed of calcite, quartz, and clay minerals illite, smectite, and kaolinite. The porosity ranges from 7-15%, and the total organic content varies from 2-7% (Smith et al., 2013). The lower Eagle Ford formation is characterized by skeletal grains, which are planktonic Globigerinid-like forams and calcispheres. This formation is calcareous with argillaceous limestone beds, and a planar laminated morphology. The Haynesville formation presents a combination of clay-rich

and carbonate-rich intervals. The porosity ranges from 8-12%, while the total organic content ranges from 1-8.5% (Hammes et al., 2011). The clay-rich intervals include pyrite, calcite-filled cracks, and shells. The intervals with lower volumetric concentration of clay are light grey, with laminations. The upper Wolfcamp formation is generally composed of quartz, calcite, dolomite, plagioclase, and pyrite, as well as the clay minerals illite, chlorite and kaolinite. This formation is medium to thinly laminated, with a porosity range of 4-8% and a total organic content of less than 9%. The upper Wolfcamp formation is composed of silty and silicified limestones and argillaceous, commonly interlaminated with organic material, and dolomitic, as well as silty and silicified mudstones that grade upwards.

2.3.2 Results and discussion

Figure 2.1 shows the comparison of the earth stress coefficient, K_0, obtained directly using uniaxial strain tests, to the K_0 estimated using **Equation 2.21**, for the Haynesville and upper Wolfcamp samples. An average relative difference of 25% is observed in estimates of K_0 in the Haynesville and upper Wolfcamp samples. The results confirm the variability in estimates of K_0 when calculated from triaxial tests. Therefore, direct measurements might be required for a more reliable evaluation of the stiffness coefficient C_{13}, and for calibration required for well-log-based geomechanical analysis. **Figure 2.2** shows the impact of the volumetric concentration of kerogen on the calculated earth stress coefficient, K_0, in the lower Eagle Ford, Haynesville, and upper Wolfcamp rock samples. I observed that the estimates of K_0 do not change significantly

(range of 0.35 to 0.6) at low volumetric concentration of kerogen (less than 0.06) in all three formations.

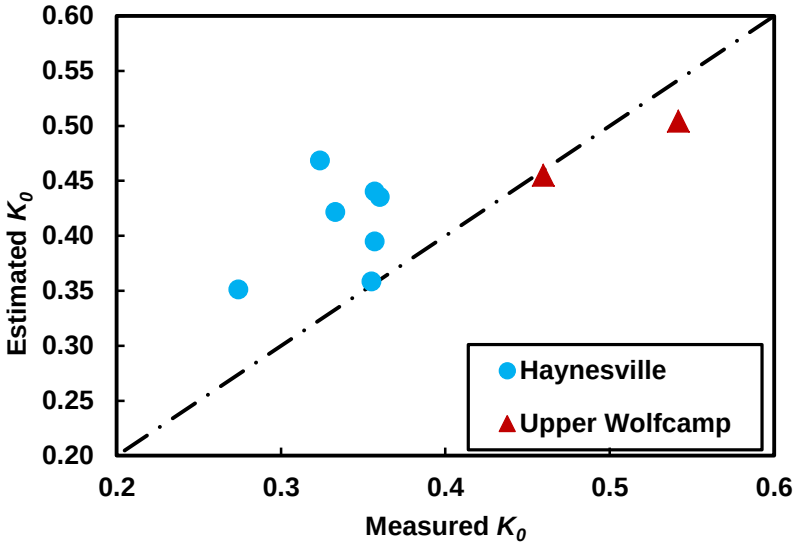

Figure 2.1: Comparison of the estimated earth stress coefficient, K_0, obtained from triaxial measurements against those obtained from uniaxial strain tests.

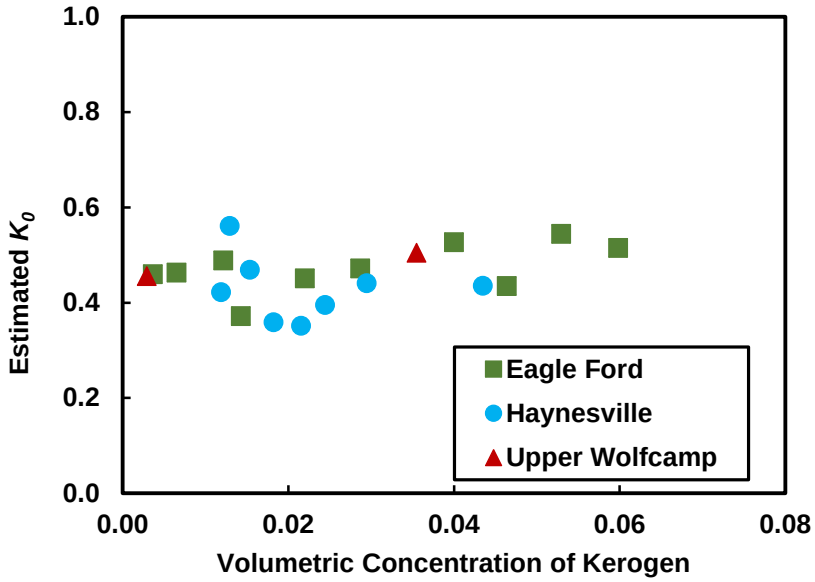

Figure 2.2: The impact of volumetric concentration of kerogen on the calculated earth stress coefficient, K_0, from triaxial tests in lower Eagle Ford, Haynesville, and upper Wolfcamp core samples.

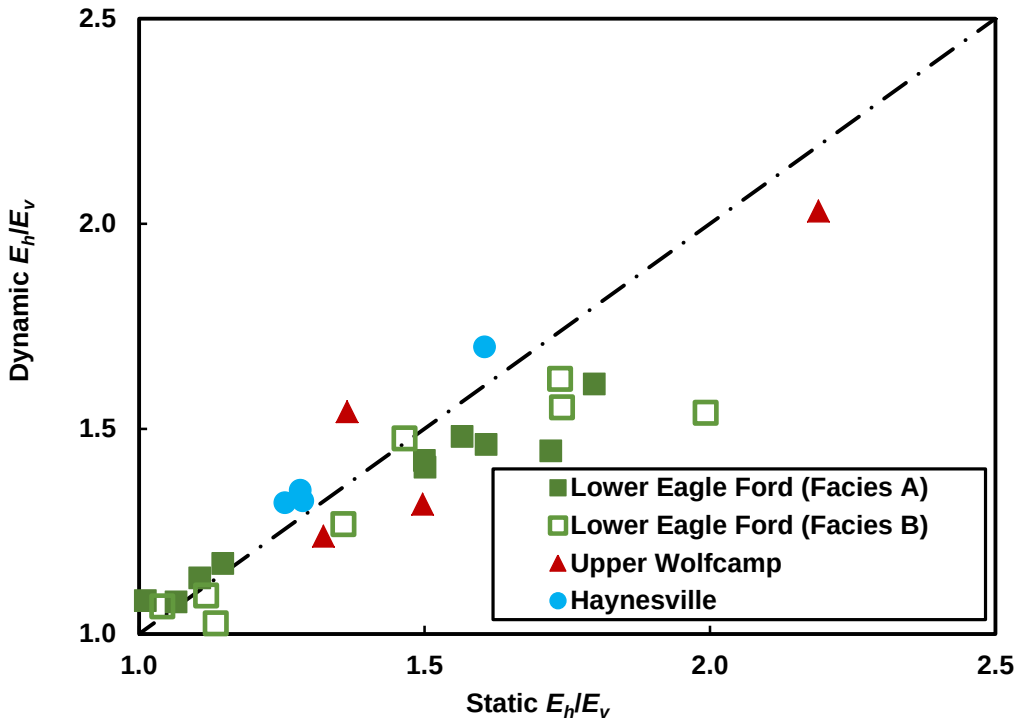

Figure 2.3: Comparison of the measured dynamic and static elastic Young's moduli in the directions parallel (horizontal) and normal (vertical) to the bedding plane in the Haynesville, upper Wolfcamp, and Facies A and B in the Eagle Ford formations.

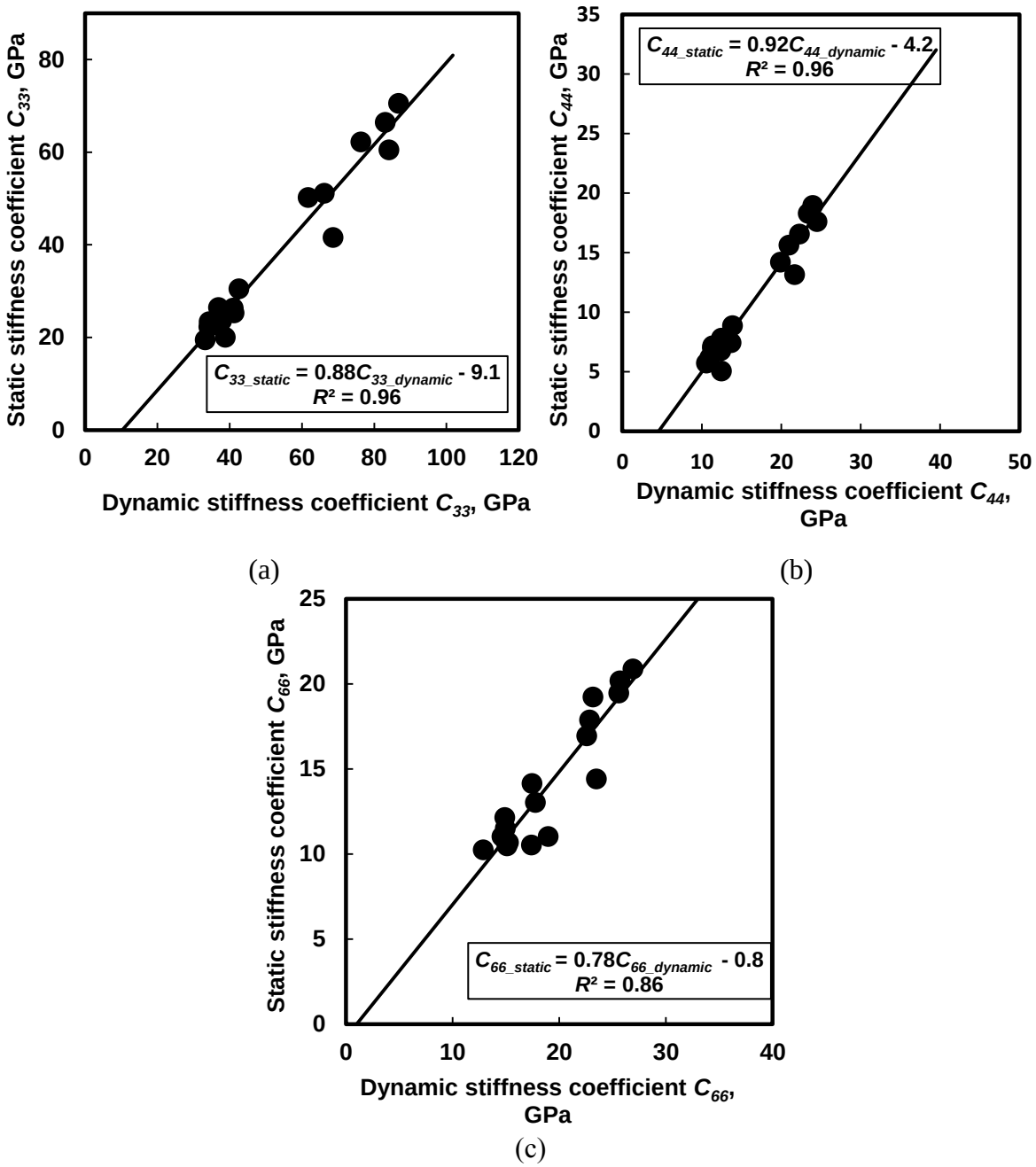

Figure 2.4: Eagle Ford Formation: Correlations between the static and dynamic stiffness coefficients (a) C_{33}, (b) C_{44}, and (c) C_{66}.

Figure 2.3 compares the ratios of the dynamic horizontal and vertical Young's moduli against the ratio of the static horizontal and vertical Young's moduli. In the cases of both facies A and B of the lower Eagle Ford shale, the ratio of horizontal to vertical Young's modulus increases above 45% in interbedded layers of calcareous mudstones. In the case of the Haynesville shale, the horizontal Young's modulus ranges from 25%-70% higher than the vertical one, in the entire depth interval. In the upper Wolfcamp shale, the horizontal Young's modulus is at least 25% higher than the vertical one.

Figure 2.4 shows the correlations between the dynamic and static stiffness coefficients in the Eagle Ford formation. I obtained similar correlations in the Haynesville and upper Wolfcamp formations. I applied the aforementioned linear relationships to estimate the well-log-based static stiffness coefficients (C_{33}, C_{44}, and C_{66}) from the well-log-based dynamic stiffness coefficients. The dynamic elastic stiffness coefficients, estimated from laboratory ultrasonic measurements, differ from dynamic elastic stiffness coefficients, obtained from in situ acoustic measurements, because of the velocity dispersion between ultrasonic and sonic frequencies. The ultrasonic velocities measured in the laboratory are not representative of the strain field over long time scales (Mossop, 2012). Therefore, uncertainties remain associated with applying laboratory-derived dynamic and static elastic stiffness coefficients in the well-log domain. **Figures 2.5a** and **2.5b** compare the compressional- and shear-wave velocities measured using ultrasonic laboratory core measurements against those obtained using acoustic well logs in the Eagle Ford formation, respectively. An average relative difference of 11% is observed in both compressional- and shear-wave velocities.

Figure 2.6 compares the horizontal Poisson's ratio to the vertical Poisson's ratio measured from triaxial stress tests. It shows that υ_v is greater than or equal υ_h in the lower Eagle Ford formation, as well as in the upper Wolfcamp formation. In the case of the Haynesville formation, υ_h is greater than υ_v.

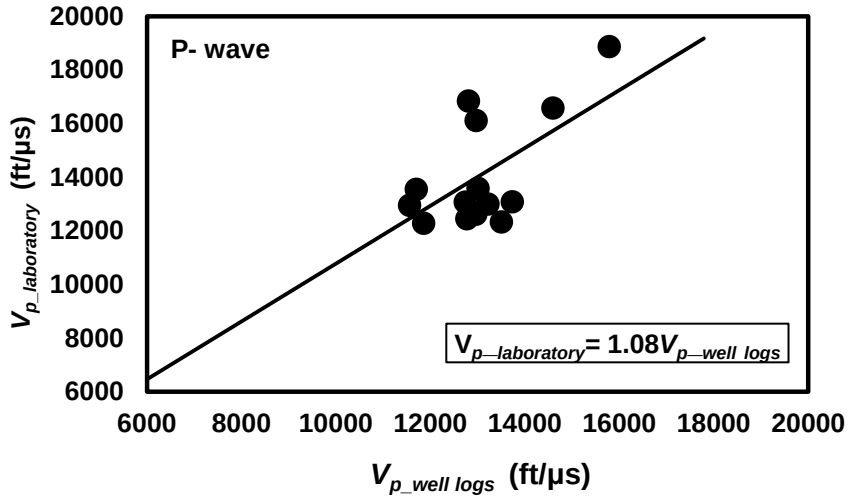

(a)

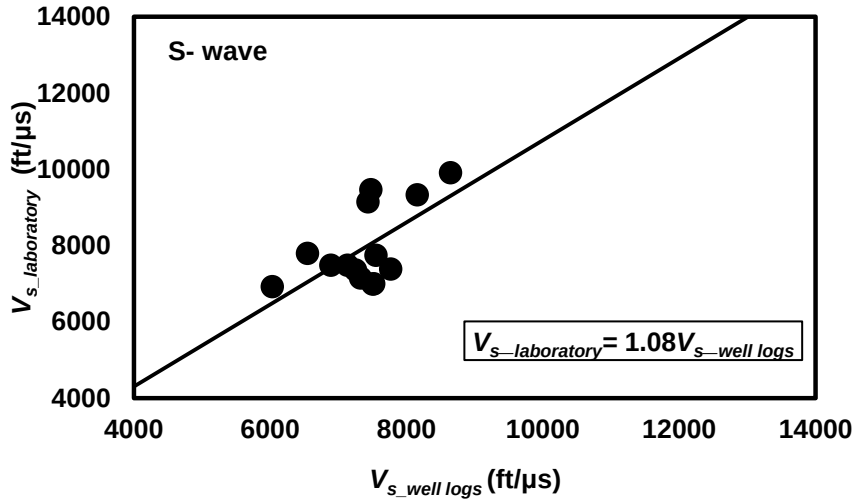

(b)

Figure 2.5: Eagle Ford Formation: Comparison between the ultrasonic velocities measured in the laboratory and the acoustic velocity logs for (a) compressional- and (b) shear-waves.

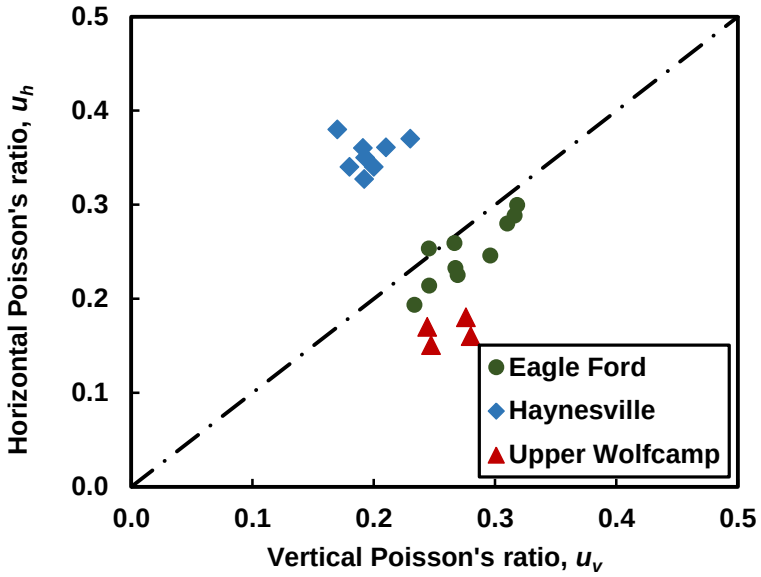

Figure 2.6: Horizontal and vertical Poisson's ratio measured using static triaxial stress tests for the core samples from Eagle Ford, Haynesville, and Upper Wolfcamp formations.

Figures 2.7a and **2.7b** compare the static stiffness coefficient C_{13} estimated using the ANNIE approximation model against those obtained from static measurements in the Eagle Ford and Haynesville formations, respectively. The C_{13} obtained from the static measurements is approximately 6% and 40% higher than the C_{13} estimated using the ANNIE approximation model for the Eagle Ford and Haynesville rock samples, respectively. **Table 2.2** shows the statistical analysis of Thomsen's parameters obtained using core measurements. The mean value of the Thomsen's parameter, δ, is the smallest compared to ε and γ in all the three formations. Thomsen's parameter δ has the highest mean value in the Haynesville formation (approximately 0.14).

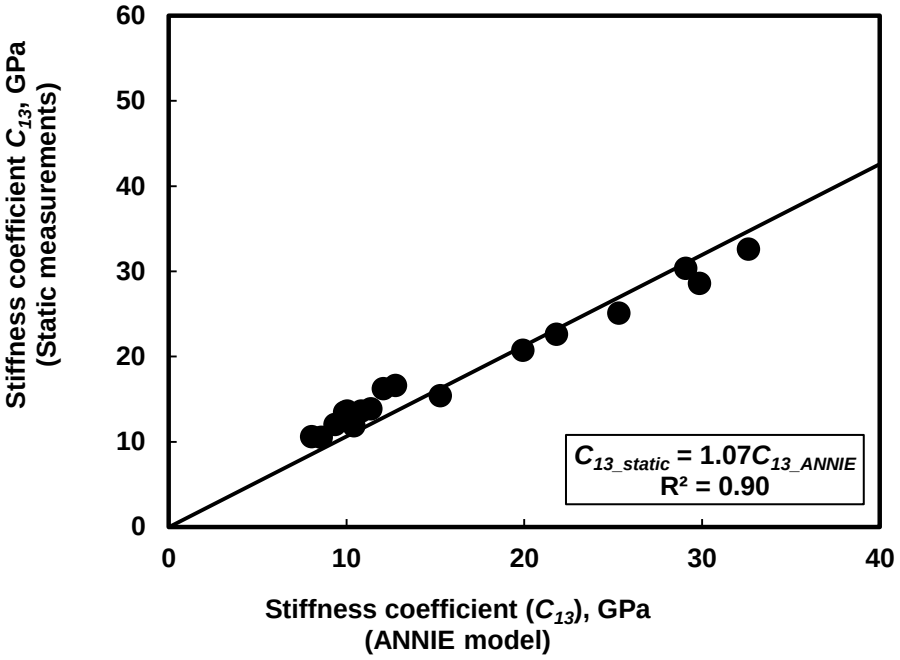

(a)

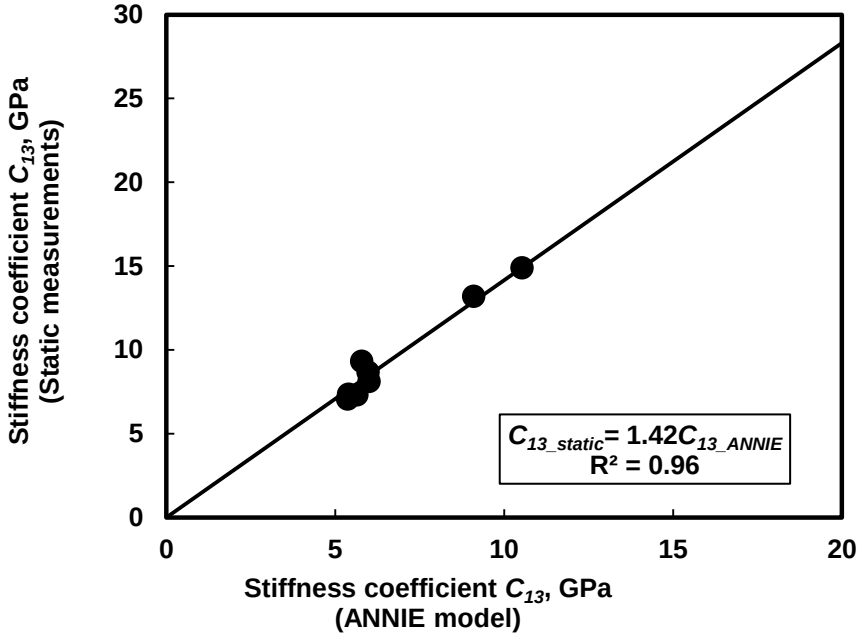

(b)

Figure 2.7: Comparisons of C_{13} values estimated using the ANNIE approximation against those obtained from static measurements in (a) Eagle Ford and (b) Haynesville formations.

Table 2.2: Statistical analysis of Thomsen's parameters obtained using core measurements**.**

Field example	Mean	Median	Minimum	Maximum	Standard Deviation
Eagle Ford					
δ	0.08	0.09	-0.02	0.20	0.07
ε	0.18	0.21	-0.02	0.39	0.14
γ	0.22	0.22	0.03	0.54	0.15
Upper Wolfcamp					
δ	0.09	0.06	0.04	0.21	0.08
ε	0.23	0.16	0.13	0.47	0.16
γ	0.36	0.28	0.20	0.69	0.22
Haynesville					
δ	0.14	0.13	0.09	0.19	0.04
ε	0.26	0.26	0.17	0.39	0.08
γ	0.12	0.11	0.06	0.19	0.06

I applied the ANNIE approximation model to estimate the remaining static stiffness coefficients (C_{11} and C_{13}) in the Eagle Ford and upper Wolfcamp formations. The use of the ANNIE approximation model is justified in this case because υ_v/υ_h is greater than one (Quirein et al., 2014). Furthermore, the mean value of Thomsen's parameter is approximately 0.08 and 0.09 in the Eagle Ford and upper Wolfcamp formations, respectively. Hence, I assumed that this value can be set to zero. Furthermore, there is no significant difference in the C_{13} obtained from the static measurements and the ones estimated using the ANNIE approximation model. I did not apply this model to the Haynesville formation because υ_v/υ_h is less than one. Furthermore, there is a significant difference in the C_{13} obtained from the static measurements and those estimated using the ANNIE approximation model. **Figure 2.8a** shows the correlation between static stiffness coefficients C_{13} and C_{33}, and **Figure 2.8b**

shows the correlation between static stiffness coefficients C_{11} and C_{66}. The correlations shown in Figures 2.8a and 2.8b are applied as an alternative to the ANNIE approximation model to estimate C_{11} and C_{13} in the Haynesville formation.

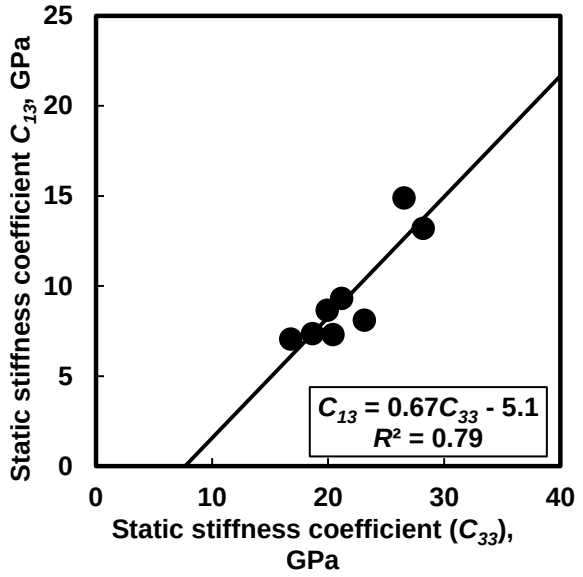

(a)

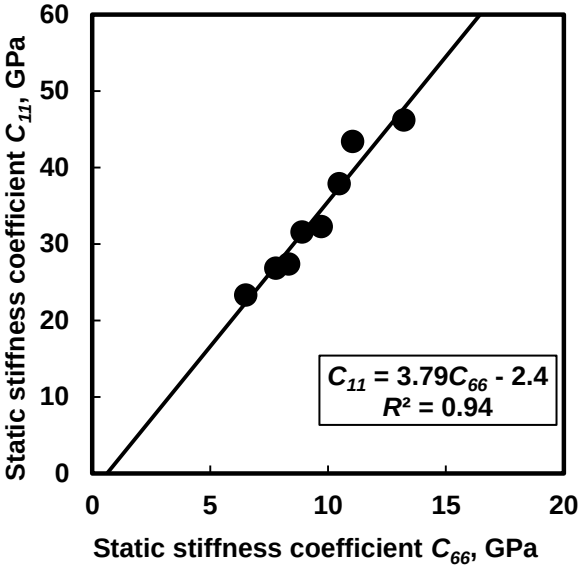

(b)

Figure 2.8: Haynesville formation: Experimentally-derived correlations betweeen the static stiffness coefficients (a) C_{13} and C_{33} and (b) C_{11} and C_{66}.

Next, I estimated the drained poroelastic coefficients of effective stresses α_h and α_v in the lower Eagle Ford, Haynesville, and upper Wolfcamp formations. Finally, I estimated the minimum horizontal stress using the elastic model for transversely isotropic media given in **Equation 2.28**. The Haynesville formation exhibits overpressure and was deposited in a passive margin (Dix et al., 2010; Hammes et al., 2011). Therefore, horizontal stresses are potentially dominated by the effects of the pore pressure rather than from tectonic effects. Constant pore pressure gradients of 20.36 MPa/km, 15.83 MPa/km and 11.7 MPa/km are assumed in the Haynesville, lower Eagle Ford and upper Wolfcamp formations, respectively.

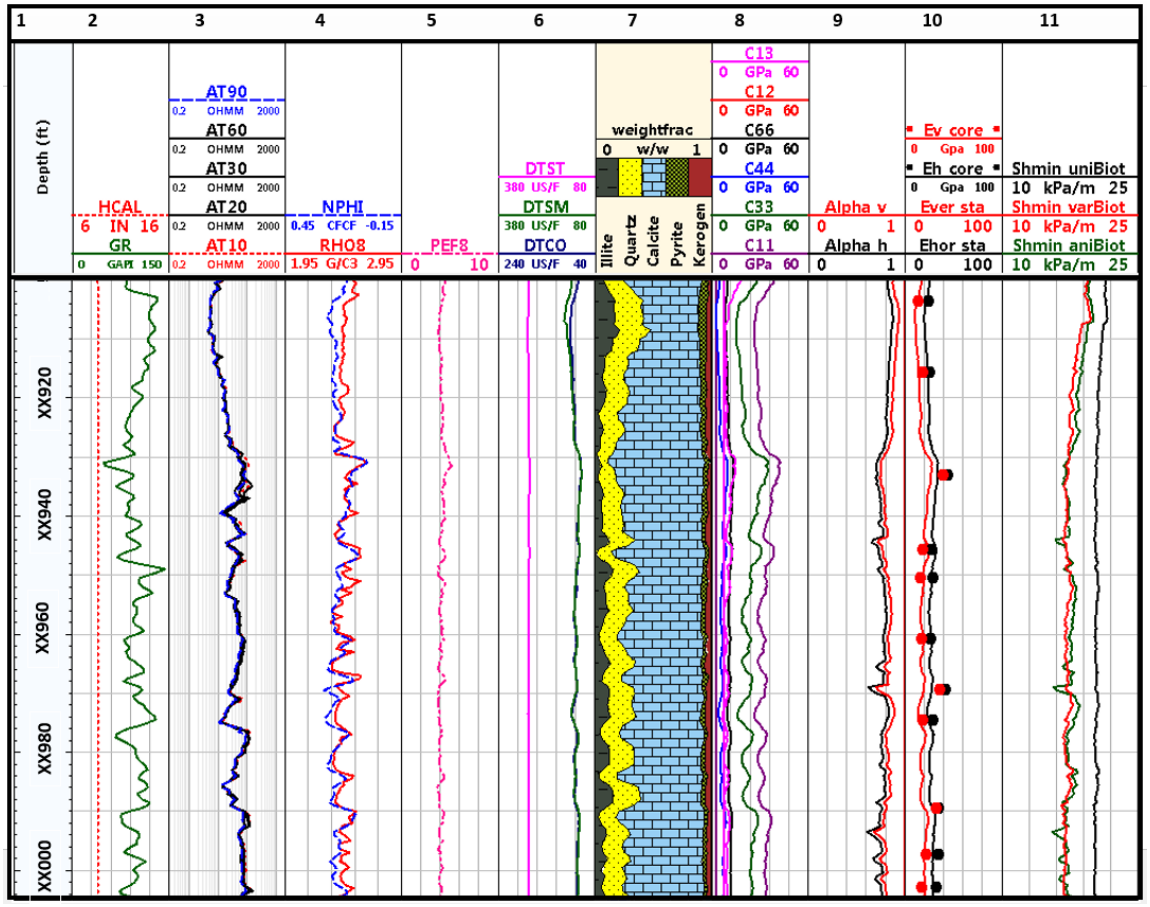

Figure 2.9: Lower Eagle Ford formation: Conventional well logs, estimates of petrophysical/ compositional, estimates of elastic and poroelastic properties, and stress profile. Tracks from left to right include, Track 1: depth; Tracks 2-6: GR/Caliper, apparent resistivity logs, neutron porosity, bulk density, PEF, and acoustic-wave slowness logs; Track 7: estimates of weight concentrations of minerals; Track 8: elastic stiffness parameters; Track 9: Young's modulus in the normal (vertical, Ever) and parallel (horizontal, Ehor) directions to the bedding plane; Tracks 10: anisotropic poroelastic parameters; and Track 11: comparisons of the estimated minimum horizontal stress gradient assuming anisotropic elastic properties and anisotropic poroelastic parameters (Shmin_aniBiot), against the cases where the anisotropic poroelastic parameters are assumed to be equal to 1 (Shmin_uniBiot), and where the anisotropic poroelastic parameters are assumed to be equal to 0.7 (Shmin_varBiot).

Figure 2.10 shows the acoustic logs, estimates of mineral volumetric concentrations, geomechanical properties, and the stress-gradient profile for a well drilled in the upper Wolfcamp formation. The significant vertical variation in volumetric concentrations of minerals (Figure 2.10, Track 7) is indicative of high vertical heterogeneity. The anisotropic poroelastic parameters vary by less than 10% (Figure 2.10, Track 10). The minimum horizontal stress-gradient estimate, assuming anisotropic elastic properties and anisotropic poroelastic parameters, is lower than that of the cases where the poroelastic parameters are assumed to be equal to 0.7 and 1 (Figure 2.10, Track 11). The average relative differences between the stress gradients, estimated after assuming anisotropic poroelastic parameters and after assuming 0.7 and 1.0 for poroelastic parameters, are approximately 20% and 50%, respectively, in the zones with relatively high volumetric concentration of clay (more than 15%). For the zones with minimal volumetric concentration of clay (less than 10%), the average relative differences between the stress gradients assuming anisotropic poroelastic parameters and the cases where these parameters are assumed to be equal to 0.7 and 1.0 are approximately 3% and 25%, respectively.

Figure 2.11 shows the acoustic logs, estimates of mineral volumetric concentrations, geomechanical properties, and the stress profile for a well drilled in the Haynesville formation. Lack of significant vertical variation in mineral concentrations (Figure 2.11, Track 7) can be indicative of relatively low vertical heterogeneity at this depth interval. The horizontal Young's modulus is more than 33% higher than the vertical one (Figure 2.11, Track 9). The estimated minimum horizontal stress gradient is

almost constant, where the poroelastic parameter is assumed to be one. The high pore pressure gradient (i.e., 20.36 MPa/km) makes the effective vertical stress term (σ_v-$\alpha_v P_p$) have a smaller weight compared to the term ($\alpha_h P_p$) in Equation 2.28. Hence, if the anisotropic poroelastic parameters are assumed to be equal to one (i.e., $\alpha_h = \alpha_v = 1$), the minimum horizontal stress gradient will be dominantly affected by the term $\alpha_h P_p$, which results in an almost constant minimum horizontal stress gradient because both parameters α_h and P_p are constants. The minimum horizontal stress gradient estimates, assuming anisotropic elastic properties and anisotropic poroelastic parameters, is lower than the cases where the poroelastic parameters are assumed to be equal to 0.7 and 1 (Figure 2.11, Track 11). The average relative differences are approximately 12% and 34% where the poroelastic parameters are assumed to be equal to 0.7 and 1, respectively, compared to the case with anisotropic poroelastic parameters. Track 12 (Figure 2.11) shows the minimum horizontal stress gradient estimated using anisotropic elastic properties obtained from experimentally-derived correlations between the static stiffness coefficients (green solid curve). The green dotted curve represents the minimum horizontal stress gradient estimated using the ANNIE approximation model (Figure 2.11, Track 12). An average relative difference of 14% is observed between the minimum horiziontal stress gradients estimated using the aformentioned two approaches (green solid and green dotted curves).

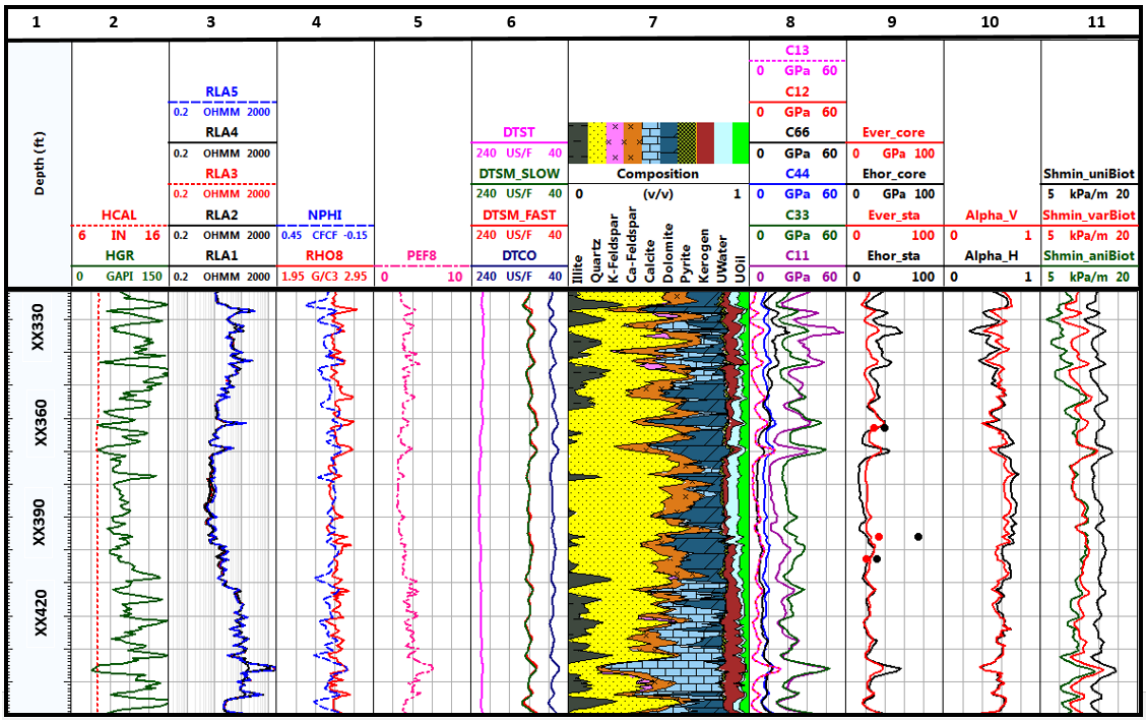

Figure 2.10: Upper Wolfcamp formation: Conventional well logs, estimates of petrophysical/ compositional, estimates of elastic and poroelastic properties, and stress profile. Tracks from left to right include, Track 1: depth; Tracks 2-6: GR/Caliper, apparent resistivity logs, neutron porosity, bulk density, PEF, and acoustic-wave slowness logs; Track 7: estimates of volumetric concentrations of minerals; Track 8: elastic stiffness parameters; Track 9: Young's modulus in the normal (vertical, Ever) and parallel (horizontal, Ehor) directions to the bedding plane; Tracks 10: anisotropic poroelastic parameters; and Track 11: comparisons of the estimated minimum horizontal stress gradient assuming anisotropic elastic properties and anisotropic poroelastic parameters (Shmin_aniBiot), against the cases where the anisotropic poroelastic parameters are assumed to be equal to 1 (Shmin_uniBiot), and where the anisotropic poroelastic parameters are assumed to be equal to 0.7 (Shmin_varBiot).

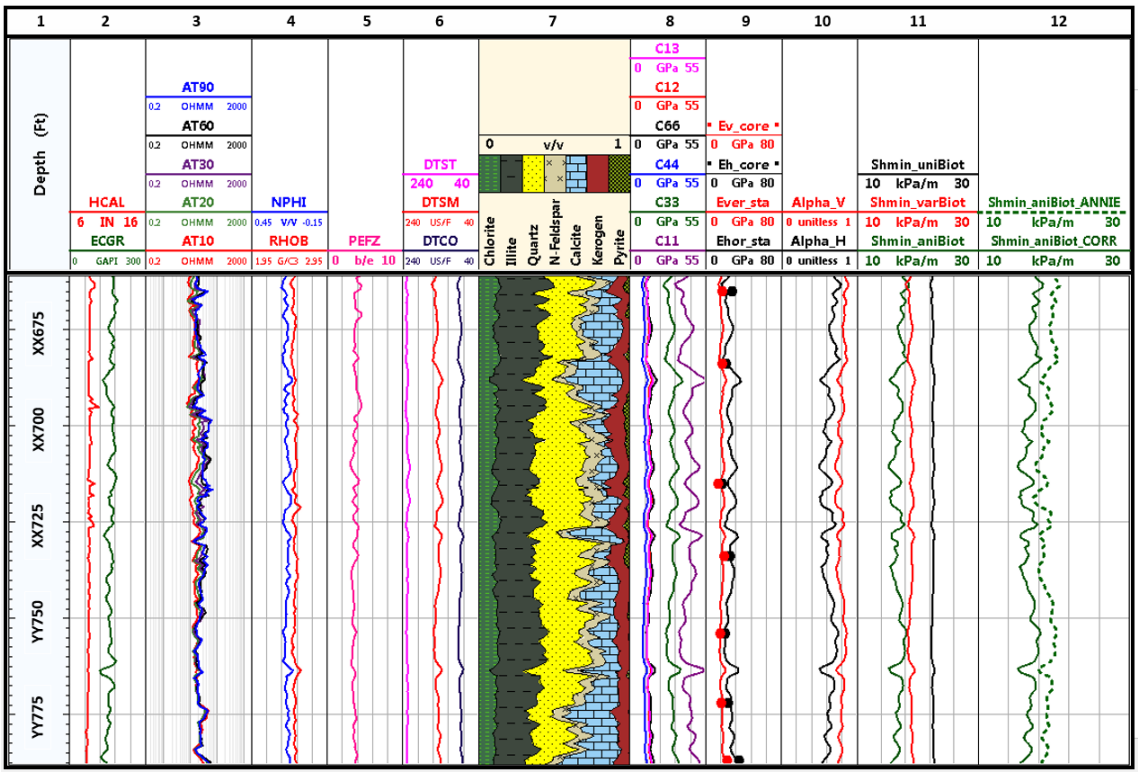

Figure 2.11: Haynesville formation: Conventional well logs, estimates of petrophysical/ compositional, estimates of elastic and poroelastic properties, and stress profile. Tracks from left to right include, Track 1: depth; Tracks 2-6: GR/Caliper, apparent resistivity logs, neutron porosity, bulk density, PEF, and acoustic-wave slowness logs; Track 7: estimates of volumetric concentrations of minerals; Track 8: elastic stiffness parameters; Track 9: Young's modulus in the normal (vertical, E_{ver}) and parallel (horizontal, E_{hor}) directions to the bedding plane; Tracks 10: anisotropic poroelastic parameters; Track 11: comparisons of the estimated minimum horizontal stress gradient assuming anisotropic elastic properties (estimated from experimentally-derived correlations between the static stiffness coefficients) and anisotropic poroelastic parameters (Shmin_aniBiot), against the cases where the anisotropic poroelastic parameters are assumed to be equal to 1 (Shmin_uniBiot), and where the anisotropic poroelastic parameters are assumed to be equal to 0.7 (Shmin_varBiot); and Track 12: comparisons of the estimated minimum horizontal stress gradient assuming anisotropic poroelastic parameters and anisotropic elastic properties estimated from experimentally-derived correlations between the static stiffness coefficients (Shmin_aniBiot_CORR), against estimated minimum horizontal stress gradient assuming ANNIE approximation model (Shmin_aniBiot_ANNIE).

2.4 Conclusions

In this section, I evaluated the impact of anisotropic poroelastic parameters and mechanical anisotropy on minimum horizontal stress prediction in organic-rich mudrocks. I carried out experiments on core samples to measure static and dynamic anisotropic elastic properties, as well as elastic stiffness coefficients. Then I used well-log-based estimates of petrophysical properties, and applied anisotropic elastic and poroelastic properties to predict depth-by-depth minimum horizontal stress. I applied the described methods to field examples from the Eagle Ford, Haynesville, and upper Wolfcamp formations with different degrees of anisotropy and vertical heterogeneity. I observed a minimal difference (less than 6%) between estimated anisotropic poroelastic parameters, in the vertical and horizontal directions, in depth intervals with low degrees of mechanical anisotropy and low vertical heterogeneity, such as in the case of the lower Eagle Ford formation. In the upper Wolfcamp example, which exhibits high anisotropy and high vertical heterogeneity, differences in the anisotropic poroelastic parameters, as well as Young's moduli in the vertical and horizontal directions, were proportional to changes in the volumetric concentration of minerals. The Haynesville formation exhibited a high mechanical anisotropy, but low vertical heterogeneity.

Results from the three field examples confirmed that the assumption of Biot's poroelastic parameter equal to one resulted in higher estimates of minimum horizontal stress gradient (approximately 30%) compared to the case where well-log-based estimates of anisotropic poroelastic parameters were used instead. A difference of less than 6% was observed between the estimates of minimum horizontal stress gradients

using Biot's poroelastic parameters equal to 0.7 and anisotropic poroelastic parameters. This characteristic was observed in formations with relatively low vertical heterogeneity and degree of mechanical anisotropy, as well as in intervals with low volumetric concentration of clay. This difference was more significant (approximately 15%) in formations with high vertical heterogeneity and mechanical anisotropy, and in intervals with high volumetric concentration of clay. In the case of the Haynesville formation, I showed that the use of the ANNIE approximation model could not be justified because (a) the mean Thomsen's parameter, δ, in the Haynesville formation had the highest value among the three formations, (b) C_{13} static measurements were approximately 40% higher than the ANNIE C_{13} estimates, and (c) ratios of υ_v/υ_h were less than one. The minimum horizontal stress was therefore estimated using experimentally-derived correlations to obtain C_{13} and C_{11}. The estimated minimum horizontal stress using experimentally-derived correlations was approximately 14% higher compared to the case where the minimum horizontal stress was estimated using the ANNIE approximation model.

Core measurements also showed that estimates of K_0 differ from direct measurements by up to 20%, when the difference between horizontal and vertical Young's moduli increases. The results confirm that anisotropy and vertical heterogeneity influences stress prediction. The outcomes of this dissertation can help improve stress predictions for geomechanical characterization in formations with different degrees of anisotropy and vertical heterogeneity.

CHAPTER III

APPLICATION OF NANOINDENTATION FOR VARIABILITY ASSESSMENT OF ELASTIC PROPERTIES IN MUDROCKS AT THE MICRO-SCALE AND WELL-LOG DOMAINS [*]

Variability in estimates of elastic properties of soft mudrock components such as clay minerals and kerogen can influence well-log-based evaluation of effective elastic properties in organic-rich mudrocks. Existing methods, such as effective medium models for well-log-based assessment of elastic properties, assume constant stiffness and idealized shape for rock components. However, these characteristics might vary depending on the distribution and size of that particular component, as well as its adjacent components. Furthermore, there is a significant variability in elastic properties of kerogen in the case of organic-rich mudrocks. The variability associated with the aforementioned parameters on effective elastic properties of rocks has not been investigated in previous publications. In this chapter, I quantify the variability in elastic properties of individual mudrock components caused by their spatial distribution, size, and rock fabric, at the micro-scale domain, and their impact in well-log-based evaluation of effective elastic properties.

In this chapter, I performed nanoindentation tests on samples from the Haynesville and the lower Eagle Ford formations, to measure Young's modulus and hardness at targeted locations. Then, I quantified the variability of Young's modulus in

[*] Reprinted with permission from "Application of Nanoindentation for Uncertainty Assessment of Elastic Properties in Mudrocks from Micro- to Well-Log-Scale" by Clotilde Chen Valdes and Zoya Heidari, 2017. Geophysics, Ahead of Print, Copyright 2017 by the Society of Exploration Geophysicists.

the micro-scale domain and its impact on effective elastic properties at the micro-scale and well-log domains. Results revealed significant uncertainties in measurements of elastic properties of soft rock components, associated with their location and size. Young's moduli of individual clay components were higher when located adjacent to stiff rock components, such as large quartz and calcite grains. They were, however, smaller when the targeted clay minerals had a large surface area, or when located adjacent to other clay minerals. The results revealed that 25% and 12% uncertainties in measured elastic properties of clay minerals affected well-log-based estimates of effective elastic stiffness coefficients up to 29% and 11 % in the Haynesville and the lower Eagle Ford formations, respectively. These uncertainties can be more significant in cases with higher concentration of clay minerals and kerogen.

3.1 Introduction

Reliable characterization of mechanical behavior is challenging in organic-rich formations (Mokhtari et al., 2013), yet required for geomechanical modelling (Ostadhassan et al., 2012), successful fracture treatment (Serajian and Ghassemi, 2011), and post-fracturing analysis. Mechanical behavior in mudrocks is often evaluated through existing methods for well-log-based assessment of elastic properties, which assimilate rock mass stiffness. Well-log-based assessment of mechanical properties is commonly carried out using a combination of conventional and advanced acoustic well logs, empirical rock-physics relations, and mechanical homogenization formulations. However, rock-physics formulations commonly use ideal assumptions such as linear elasticity of the rock mass. Furthermore, mechanical homogenization formulations only

account for the volumetric concentrations of the rock components, and assume that the rock components are regular-shaped, and within the elastic deformation regime. Consequently, laboratory measurements are used to correct for the limitations introduced by wireline resolution and by micromechanical models in well-log-based estimates of rock mechanical properties.

Core-scale measurements of rock mechanical properties provide an accurate description of mechanical behavior in the formation. However, availability of core samples is very limited, and experimental procedures are often time consuming and costly, therefore, core samples are selected and spaced at depths of interests, which might not be representative for a mechanical model. Furthermore, in organic-rich formations, successful core recovery is a common issue due to uncoupling of interbedded phases and laminations created by clay minerals, and natural and mechanical fractures. Moreover, measurements of mechanical properties from core samples are often defined under the assumption of either elastic or plastic behavior in an infinite medium; however, the presence of end-cap effects can introduce uncertainties in the aforementioned estimates.

Micro-scale measurements of rock mechanical properties can be performed via instrumented sharp indentation. This technique provides a fingerprint in the evaluation of elastic and plastic properties, as it uses small volumes of rock masses obtained from drilling cuttings. Furthermore, a major availability of samples leads to a higher volume of nanoindentation tests, which results in a broader characterization of rock mechanical properties in the micro-scale level of investigation.

Previous publications have evaluated micro-scale domain mechanical properties of mudrocks using nanoindentation experiments. Kumar et al. (2012) found that Young's moduli measurements on millimeter size samples were in agreement with dynamic Young's moduli in core samples. Shukla et al. (2013) also measured Young's modulus and hardness using drilling cuttings from shale samples in the micro-scale domain. They found correlations between compositional properties, porosity, total organic content and mechanical properties in shales. Shukla et al. (2013), De Block et al. (2015) and Mason et al. (2014) also observed that the total organic content (TOC) is the major contributor in Young's moduli reduction in shale samples.

Elastic properties of clay minerals are poorly understood, and data on elastic properties of clay minerals is scarce (Vyzhva et al., 2014; Katahara, 1996). Young's modulus of clay minerals is often assumed as a fixed value of 27.5 GPa (Hornby, 1994). Clay type, bound water in the interlayers, and anisotropy due to layering are common sources of variability in elastic moduli of clay minerals (Pal Bathija et al., 2008). However, the variability in elastic moduli of clay minerals is often overlooked in estimates of effective elastic properties of mudrocks. Pal Bathija et al. (2008) measured Young's modulus of clay minerals via nanoindentation. Moreover, they employed molecular simulation to estimate Young's modulus and hardness of montmorillonite, muscovite mica, and kaolinite clay minerals. This study, however, measured elastic properties of clay minerals in powder clay samples, and not as a mineral component within the rock matrix.

Multi-scale mechanical properties in mudrocks have not been extensively studied and documented, mainly due to their high heterogeneity and anisotropy (Ren and Spikes, 2014). Ortega et al. (2010) introduced a multi-scale micromechanics model, in which they use mineralogical and petrophysical data to define elastic anisotropy in shales. This model enables estimating mechanical response of shale rocks using nanoindentation and core-scale experiments.

The aforementioned publications did not quantify the variability of elastic properties in mudrocks as a function of factors such as mineral and kerogen distribution within the rock, and grain size in the rock matrix. The objectives of this chapter include: (a) quantify the variability of elastic properties of rock components (e.g., clay and kerogen) which can vary at different locations in the rock depending on the adjacent minerals, and (b) quantify the variability in well-log-based estimates of effective elastic properties of the rock, caused by variation in elastic properties of individual rock components at micron-scale. Nanoindentation mechanical tests are used to quantify the variability in elastic properties of mudrock components in the micro-scale level of investigation. The elastic properties of individual mudrock components measured via nanoindentation mechanical tests are then used as inputs for well-log-based assessment of effective elastic properties. Furthermore, I quantify the variability in the well-log-based estimates of effective elastic properties estimated using the inputs from nanoindentation results and the associated uncertainties of elastic properties in the micro-scale domain. The following sections describe the methods introduced in this

dissertation and their applications to field examples in the lower Eagle Ford and the Haynesville formations.

3.2 Method

I use a multi-scale experimental approach for the assessment of uncertainties in elastic properties of mudrock components. Furthermore, I evaluate the impact of these uncertainties on effective elastic properties of organic-rich mudrocks at the micro-scale, core-scale, and well-log-scale domains. I perform nanoindentation mechanical tests to estimate elastic properties of mudrock components (e.g., kerogen, clay and non-clay minerals), in the micro-scale domain. Then I quantify the variability of elastic properties in each mudrock component due to factors such as location in the rock sample, adjacent minerals, and particle size. Then I use the measurements of elastic properties in individual mudrock components and their uncertainties, as inputs to estimate effective elastic properties at the well-log domain. I then compare well-log-based estimates of effective elastic properties estimated using the inputs from nanoindentation results against those obtained from core-scale measurements.

In the micro-scale domain, I use a micromechanical framework to estimate the effective mechanical properties in organic-rich mudrock formations. The selected scale of investigation encompasses levels I and II of homogenization (Gathier, 2008). At level I, the representative elementary volume (REV) of rock is composed of clay composite, and the presence of clay minerals is evident. Furthermore, rock components are distinguishable at this level using imaging techniques, such as scanning electron microscopy (SEM), and the mineral chemical composition can be verified through

energy dispersive spectroscopy chemical microanalysis (EDS). At level II (i.e., 10^{-5} to 10^{-4} m), representative elementary volume of rock is composed of clay combined with non-clay minerals (e.g., quartz and calcite), and pore space. Furthermore, the difference in stiffness between the clay phase and non-clay components is detectable at this scale, which helps to investigate coupling and interaction of individual mudrock components.

3.2.1 Experimental procedure at the micro-scale domain

I carry out nanoindentation mechanical tests at room temperature in mudrock samples obtained from cuttings. The rock samples are prepared to achieve indentation surfaces parallel to the bedding plane, with approximate dimensions of 3 mm x 3 mm x 1 mm. Then I mechanically polish the sides, top and bottom surfaces of the samples, to ensure flatness and perpendicularity of the sample surfaces. Then I select an area of interest for nanoindentation, and polish the target surface area using argon ion milling.

After ion milling, I select two types of indentation targets in the rock samples: (a) individual mineral mudrock components and kerogen (**Figure 3.1**) and (b) mixtures of mudrock mineral components and kerogen (**Figure 3.2**). To target individual rock components (e.g., minerals and kerogen), they must have surface dimensions of larger than 5μm x 5μm. This ensures that the axial load is exclusively applied to the component of interest, and the instrument is not applying load over a mixture of rock components. EDS and SEM techniques are then combined to identify the individual mudrock components to target. Then I create micro-machined trenches as shown in the example in **Figure 3.1a**, to be able to locate the minerals under the optical microscope. **Figure 3.1b** shows the same view captured by an optical microscope attached to the nanoindentation

device. Although the target clay minerals are not visible in Figure 3.1b, I was able to locate them using the micro-machined trenches as references.

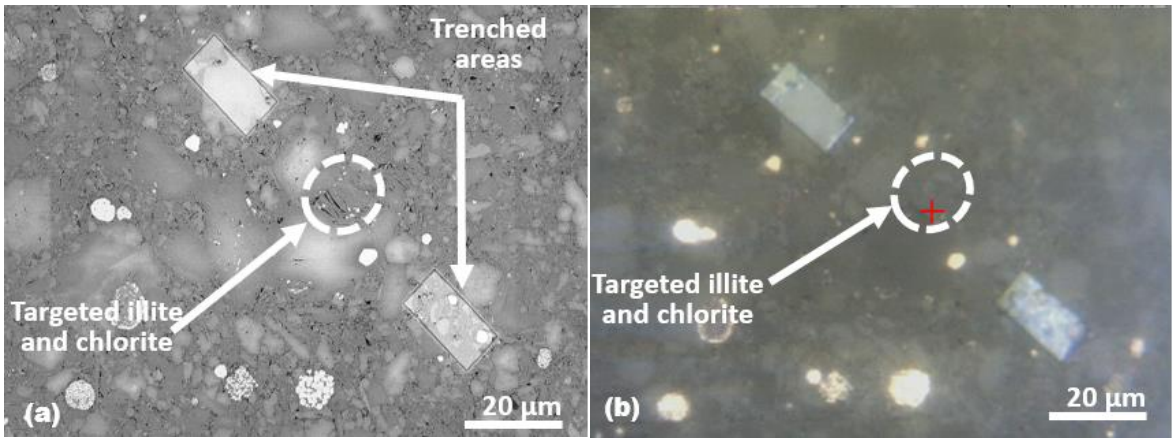

(a) (b)

Figure 3.1: Haynesville Formation: Trenches created in the rock samples by micromachining, visualized by (a) SEM and (b) optical microscope using a 40X optic lens.

In the case of indentation in mixtures of mineral components and kerogen, I perform indentation tests in a regular spacing pattern over the argon milled surface of the rock samples. The indentation spacing is determined by ensuring that the individual areas of influence under the indentations do not interact within each other. I use Westergaard (1939) formula for point loads to determine the area of influence and minimum spacing under the indentations. This formula was originally developed for non-isotropic soils that exhibit a combination of clay and thin layers of coarser and stiffer material, by using pressure isobars to estimate vertical stress distribution (σ_z), under an applied surface load P, using **Equation 3.1**

$$\sigma_z = \frac{P}{z^2} I_w, \tag{3.1}$$

where z is the vertical depth from the surface and I_w is the Westergaard stress coefficient, given by **Equation 3.2**

$$I_w = \frac{(1/\pi)}{\left[1+2(r/z)^2\right]^{3/2}}. \tag{3.2}$$

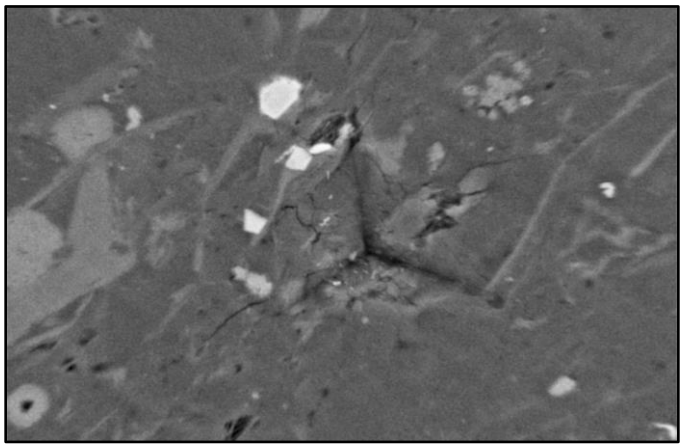

Figure 3.2: Indentation carried out over a mixture of rock components in the lower Eagle Ford formation.

For indentation in mixtures of mineral components, I select a REV to target the effective elastic properties of the rock. The REV selected is larger than the indentation imprint (15 μm x 15 μm), and it encompasses at least the longest dimension of the largest

grain in the area of interest. The selected REV must also comprise an equivalent mineral composition to that of the rock in larger scale.

3.2.2 Evaluation of elastic properties in the micro-scale domain

I apply an axial load, P, over the rock sample surface at a constant rate, using a Berkovich indenter (Berkovich, 1950) during the nanoindentation tests. The outcome of the nanoindentation test is a curve representing displacements as the result of an applied load (Figure 3.3). This load-displacement data provides information about material elastic properties such as Young's modulus, and plastic properties such as compressive yield strength, strain hardening coefficient, and hardness. Constitutive relations for elasto-plastic materials are not well understood. Therefore, I derive mechanical properties of the rock samples via a mechanical work-energy approach, in combination with the existing elasto-plastic formulations from finite element analysis (Giannakopoulos et al, 1999).

In both types of indentation targets, I measure elastic and plastic properties in each sample using a mechanical work-energy approach. The elastic deformation region in represents recoverable work (W_e), the plastic deformation region represents the permanent work (W_p), and the total work (W_t) is equal to summation of the recoverable and permanent work. The permanent and total work, W_p and W_t, are represented by the areas below the unloading and loading curve, respectively. Based on mechanical work-energy approach, I then estimate elastic modulus, E, as described by Giannakopoulos (1999) and shown as follows

$$E = d^* \frac{H}{1 - \frac{W_p}{W_t}}, \tag{3.3}$$

where d^* is equal to 4.678 for Berkovich indenters (Constantinides et al., 2003) and H is the material hardness, defined as the average applied load in a contact area, A_c. H can be calculated via **Equation 3.4**

$$H = \frac{P}{A_c}. \tag{3.4}$$

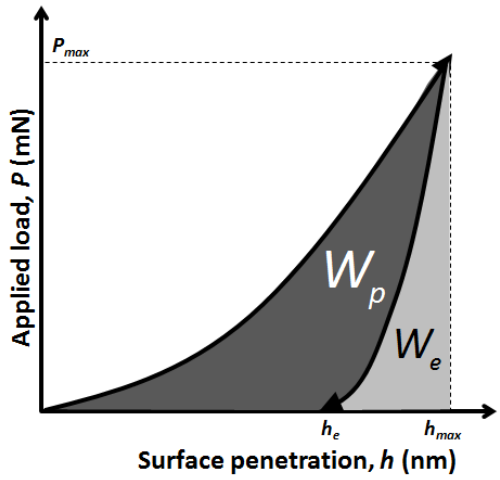

Figure 3.3: Mechanical work-energy approach to calculate Young's modulus and hardness.

In the case of indenting individual mudrock components, I evaluate their elastic properties with respect to their position within the rock sample. Then, I quantify the variability of Young's modulus and hardness of mudrock components (kerogen, clay and non-clay minerals) at different locations on the surface of rock samples. In the case of targeting mixtures of mudrock components, I use EDS to quantify the volumetric

concentrations of minerals covered by each indentation. I then apply self-consistent approximation model (SCA) (Berryman, 1995), which assumes that to quantify the difference between effective elastic properties and measured elastic properties using nanoindentation experiments. Estimates of SCA approximation model to obtain effective bulk and shear moduli are given by **Equation 3.5** and **Equation 3.6**:

$$\sum_{i=1}^{N} x_i \left(K_i - K_{sc}^{*} \right) P^{*i} = 0 \tag{3.5}$$

and

$$\sum_{i=1}^{N} x_i \left(\mu_i - \mu_{sc}^{*} \right) Q^{*i} = 0, \tag{3.6}$$

where N is the number of rock component, x_i is volumetric concentration of the ith rock component, K_i is the bulk modulus of the rock component i. Shape factors P^*_i and Q^*_i are function of the shape and aspect ratios of each rock component. The shape factors are expressed as

$$P_i^* = \frac{1}{3} T^{(i)}_{jjll} \tag{3.7}$$

and

$$Q_i^* = \frac{1}{5} T^{(i)}{}_{jljl} - P_i, \tag{3.8}$$

where $T^*{}_i$ refers to Wu's tensor (Wu, 1966), which homogenizes the far-field strain to the strain within the individual rock components.

Measured elastic properties of individual mudrock components are then used as inputs to the SCA approximation model, and the aspect ratios are selected based on observations at homogenization levels I and II, via SEM images. I finally estimate Young's modulus by

$$E_{sca} = \frac{9 K_{sc}{}^* \mu_{sc}{}^*}{3 K_{sc}{}^* + \mu_{sc}{}^*}. \tag{3.9}$$

The SCA model is valid under the assumption that the material is linear elastic and isotropic. I have the same assumption for nanoindentation tests where the load is assumed to be applied over an infinite surface of an isotropic material. I perform nanoindentation experiments over the surface of the rock sample in a square-shaped pattern. I then use a secondary electron (SE) imaging technique to identify the indented surfaces. SE imaging provides information about morphology and topography of rock surfaces, which demonstrate deformations on the sample surface. The next step includes surface mapping via EDS analysis to identify the position and volumetric concentrations of minerals within each indentation. Finally, the relative difference between the measured and estimated Young's modulus of the mudrock mixture is quantified by

$$e_E = \left| \frac{E_{measured} - E_{sca}}{E_{sca}} \right| \times 100, \tag{3.10}$$

where $E_{measured}$ is the Young's modulus measured from nanoindentation experiments and E_{sca} is the Young's modulus calculated from self-consistent approximation model.

3.2.3 Multi-scale evaluation of elastic properties

I apply measurements of elastic properties of individual mudrock components from nanoindentation tests as inputs to well-log-based assessment of effective elastic properties. I then quantify the variability in the well-log-based estimates of effective elastic properties estimated using the inputs from nanoindentation results by comparing the aforementioned estimates to well-log-based estimates of static elastic properties obtained from core measurements.

The first step in the well-log-based assessment of elastic properties includes conducting well-log interpretation for the assessment of total porosity, water saturation, and volumetric concentrations of minerals and kerogen. Input well logs for petrophysical and compositional evaluation include gamma ray (GR), electrical resistivity, density, neutron porosity, photoelectric factor (PEF), elemental capture spectroscopy (ECS), and compressional-wave slowness. The estimates of mineral concentrations are cross validated using X-Ray Diffraction (XRD) and total organic content (TOC) core measurements.

Estimates of mineral concentrations and elastic properties of individual mineral components, measured via nanoindentation tests, are then used as inputs to calculate depth-by-depth effective elastic properties in the well-log domain. The estimated effective elastic properties at the well-log domain are then rewritten in the form of the

effective elastic stiffness tensor in a transversely isotropic formation in the vertical axis of symmetry.

Different effective media models can be considered for the assessment of the effective stiffness tensor, depending on the mechanical characteristics, lithology, and geological traits of the formation under study. I use two different effective media models for assessment of effective stiffness tensor in the two field examples documented in this chapter, the Haynesville and lower Eagle Ford formations.

3.2.3.1 Assessment of effective stiffness tensor in the Haynesville formation

In the case of the Haynesville formation, I use Eshelby-Cheng (1978, 1993) model, which is used to estimate the effective anisotropic stiffness tensor for transversely isotropic, cracked rocks. The Eshelby-Cheng model assumes an isotropic, homogeneous, and elastic background, and idealized ellipsoidal cracks. In the Haynesville formation, the medium and high stiffness rock components (e.g. quartz, calcite, pyrite) represent the isotropic, homogeneous and elastic background. The soft components (e.g. clay minerals and kerogen) are represented as the idealized ellipsoidal inclusions. The general form of the Eshelby-Cheng elastic effective stiffness tensor is given by

$$C_{ij}^{\ eff} = C_{ij}^{\ 0} - \phi C_{ij}^{\ 1} \tag{3.11}$$

where ϕ and $C_{ij}^{\ 0}$ represent the porosity and the stiffness tensor for the homogeneous elastic background, respectively. $C_{ij}^{\ 1}$ represents the corrections in the elastic stiffness tensor due to the ellipsoidal inclusions, and can be written as

$$C_{11}{}^{1} = \lambda\left(S_{31} - S_{33} + 1\right) + \frac{2\mu E}{D(S_{12} - S_{11} + 1)}, \tag{3.12}$$

$$C_{13}{}^{1} = \frac{\left(\lambda + 2\mu\right)\left(S_{13} + S_{31}\right) - 4\mu C + \lambda\left(S_{13} - S_{12} - S_{11} - S_{33} + 2\right)}{2D}, \tag{3.13}$$

$$C_{33}{}^{1} = \frac{\left(\lambda + 2\mu\right)\left(-S_{12} - S_{11} + 1\right) + 2\lambda S_{13} + 4\mu C}{2D}, \tag{3.14}$$

$$C_{44}{}^{1} = \frac{\mu}{1 - 2S_{1313}}, \tag{3.15}$$

and

$$C_{66}{}^{1} = \frac{\mu}{1 - 2S_{1212}}, \tag{3.16}$$

where

$$C = \frac{K_{c,k}}{3(K - K_{c,k})}, \tag{3.17}$$

$$D = S_{33}S_{11} + S_{33}S_{12} - 2S_{31}S_{13} - (S_{11} + S_{12} + S_{33} - 1 - 3C) - C\left[S_{11} + S_{12} + 2\left(S_{33} - S_{13} - S_{31}\right)\right] \tag{3.18}$$

$$E = S_{33}S_{11} - S_{31}S_{13} - (S_{33} + S_{11} - 2C - 1) + C\left(S_{31} + S_{13} - S_{11} - S_{33}\right) \tag{3.19}$$

$$S_{11} = QI_{aa} - RI_{a} \tag{3.20}$$

$$S_{12} = QI_{ab} - RI_{a} \tag{3.21}$$

$$S_{31} = QI_{ac} - RI_{a} \tag{3.22}$$

$$S_{1212} = QI_{ab} + RI_{a} \tag{3.23}$$

$$S_{11} = QI_{aa} - RI_{a} \tag{3.24}$$

$$S_{33} = Q\left(\frac{4\pi}{3} - 2I_{ac}\alpha^{2}\right) + I_{c}R, \tag{3.25}$$

$$S_{13} = QI_{ac}\alpha^2 - RI_a, \tag{3.26}$$

$$S_{1313} = \frac{Q\left(1+\alpha^2\right)I_{ac}}{2} + \frac{R\left(I_a + I_c\right)}{2}, \tag{3.27}$$

$$I_a = \frac{2\pi\alpha\left(\cos^{-1}\alpha^2 - \alpha S_a\right)}{S_a^3}, \tag{3.28}$$

$$I_c = 4\pi - 2I_a, \tag{3.29}$$

$$I_{ac} = \frac{I_c - I_a}{3S_a^3}, \tag{3.30}$$

$$I_{aa} = \pi - \frac{3I_{ac}}{4}, \tag{3.31}$$

$$I_{ab} = \frac{I_{aa}}{3}, \tag{3.32}$$

$$\sigma = \frac{3K - 2\mu}{6K + 2\mu}, \tag{3.33}$$

$$S_a = \sqrt{1-\alpha^2}, \tag{3.34}$$

$$R = \frac{1-2\sigma}{8\pi(1-\sigma)}, \tag{3.35}$$

$$Q = \frac{3R}{1-2\sigma}, \tag{3.36}$$

$K_{c,k}$ is the bulk modulus of the soft components, estimated from nanoindentation measurements of Young's modulus and Poisson's ratio of clay minerals and kerogen, K is the effective bulk modulus of the rock components with high stiffness, and α is the aspect ratio assigned to the soft rock components.

3.2.3.2 Assessment of effective stiffness tensor in the lower Eagle Ford formation

The lower Eagle Ford formation is primarily well-laminated (Martin et al., 2011; Mokhtari et al., 2016), with and presents low vertical heterogeneity and low mechanical anisotropy (Chen Valdes et. al, 2016). Thus, I use Backus averaging for isotropic layers (Backus, 1962) to model an equivalent anisotropic layered medium and then estimate effective elastic properties. This model assumes that the rock is composed of isotropic layers, and therefore, used to model the laminated morphology present in the lower Eagle Ford formation. I use this model because it only requires two independent constant to describe each component, yet the effective medium is still assumed to be transversely isotropic. The well-log domain effective elastic stiffness coefficients (estimated using the inputs from nanoindentation results) C_{11}^{eff}, C_{12}^{eff}, C_{13}^{eff}, C_{33}^{eff}, C_{44}^{eff}, and C_{66}^{eff} are given by

$$C_{11}^{eff} = \left\langle a - f^2 c^{-1} \right\rangle + \left\langle c^{-1} \right\rangle^{-1} \left\langle f c^{-1} \right\rangle^2, \tag{3.37}$$

$$C_{12}^{eff} = \left\langle b - f^2 c^{-1} \right\rangle + \left\langle c^{-1} \right\rangle^{-1} \left\langle f c^{-1} \right\rangle^2, \tag{3.38}$$

$$C_{13}^{eff} = \left\langle c^{-1} \right\rangle^{-1} \left\langle f c^{-1} \right\rangle^2, \tag{3.39}$$

$$C_{33}^{eff} = \left\langle c^{-1} \right\rangle^{-1}, \tag{3.40}$$

$$C_{44}^{eff} = \left\langle d^{-1} \right\rangle^{-1}, \tag{3.41}$$

and

$$C_{66}^{eff} = \left\langle m \right\rangle. \tag{3.42}$$

where *a*, *b*, *c*, *f*, and *m*, are five independent elastic constants. Each component requires two independent elastic constants that are described by

$$a = c = \lambda + 2\mu, \tag{3.43}$$

$$b = f = \lambda, \tag{3.44}$$

and

$$d = m = \mu, \tag{3.45}$$

where λ and μ are the Lamé parameters of elasticity, given by

$$\lambda = \frac{\nu E}{(1+\nu)(1-2\nu)} \tag{3.46}$$

and

$$\mu = \frac{E}{2(1+\nu)}, \tag{3.47}$$

where ν is Poisson's ratio from nanoindentation tests. Then I analyze density and cross-dipole sonic slowness logs to estimate dynamic elastic stiffness coefficients, C_{ij}. Dynamic elastic stiffness coefficients C_{33}, C_{44}, and C_{55}, are estimated using the compressional, fast-shear, and slow-shear slowness measurements from the acoustic tools and bulk density measurements. C_{66} is estimated from borehole Stoneley slowness measurements (Frydman, 2010). The outcomes of nanoindentation tests are static measurements of elastic properties. These static elastic properties are used to estimate static stiffness coefficients which are required for geomechanical modelling (Holt et al., 2013). Therefore, I use empirical correlations obtained between laboratory-derived

dynamic and static elastic stiffness coefficients to estimate static elastic stiffness coefficients C_{33}, C_{44}, C_{55}, and C_{66} in the well-log domain. Elastic stiffness coefficients C_{11}, C_{13}, and C_{12} are then obtained using the correlations from core measurements of elastic properties. I calibrate well-log-based estimates of elastic stiffness coefficients C_{11}, C_{13}, C_{12}, and C_{33} to obtain static elastic properties at the well-log domain by solving the following system of equations (Podio et al., 1968), as follows

$$E_v = C_{33} - \frac{2C_{13}^{\ 2}}{C_{11} + C_{12}}, \tag{3.48}$$

$$E_h = C_{11} + \frac{C_{13}^{\ 2}\left(C_{12} - C_{11}\right) + C_{12}\left(C_{13}^{\ 2} - C_{12}C_{33}\right)}{C_{33}C_{11} - C_{13}^{\ 2}}, \tag{3.49}$$

$$\upsilon_v = \frac{C_{13}}{C_{11} + C_{12}}, \tag{3.50}$$

and

$$\upsilon_h = \frac{C_{33}C_{12} - C_{13}^{\ 2}}{C_{33}C_{11} - C_{13}^{\ 2}}, \tag{3.51}$$

where E_V and E_H are Young's moduli in the directions normal and parallel to the bedding plane, respectively, and v_v and v_h are the Poisson's ratio normal and parallel to the bedding plane, respectively.

Finally, I quantify the difference between effective elastic stiffness coefficients C_{11}^{eff}, C_{12}^{eff}, C_{13}^{eff}, C_{33}^{eff}, C_{44}^{eff}, and C_{66}^{eff} (estimated using the inputs from nanoindentation results), and estimates of dry elastic stiffness coefficients C_{11}^{d}, C_{13}^{d}, C_{12}^{d}, C_{33}^{d}, C_{44}^{d}, and C_{66}^{d} obtained via acoustic well logs and calibrated using core measurements. Furthermore, I quantify the difference between static measurements of

elastic properties from core measurements and nanoindentation-based estimates of effective elastic properties at the well-log domain.

3.3 Field Example No.1: The Haynesville Formation

The Haynesville formation is composed of clay-rich (illite and chlorite) and carbonate-rich intervals, with pyrite, calcite-filled cracks, and shells present. Therefore, this formation is classified as calcareous mudstones or calcareous/argillaceous mudstones (Suarez-Rivera et al., 2013). The porosity and total organic content are 8-12%, and 1-8.5%, respectively (Hammes et al., 2011). I select rock samples from the laminated peloidal calcareous mudstone facies, because it is the most abundant facies in the Haynesville formation (Hammes et al., 2011). Furthermore, this facies was selected as the best rock class for production, based on rock classification using petrophysical, compositional and elastic properties (Aranibar et al., 2013). This facies is characterized for either having siliciclastic-or carbonate-dominated grains. Moreover, this facies is laminated, with parallel beddings composed of bioclasts, peloids, clay, organic deposits and detrital calcite. The laminated mudstone is composed of organic laminae, sponge spicules, peloids, pellets, and fragments of bivalve shells and equinoderms, which are aligned along the bedding planes. The siliciclastic-dominated areas are primarily composed of detrital quartz, feldspar silt and clay minerals. The TOC in this facies varies between 2% and 5%.

3.3.1 Evaluation of elastic properties in the micro-scale domain

Nanoindentation mechanical tests are carried out over individual mineral components and kerogen in the Haynesville formation samples. The laminated peloidal calcareous mudstone facies is characterized as laminated with components deposited along the bedding. Therefore, I was able to target kerogen, clay and non-clay minerals that were deposited parallel to the bedding plane. Furthermore, I observed that the intermixed layers of illite and chlorite, illite, quartz, calcite, and kerogen particles were large enough for individual indentation, as shown in **Figure 3.4**. For indentation of kerogen, a maximum axial load of 5.0 mN was used, which resulted in indenter penetration depths of less than 400 nm. For the clay and non-clay minerals, the maximum axial loads applied were 15 mN and 100 mN, respectively. I used an indentation rate of 0.17 mN/s, for all mudrock components.

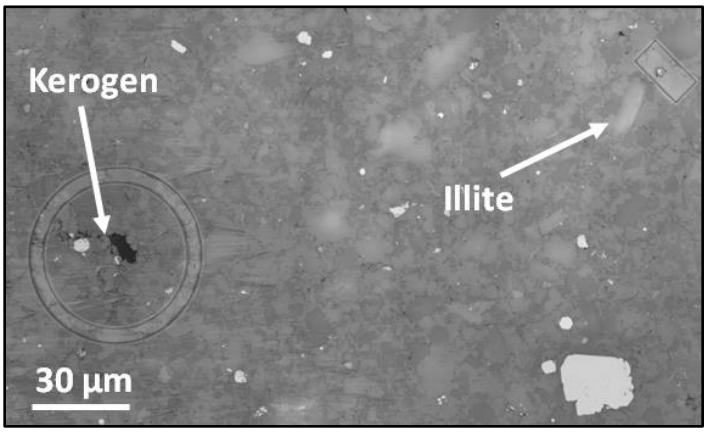

Figure 3.4: Haynesville formation: Individual component indentation carried out over kerogen and mica mudrock components (confirmed via EDS).

Table 3.1 shows a summary of the measured Young's modulus and hardness for individual mineral components in samples from the Haynesville formation. Young's modulus of illite varies from 9.0 GPa-18.1 GPa, with an average value of 13.1 GPa. The intermixed layer of illite and chlorite has a measured Young's modulus of 6.6 GPa. However, I measured a higher variability in Young's modulus and hardness for intermixed layers of illite and chlorite than in measurements of Young's modulus for individual illite components. This higher variability in Young's modulus could be attributed to variable quantities of illite and chlorite, and to variable surface areas of intermixed layers in the tested rock samples. I also measured Young's modulus of kerogen, that ranged from 8.5-11.0 GPa, in kerogen deposits with similar size and thickness. The measured Young's modulus in quartz grains showed higher stiffness than the soft mineral components (clay and kerogen). I measured an average Young's modulus for quartz grains of 81.5 GPa, which varied within the range of 73.4-91.5 GPa.

For a mixture of mineral components, I measured an average Young's modulus of 32.7 GPa, and an average hardness of 1.2 GPa from the indentation tests in the rock samples from the Haynesville formation. A higher variability in measured Young's modulus in the mixture of mineral components was noticed when the imprint of the indentation was placed within grain boundaries. Furthermore, the measured Young's modulus was less variable when the indented surface was mostly composed of a homogeneous mixture of minerals at similar mineral concentrations.

Table 3.1: Haynesville formation: Young's modulus, E, and hardness, H, estimated using nanoindentation tests.

Rock Component	***E*** **(GPa)**	***H*** **(GPa)**
Calcite	71.6±1.1	3.8±0.1
Illite	13.1±1.1	1.0±0.1
Illite and chlorite (intermixed layers)	6.6±1.7	0.4±0.2
Kerogen	9.3±0.8	0.7±0.2
Quartz	81.5±2.7	3.2±0.3

Figure 3.5 shows indented areas from a rock sample in the Haynesville formation, where the indentation imprint lies over (a) quartz grain, (b) boundary of quartz grain and intermixed layer of illite and chlorite, and (c) homogeneous mixture of quartz, illite, and chlorite. SE images are shown on the left-hand side, and EDS surface maps are shown in the right-hand**.** The EDS surface maps were acquired using a 15 kV accelerating voltage, 3.2 nA beam current, and 200 microseconds dwell time. The mudrock components in the analyzed samples are quartz, illite/chlorite, kerogen, and smaller quantities of apatite and pyrite. The dominant elements detected via EDS include aluminum (Al), silicon (Si), oxygen (O), and calcium (Ca). Combined interpretation of the SEM images and single-element EDS, infer that the indented areas are majorly composed (in volume percent) of quartz (approximately 50%), calcite (approximately 10%), and clay minerals (approximately 40%). **Table 3.2** lists the average relative difference between $E_{measured}$ and E_{sca} for the examples displayed in **Figure 3.5**. The results indicate that this relative difference is less than 10.7%. Furthermore, the difference in Young's modulus between these three examples is less than 9%. I also

observed that quartz grains restrained propagation of the area of stress influence of each indentation (brightest areas in the SE images). This could be evidence that measuring elastic properties at the micro-scale domain could carry a high degree of variability in heterogeneous mudrocks. Therefore, the indented surfaces must fulfill the requirements for the REV, to ensure that the mechanical properties measured at the micro-scale domain are representative of mechanical properties of the rock.

Figure 3.6 shows an indented area from the Haynesville formation, in which the volumetric compositions of minerals are different from those previously shown in **Figure 3.5**. In **Figure 3.6**, the indented area is composed mostly of quartz and calcite, a small concentration of clay minerals, and the indentation imprint is located in the boundary of quartz and calcite grains. In this example, the measured Young's modulus is 73.8 GPa, which is different from the average measured values for the Haynesville formation examples. It can be observed that the imprint left after indentation was considerably smaller than the previous examples, and did not extended beyond the grain boundary into the clay minerals. The high Young's modulus and the reduced residual indentation imprint in this example comprised only the stiffest minerals (quartz and calcite), and therefore, it is not representative of the mechanical behavior of the rock. As a result, these tests were not taken into consideration to calculate the average effective Young's modulus reported in Table 3.1. Furthermore, I did not use the indentation results from a mixture of mineral components to evaluate elastic properties at the well-log domain, because the results show high variability in effective elastic properties.

Table 3.2: Haynesville formation: average relative difference between $E_{measured}$ and E_{sca} for the examples displayed in Figure 3.5, for a mixture of mineral components.

Sample ID	$E_{measured}$ (GPa)	E_{sca} (GPa)	e_E (%)
(a)	33.6	35.2	4.4
(b)	29.5	33.0	10.7
(c)	36.5	35.7	2.2

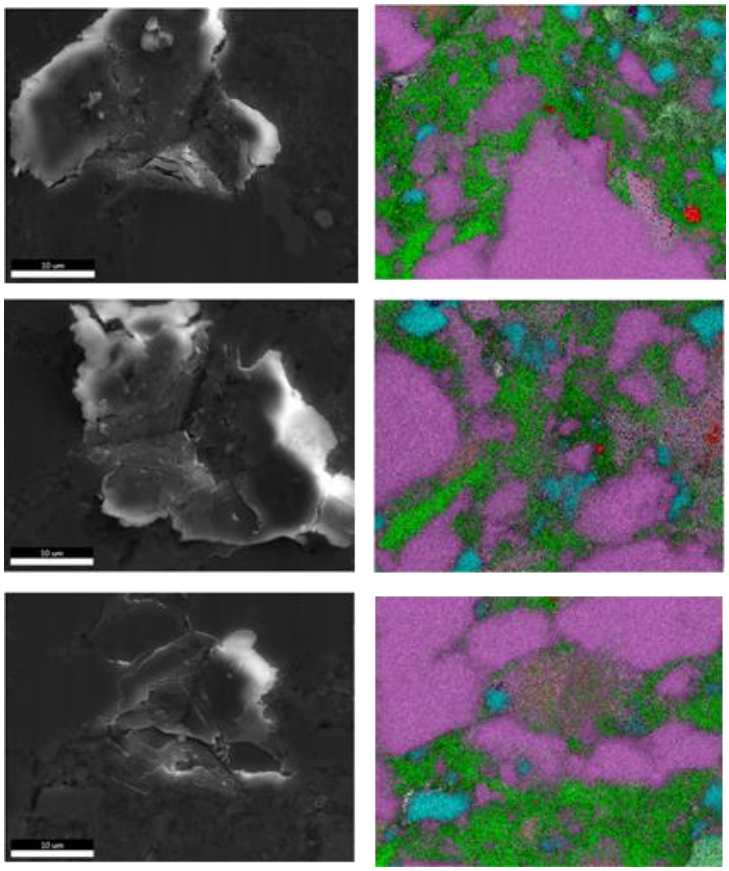

Figure 3.5: Haynesville formation: Mixture of mineral components, where the indentation imprint is located at (a) quartz grain, (b) boundary of quartz grain and intermixed layer of illite and chlorite, and (c) mixture of quartz, illite and chlorite. The SE images (left) show the sample topography after indentation. The right-hand side images show EDS surface maps acquired after nanoindentation tests.

3.3.2 Multi-Scale evaluation of elastic properties

The nanoindentation measurements of elastic properties of individual mudrock components reported in Table 3.1 were applied as inputs to estimate effective elastic stiffness coefficients at the well-log domain.

Figure 3.7 shows conventional well logs, acoustic logs, and estimated volumetric concentrations of minerals, elastic stiffness coefficients, and elastic properties in the lower Eagle Ford formation. Tracks 8 through 13 in Figure 3.7 illustrate the difference between estimates of effective elastic stiffness coefficients obtained using the inputs from nanoindentation results (C_{ij}^{eff}), and well-log-based elastic stiffness coefficients estimated using acoustic logs (C_{ij}^{d}). I observed average relative differences of 17.9%, 17.3%, 31.2%, 27.2%, 14.1%, and 17.6% in estimates of elastic stiffness coefficients C_{11}, C_{13}, C_{33}, C_{44}, and C_{66}, respectively.

Then I estimated the variability of C_{ij}^{eff} caused by the variability of elastic properties of soft mudrock components (e.g. clay minerals and kerogen) measured via nanoindentation tests, and shown in Table 3.1. Variabilities of 25% and 9% from the average values of elastic properties of clay minerals and kerogen, respectively, impact estimates effective elastic stiffness coefficients C_{11}^{eff}, C_{13}^{eff}, C_{33}^{eff}, C_{44}^{eff}, and C_{66}^{eff} by 15.9%, 25.9%, 28.8%, 13.6%, and 13.2%, respectively.

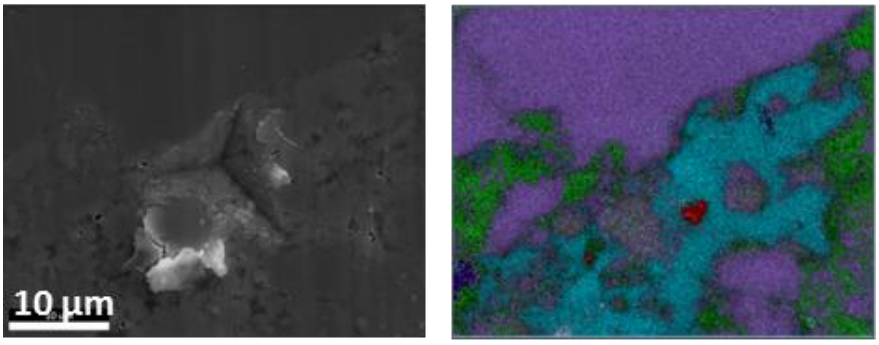

Figure 3.6: Haynesville formation: Mixture of mineral components, where the indentation imprint is located over the boundary of calcite and quartz grains**.**

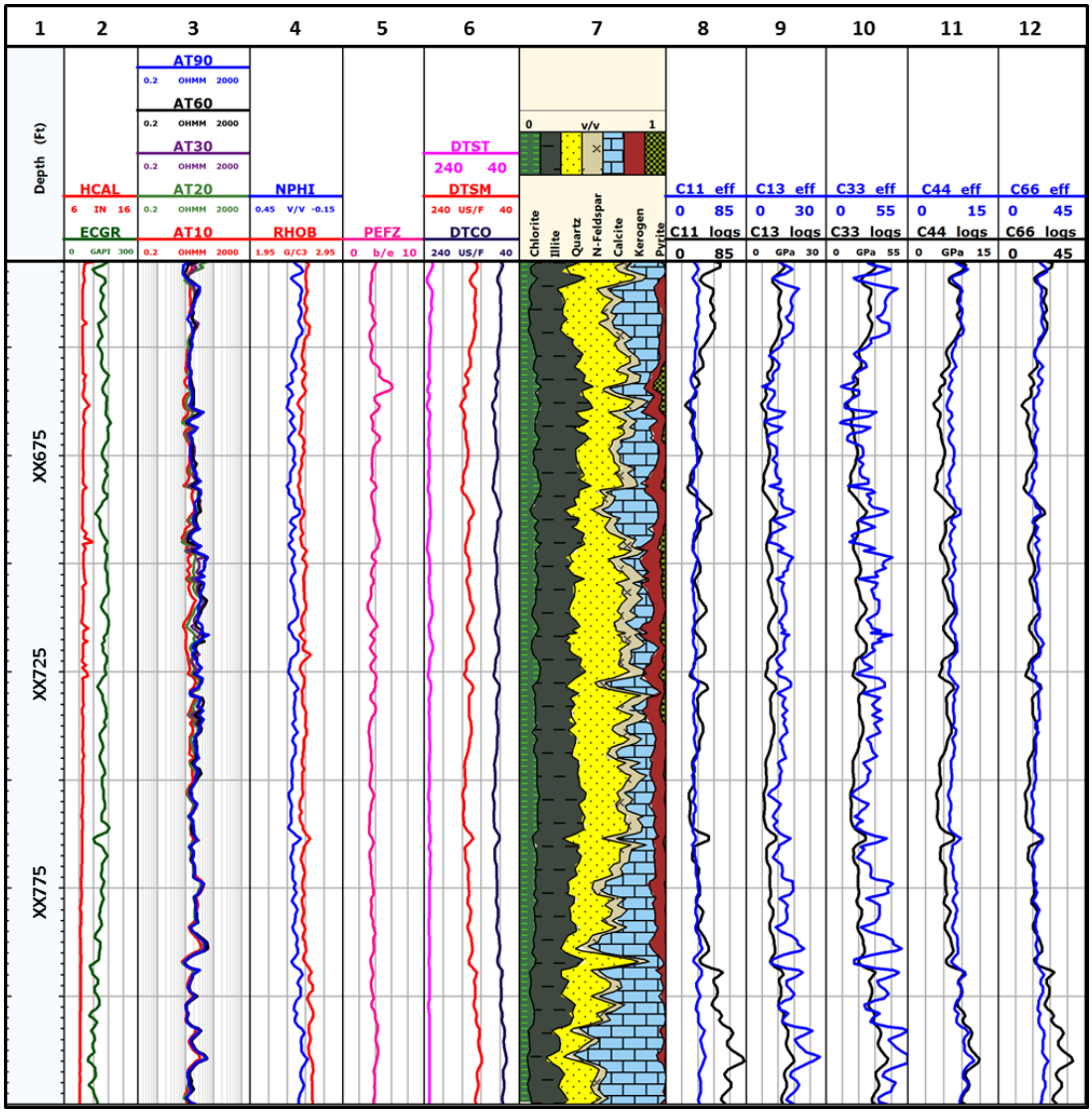

Figure 3.7: Haynesville formation: Conventional well logs, estimates of petrophysical/ compositional properties and elastic stiffness coefficients and elastic properties. Tracks from left to right include, Track 1: depth; Tracks 2-6: GR/Caliper, apparent resistivity logs, neutron porosity, bulk density, PEF, and acoustic-wave slowness logs; Track 7: estimates of volumetric concentrations of kerogen, n-feldspar, calcite, quartz, chlorite, pyrite and illite; and Tracks 8-12: elastic stiffness parameters in the well-log-domain estimated using the results from nanoindentation tests as inputs (Cij_eff), and from acoustic well logs (Cij_logs).

3.4 Field Example No.2: The Lower Eagle Ford Formation

The lower Eagle Ford formation is calcareous with argillaceous limestone beds, and a planar and laminated morphology. This formation is composed of illite, smectite, kaolinite, and quartz. The lower Eagle Ford formation is characterized by skeletal grains, which are planktonic Globigerinid-like forams and calcispheres. The porosity and total organic content are approximately 7-15% and 2-7%, respectively (Smith et al. 2013). The rock samples for nanoindentation tests were collected from the Lozier Canyon, an outcrop location west of Del Río, Texas.

3.4.1 Evaluation of elastic properties in the micro-scale domain

The experimental protocol used in the Haynesville formation field example was applied to measure elastic properties of individual mudrock components. **Table 3.3** shows a summary of the measured Young's modulus and hardness for individual mineral components in samples from the lower Eagle Ford formation.

In the lower Eagle Ford formation example, I was not able to target individual clay minerals, due to their small size. Hence, I indented mixed areas of illite and kaolinite clay minerals, where the Young's modulus varies from 20.0 GPa to 39.9 GPa, with an average value of 29.4 GPa. Pal Bathija et al. (2008) reported that the Young's modulus from nanoindentation experiments were 2.6 GPa for kaolinite, and 7.3 GPa for montmorillonite. Their molecular simulation results for Young's modulus of montmorillonite are documented in the range of 4.8 to 16.2 GPa. However, they did not report nanoindentation measurements of Young's modulus for illite and/or a mixture of illite and kaolinite. Katahara (1996) reported estimates of illite elastic properties

calculated via measurements of ultrasonic wave velocities. Their estimated value of Young's modulus was 11.4 GPa. These estimates, however, were made under the assumption that the acoustic wave propagation throughout the mineral is elastic.

In the samples for the lower Eagle Ford formation, kerogen deposits were smaller than the minimal area of contact of the tip indenter (5 μm x 5 μm). Therefore, I did not measure elastic properties of kerogen in this formation. Kumar et al. (2012) and Mba et al. (2010) reported Young's modulus of kerogen in samples from the Woodford and the Bakken formations via nanoindentation that ranged within 1.9 to 15 GPa, and 15 to 25 GPa, respectively. Zeszotarksi et al. (2004) measured Young's modulus in isolated kerogen from the Woodford formation within the range 10.5-11.1 GPa. Furthermore, Zhang and Jamili (2015) estimated a Young's modulus of 3.5 GPa in Green River oil shale using molecular simulations.

I measured an average value of 80.4 GPa for Young's modulus in quartz grains, with values within the range 72.1-87.8 GPa. Bass and Weidner (1984) reported that Young's modulus for quartz crystals at room pressure and temperature within range 79.4-102.9 GPa. Heyliger et al. (2003) also reported values of Young's modulus in natural quartz spheres within the range 79.4 to 102.8 GPa. The results from previous publications are in agreement with my experimental results.

3.4.2 Multi-scale evaluation of elastic properties

I applied the nanoindentation measurements of elastic properties of individual mudrock components reported in **Table 3.3** as inputs to equations 37-45, to estimate effective elastic stiffness coefficients in well-log domain.

Figure 3.8 shows conventional well logs, acoustic logs, and estimated volumetric concentrations of minerals, elastic stiffness coefficients, and elastic properties in the lower Eagle Ford formation. Tracks 8 through 13 in Figure 3.8 illustrate the difference between estimates of effective elastic stiffness coefficients obtained using the inputs from nanoindentation results (C_{ij}^{eff}), and well-log-based elastic stiffness coefficients estimated using acoustic logs (C_{ij}^{d}). I observed average relative differences of 30.4%, 15.1%, 32.9%, 22.4%, and 6.6% in estimates of elastic stiffness coefficients C_{11}, C_{13}, C_{33}, C_{44}, and C_{66}, respectively. I also included the variability of individual mudrock components from nanoindentation to estimate effective elastic properties at the well-log domain. A variability of 12% in elastic properties of clay minerals measured via nanoindentation impacts the magnitudes of effective elastic stiffness coefficients C_{11}^{eff}, C_{13}^{eff}, C_{33}^{eff}, C_{44}^{eff}, and C_{66}^{eff} by 9.3%, 6.8%, 7.2%, 11.0%, and 9.9%, respectively.

Table 3.3: Lower Eagle Ford formation: Young's modulus, *E*, and hardness, *H*, estimated using nanoindentation tests.

Rock Component	***E* (GPa)**	***H* (GPa)**
Calcite	68.8±3.1	2.5±0.3
Illite and Kaolinite	29.4±3.4	0.4±0.1
Quartz	80.4±4.5	3.2±0.3

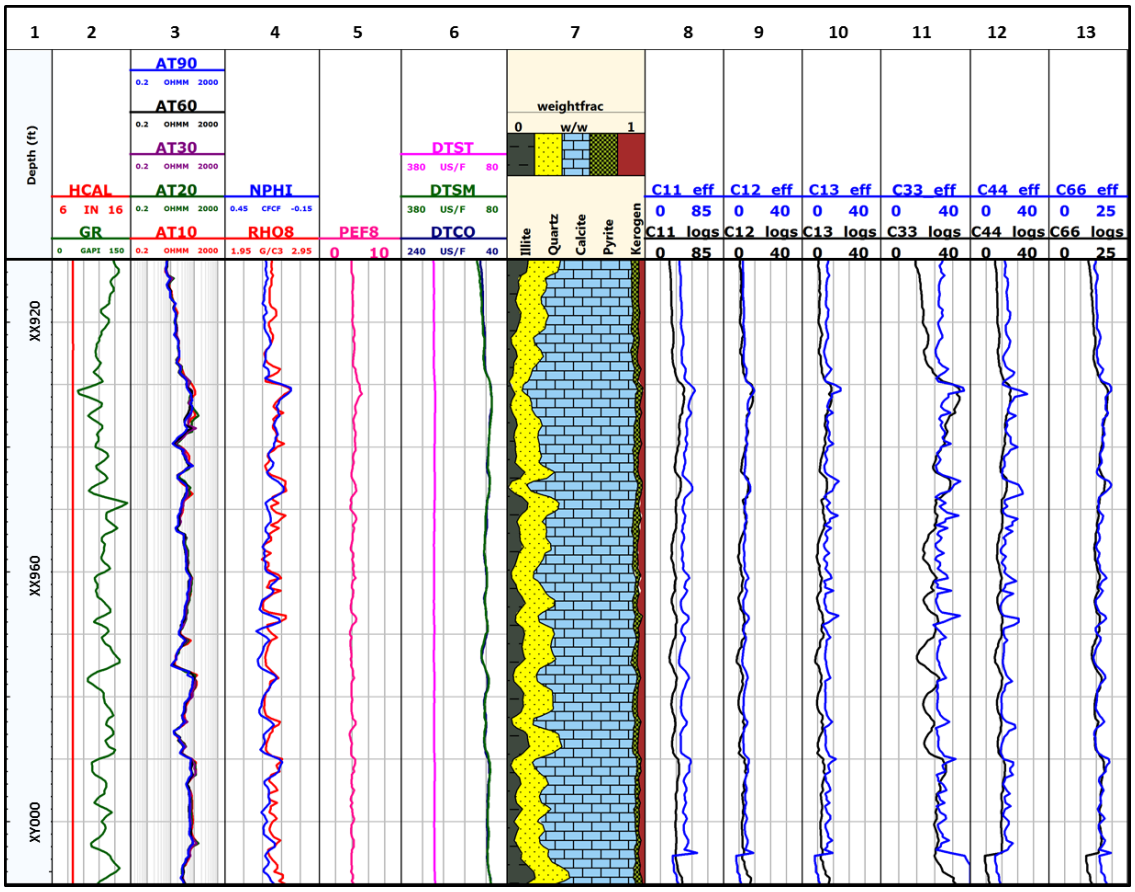

Figure 3.8: Lower Eagle Ford formation: Conventional well logs, estimates of petrophysical/ compositional, and.elastic stiffness coefficients and elastic properties. Tracks from left to right include, Track 1: depth; Tracks 2-6: GR/Caliper, apparent resistivity logs, neutron porosity, bulk density, PEF, and acoustic-wave slowness logs; Track 7: estimates of volumetric concentrations of kerogen, calcite, quartz, pyrite and illite; and Tracks 8-13: elastic stiffness parameters in the well-log-domain estimated using the results from nanoindentation tests as inputs (Cij_eff), and from acoustic well logs (Cij_logs).

3.5 Discussion

The results from the nanoindentation experiments showed that the variability in measurements of elastic properties of individual mudrock components is related to the stiffness of the component. The soft (e.g. clay minerals and kerogen) and high-stiffness non-clay minerals (e.g. quartz and calcite) experienced relatively higher and lower variability in elastic properties, respectively. Furthermore, SEM images acquired post-indentation, in addition to final deformation curves due to the applied load, indicated that the plastic deformation of the targeted mudrock components is non-homogeneous. The targeted clay minerals with immediate contiguity to large quartz grains presented higher values of Young's modulus, compared to the targeted ones that were located next to smaller quartz grains or that presented a larger surface contact area, by at least 15%. This could be explained by strain incompatibility between clay and non-clay minerals, which occurs at the grain boundaries. As a result of this incompatibility, the indented clay minerals were constrained from freely deforming in the surface perpendicular to the indentation direction, which could potentially increase their stiffness and therefore, they present higher magnitudes of elastic properties. Increasing the number of indentations in clay minerals, could potentially reduce the variability in the measurements. Furthermore, using a smaller indenter tip will reduce the surface contact area between the indenter tip and the target clay minerals. A smaller surface contact area results in a smaller area of influence of the indentation, which could help reduce the influence of strain incompatibility in the measurements of elastic properties of individual clay minerals.

Then I used the results from the nanoindentation experiments, in addition to the results from the multi-mineral analysis performed at the well-log domain, as inputs to estimate effective elastic properties at the well-log domain in both formations. In the case of the Haynesville formation, I picked samples from the laminated peloidal calcareous mudstone facies, where clay minerals and kerogen are deposited along the bedding plane. I carried out the tests in the direction perpendicular to the bedding plane. Therefore, I could only to target the individual mudrock components in the direction perpendicular to the bedding plane, in which their surface area is larger than the indenter tip. I considered the Eshelby-Cheng inclusion model for transversely isotropic media as reliable to resemble the stiffness tensor in the Haynesville formation. Furthermore, Eshelby-Cheng models better assimilate the resistance to deformation due to the stresses applied parallel to the bedding plane, because it takes into account the anisotropy introduced by the orientation of clay minerals and kerogen. In the case of the lower Eagle Ford formation, I used Backus averaging model due to observed thin limestone layers and laminated morphology. Furthermore, clay minerals in the Eagle Ford formation do not show a preferred orientation, as opposed to the Haynesville formation. Clay preferred orientation vanishes at micro-scale when volumetric concentration of clay is less than 30% (Hone and Zoback, 2013). Therefore, I picked Backus averaging model to estimate effective elastic stiffness coefficients at the well-log domain, due to the reliability of this model to represent a stratified medium that is composed of anisotropic thin layers (Backus, 1962).

3.6 Conclusions

To address the uncertainties involved in estimates of effective elastic properties of organic-rich mudrocks, I investigated the variability of elastic properties of rock components at the micro-scale domain and quantified its impact on the estimates in the well-log domain. I conducted nanoindentation experiments, combined with SEM and EDS analysis, core-scale measurements of elastic properties and applied well logs to perform a multi-scale evaluation of mechanical properties in the Haynesville and lower Eagle Ford formations. I quantified uncertainties in measurements of elastic properties of soft rock components such as clay minerals and kerogen, and in mixtures of mudrock mineral components at the micro-scale domain. I reported that Young's moduli of individual clay minerals when located adjacent to stiff rock components (e.g., large quartz grains) up to 25% higher, compared to the cases where they are located adjacent to other clay minerals and other smaller non-clay minerals. This higher stiffness could be caused by grains of non-clay minerals that restrained lateral deformation of clay minerals, which reduced stress influence surface area under each indentation. This behavior was also observed in indentation over mixtures of mineral components. SE images also provided a clear view of different deformation behaviors undergone after each indentation test, due to the uncoupling of mudrock components. This could indicate the variability and a source of variability in measured elastic properties in mudrocks.

I also quantified the differences between estimates of elastic stiffness coefficients from static core measurements and well-log-based estimates of effective elastic stiffness coefficients obtained using the inputs from nanoindentation results, in which I estimated

differences up to 33%. The method applied in this chapter can help reduce the uncertainties involved in the evaluation of effective mechanical properties of mudrocks, by quantifying the variability in distribution and interaction between kerogen, clay and non-clay minerals in the micro-scale domain. Furthermore, results from nanoindentation tests can be used to enhance assessment of effective elastic properties in the well-log domain, when availability of core samples is limited. Cuttings will be sufficient for performing nanoindentation tests. These micro-scale tests can be used as inputs to well-log-based models to enhance evaluation of mechanical properties in formations with complex lithology such as organic-rich mudrocks.

CHAPTER IV

QUANTIFYING THE IMPACT OF THERMAL MATURITY ON ELASTIC PROPERTIES OF KEROGEN

Direct measurements of elastic properties of kerogen using static methods is challenging due to its small concentration and complex distribution within organic-rich mudrocks. Furthermore, the effects of thermal maturation on elastic properties of kerogen are not well understood. The primary objective of this chapter is to quantify the impact of thermal maturity on elastic properties of kerogen. I measure elastic properties of isolated kerogen samples, at the micron-scale level of investigation. I carry out nanoindentation tests on compacted type II and type III kerogen samples. These samples are prepared at four different levels of synthetic thermal maturation. Then, I quantify the impact of kerogen thermal maturity on effective elastic properties in mudrocks. Furthermore, I evaluate the relationship between elastic properties, hydrogen index, and electrical resistivity in the synthetically-matured kerogen samples.

The results of the laboratory measurements show that Young's modulus varies with thermal maturity of kerogen, where I observed that the measured values in heat-treated kerogen samples differ from the measurements carried out in untreated kerogen. I reported the lowest values of Young's modulus in the heat-treated kerogen samples in which the highest electrical resistivity and hydrogen index were reported. The method applied in this chapter enables a better understanding of the effects of thermal maturation of kerogen on its mechanical properties in organic-rich mudrocks.

The measured mechanical properties helps understand the variability of elastic properties of kerogen due to changes in thermal maturity. Furthermore, the findings presented in this chapter can potentially improve well-log-based assessment of rock mechanical properties in formations with high organic content.

4.1 Introduction

Organic matter (i.e. kerogen and bitumen) directly influences acoustic anisotropy, and for instance, elastic properties in organic-rich mudrocks (Vernik and Nur, 1992). Including kerogen as an independent variable results in higher accuracy in estimates of elastic properties, porosity, and lithology from joint interpretation of acoustic-wave velocities and other well logs. However, direct measurements of elastic properties of kerogen are scarce and highly variable due to low volumetric concentrations, complex distribution and variability in kerogen porosity in organic-rich mudrocks.

Yan and Han (2013) carried out measurements of ultrasonic velocities in isolated samples belonging to the Green River shale, and inverted bulk modulus of kerogen using fluid substitution and averaging methods. They estimated average bulk modulus is 3.5-5.0 GPa, and shear modulus of approximately half the average bulk modulus. The estimates reported in this study correspond to dynamic measurements, made under the assumptions of linear elasticity in cemented rock. Furthermore, the aforementioned publication showed that kerogen has significantly lower stiffness compared to other mudrock components (e.g. quartz, calcite and pyrite). This difference in stiffness could result in nonlinear deformations of kerogen (i.e.

viscoelastic behavior) under high-magnitude loads, which might not be evaluated accurately, if ultrasonic velocities are used to estimate elastic properties. Hence, measuring elastic properties using direct methods such as nanoindentation could improve estimates of elastic properties of kerogen.

Zeszotarski et al. (2004) performed measurements of hardness and elastic modulus at room temperature, on kerogen from the Woodford shale, combining nanoindentation and atomic force microscopy (AFM) techniques. They observed an average elastic modulus of 10.5-11.1 GPa. Kumar et al. (2012) and Mba and Prasad (2010) reported Young's modulus of kerogen in samples from the Woodford and the Bakken formations via nanoindentation that ranged within 1.9-15 GPa and 15-25 GPa, respectively. Furthermore, Zhang and Jamili (2015) estimated a Young's modulus of 3.5 GPa in Green River oil shale using molecular simulations. These publications, however, do not consider the effects of thermal maturity on elastic properties of kerogen.

Prasad et al. (2009) found that compressional velocity and impedance increase with thermal maturation, and are inversely proportional to hydrogen index. Zargari et al. (2011) carried out nanoindentation measurements to quantify the effects of thermal maturity on mechanical properties of organic-rich shales. They subjected the organic-rich shale samples to hydrous pyrolysis, and found a reduction in Young's modulus of thermally immature samples. Allan et al. (2016) characterized pyrolysis-induced evolution of elastic properties in mudstone samples, where they documented that thermal maturation increases mechanical anisotropy.

Previous publications documented alteration in chemical and molecular structure of kerogen as its thermal maturity increases. Kerogen produces bitumen and hydrocarbons during thermal maturation, its aromaticity increases, and graphitization can happen (Yang and Heidari, 2016a, 2016b; Yang et al. 2016, Romero-Sarmiento et al.; 2014; Spötl et al., 1998). Yang and Heidari (2016a, 2016b) and Yan et al. 2016 showed that the alteration in chemical structure of kerogen affects its electrical conductivity and density.

The impact of thermal maturation on elastic properties of kerogen has not been studied thoroughly. Emmanuel et al. (2016) found that vitrinite reflectance and Young's modulus of organic matter in shales increases at different levels of thermal maturation, according to burial depth. This study, however, was performed on naturally-matured samples at room temperature on type II kerogen samples, at three different levels of thermal maturation. Zargari et al. (2011) also completed a similar study in kerogen samples from the Bakken formation, where they found that elastic modulus in kerogen was lower in mature samples.

The primary objective of this chapter is to quantify the impact of thermal maturity on elastic properties of kerogen. I measure elastic properties of isolated kerogen in micron-scale level of investigation to directly quantify the elastic properties of kerogen. I perform nanoindentation tests on compacted kerogen samples, at four different levels of thermal maturity in synthetically-matured samples from four mudrock formations (i.e. Formations A, B, C, and D). Then I evaluated the differences between elastic properties of kerogen at different levels of thermal maturity.

Furthermore, I perform a sensitivity analysis to quantify the impact of variation in elastic properties of kerogen due to thermal maturity, on effective elastic properties of organic-rich mudrocks.

4.2 Method

The first step consists of extracting and isolating kerogen from mudrocks to obtain kerogen powder. I compact the kerogen powder into cylindrical discs to facilitate measurements of elastic properties. In the next step, I synthetically mature the kerogen samples using heat treatment. Then I carry out nanoindentation tests to obtain mechanical properties of the synthetically-matured kerogen samples at different levels of thermal maturity in four mudrock formations (i.e. Formations A, B, C, and D). Next, perform sensitivity analysis is performed at depth intervals with different levels of organic richness, to quantify the impact of thermal maturity of kerogen on effective elastic properties in one of these formations (i.e. Formation B). The following sections describe the detailed procedures used to quantify the impact of thermal maturity on elastic properties of kerogen and organic-rich mudrocks.

4.2.1 Kerogen Isolation

I follow the kerogen isolation procedure reported by Yang et al. (2016). In this technique, mudrock samples are first crushed and mechanically sieved. The mudrock powder is then used to obtain kerogen powder through chemical treatments. Bitumen, minerals and free hydrocarbons are removed chemically using chloroforms, hydrochloric (HCl), and hydrofluoric (HF) acid treatments (Durand and Nicaise, 1980;

Vandenbroucke, 2003). Chloroform is used to remove free hydrocarbons and bitumen. HCl and HF acids are used to remove carbonates and silicates, respectively.

The next step includes pyrite separation. Pyrite is removed from the samples using density-based separation by zinc bromide (Kinghorn and Rahman, 1980; Kinghorn and Rahman, 1983). The samples, treated with HCl and HF acids, are grinded further to increase the surface contact area between the solid grains and a zinc bromide solution. The mixture is then separated using centrifugation at a rate of 2000 rpm. A visible separation of the mixture in the test tubes indicates a successful centrifugation. The sink fraction contains heavy minerals and the float fraction contains kerogen solids. The isolated kerogen is then filtered, rinsed, and dried.

The removal of minerals is then confirmed via X-ray fluorescence (XRF) analysis on mudrock and isolated kerogen samples. A significant reduction in silicon, potassium, calcium, and aluminum obtained from XRF analysis indicates a successful removal of minerals. XRF analysis results indicate that the compacted kerogen samples contain a small amount of iron disulfide solids. Therefore, the measurements of mechanical properties in the compacted kerogen packs are corrected for the impact of the presence of pyrite. This correction is described in the "Evaluation of Mechanical Properties of Kerogen" section.

4.2.2 Sample preparation

The sample preparation procedure includes (a) mechanical compaction and (b) synthetic maturation. The isolated kerogen powder samples were first mechanically compacted using a uniaxial loading frame. An axial pressure of approximately 100 psi

was applied over disk-shaped molded kerogen, with a surface area of 4.9-5.4 cm^2, and an average cross-sectional thickness of 2.1 mm. The molded kerogen sample is then extruded from the mold using a vise, and then segmented into 4-6 pieces prior to heat treatment.

Then I synthetically matured the compacted kerogen samples to 150ºC, 300ºC and 425ºC, using a heating device within an X-ray diffraction (XRD) instrument, to recreate thermal maturation of kerogen. Table 4.1 shows Rock-Eval pyrolysis analysis performed in isolated kerogen samples from Formation B and Formation D showing the relationship between heat-treatment temperatures for synthetic thermal maturation, hydrogen index, and T_{max} (Yang et al. 2016). To achieve synthetic thermal maturation, I increased the temperature in the samples at a constant rate of 4ºC/minute, from room temperature to the target heat treatment temperature. Then I isothermally heated the samples for an hour, to finally decrease the temperature at the same constant rate of 4ºC/minute, to achieve a final room temperature of 30 ºC.

Table 4.1: Relationship between heat-treatment temperature, T_{max}, and hydrogen index (HI) in formations B and D

Heat Treatment Temperature (°C)	**T_{max} (°C)**		**Hydrogen Index (mg hydrocarbon/g organic carbon)**	
	B	**D**	**B**	**D**
25	408	426	41	603
150	407	428	34	604
300	410	421	26	422
425	459	457	1	76

4.2.3 Mechanical tests at the micron-scale level of investigation

I carry out nanoindentation mechanical tests on the heat-treated kerogen samples at room temperature. Between 50 and 100 indentations are completed in each sample, at a regular spacing of 75 μm, using a Berkovich indenter (Berkovich, 1950). From the nanoindentation tests, a curve is obtained that represents the displacement of the material under the indenter tip, as a result of an applied axial load P. For these experiments, I apply maximum axial loads of 5 mN and 10 mN at a constant rate of 0.167 mN/s, and unload at the same constant rate. The applied load as a function of displacements provides information about elastic and plastic properties of the kerogen samples, such as Young's modulus and hardness.

Next, I estimated Young's modulus (E_{test}) and material hardness (H) using work-energy approach, which separates the elastic deformation from the non-recoverable, plastic deformation. The elastic and plastic deformations are represented by the area underneath the applied load P vs deformation curve. The elastic deformation represents the recoverable work (W_e), the plastic deformation region represents the permanent work (W_p), and the total work (W_t) is represented by the addition of the recoverable and permanent work. The recoverable (W_e) and the total work ($W_t = W_e + W_p$), are represented by the areas below the unloading and loading curve, respectively. Then I estimated elastic modulus, E_{test}, based on mechanical work-energy approach as described by Giannakopoulos and Suresh (1999).

4.2.4 Evaluation of mechanical properties of kerogen under the effects of thermal maturation

This subsection presents the steps followed to evaluate mechanical properties of kerogen. I estimate the porosity in the kerogen pack using X-ray micro computed tomography (micro-CT). It should be noted that kerogen pack porosity refers to the pore volume fraction in between kerogen powder and does not include kerogen porosity. Kerogen porosity is partially or fully destroyed during the kerogen isolation process. I corrected the measurements obtained from nanoindentation experiments for the presence of pyrite in the kerogen pack using Voigt upper bound model. Finally, I evaluate elastic properties of the kerogen pack using Hertz-Mindlin granular contact model.

4.2.4.1 Estimates of porosity in the kerogen pack

To evaluate the porosity in the compacted kerogen pack, $\phi_{k,pack}$, I use X-ray micro computed tomography (micro-CT) imaging technique. At this scale (<1 μm voxel size), I could quantify and segregate the volumes of solid kerogen and pore space, using a sequence of 2D images. Figure 4.1 shows an example of a 2D micro-CT image of a compacted kerogen pack, used in this dissertation. The green, red, and magenta regions represent kerogen, residual pyrite, and pore space in the compacted kerogen pack, respectively. The porosity in the kerogen packs are estimated by dividing the fraction of pore space present in the samples by the total area of the 2D image.

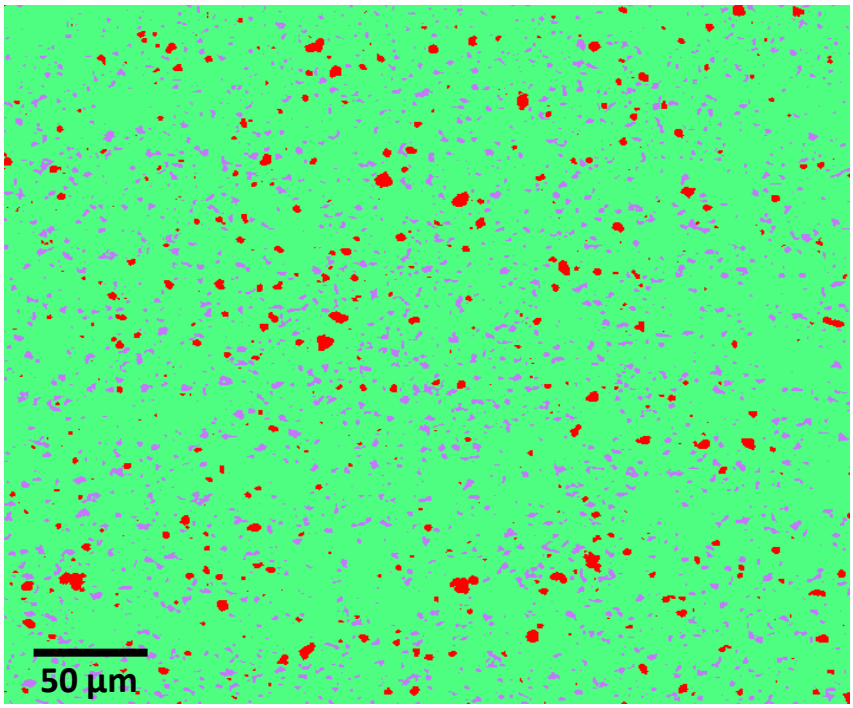

Figure 4.1: 2D micro-CT image of a compacted kerogen pack used in this study. The green, red, and magenta regions represent kerogen, residual pyrite, and pore space in the compacted kerogen pack, respectively.

4.2.4.2 Correction for the presence of pyrite in measurements of elastic properties of the kerogen pack

Pyrite is a mineral that is characterized for having very high stiffness and elastic moduli. Thus, the concentration of residual pyrite present in the compacted kerogen sample could impact measured mechanical properties of the kerogen pack. Therefore, I correct the estimates of elastic moduli of the kerogen pack for the small amount of pyrite in the samples.

To correct the results for the impact of pyrite, I estimate the weight concentration of pyrite in each kerogen pack via XRF analysis. The XRF analysis enables the quantification of weight concentration of iron (Fe) and sulfur (S) elements

which exist in pyrite mineral (FeS2) in the kerogen packs. Next, I use effective media models to correct the measured Young's modulus of the kerogen packs for the impact of pyrite. The strain in the kerogen packs is assumed to deform uniformly under the effect of an externally applied load. Hence, Voigt upper bound equation is used (Reuss, 1929), which assumes a state of uniform strain in the composite (Berryman, 1995), to estimate Young's modulus of kerogen in the compacted pack, $E_{kerogen,}$ via

$$E_{test}{}^{V} = f_{kerogen}E_{kerogen} + f_{pyrite}E_{pyrite} + \phi_{k,pack}E_{air}, \quad (4.1)$$

where $E_{test}{}^{V}$ represents upper bound for the Young's moduli of the kerogen pack, and represents the measurement of Young's modulus obtained from the nanoindentation tests. E_{pyrite} and E_{air} are the Young's moduli of pyrite and the pore space in the kerogen pack, respectively. $f_{kerogen}$ and f_{pyrite} represent the volumetric concentrations of kerogen and pyrite, respectively, estimated from XRF analysis. E_{pyrite} is obtained from previous nanoindentation tests on pyrite found in mudrock samples (Chen Valdes and Heidari, 2016). In the next step, I replace the fraction of pyrite from the mixture with properties of kerogen. The new elastic moduli of the kerogen pack after pyrite removal, $E_{test}{}^{*}$, is then calculated using Voigt upper bound equation, given by

$$E_{test}{}^{*} = f_{kerogen}{}^{*}E_{kerogen} + \phi_{k,pack}E_{air}, \quad (4.2)$$

where $f_{kerogen}{}^{*}$ represents the total volumetric concentration of the solids in the compacted kerogen pack (i.e. kerogen and pyrite). **Figure 4.2** shows the relative difference between the measured Young's moduli and Young's moduli after synthetic pyrite removal for the compacted kerogen samples documented in this paper. I observe

relative differences of 18%, 13%, 20% and 13% in Young's modulus before and after synthetic pyrite removal Formations A, B, C and D, respectively.

4.2.4.3 Assessment of elastic properties of kerogen

I use the corrected Young's modulus, E_{test}^{*}, and porosity of the kerogen pack, $\phi_{k,pack}$, to estimate elastic properties of kerogen, when the porosity of the kerogen pack approaches zero. These estimates will be later used as inputs to estimate effective elastic properties of an organic-rich mudrock (i.e., Formation B).

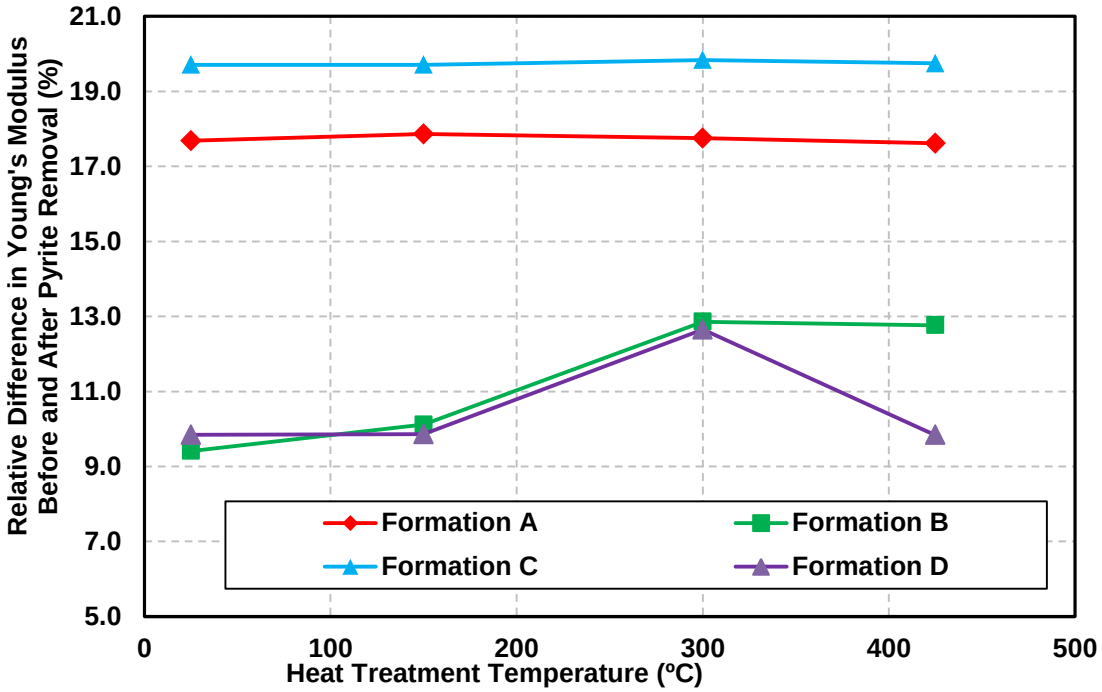

Figure 4.2: Relative difference between measured Young's moduli and Young's moduli after synthetic pyrite removal.

The Hertz-Mindlin granular contact model (Mavko et al., 2009) is used to correct Poisson's ratio of kerogen packs for the impact of kerogen pack porosity. The Hertz-

Mindlin model describes the grain to grain contact between two identical spheres that are pressed together, and it is generally used to describe elastic properties of pre-compacted granular materials. For a random, identical-sphere packing of frictionless spheres with a dry frame, I can first obtain Poisson's ratio of kerogen, $\upsilon_{kerogen}$, when porosity of the pack is equal to zero, via

$$\upsilon_{kerogen} = \frac{10\upsilon_{test}}{(1+6\upsilon_{test})}, \tag{4.3}$$

where υ_{test} is the Poisson's ratio, which is an input required for the nanoindentation tests. To input a correct υ_{test}, a series of identical tests are run on the kerogen samples under the same loading conditions and varying Poisson's ratio. The final value for υ_{test} is selected after a consistent E_{test} is achieved in multiple nanoindentation tests.

Due to low stiffness of kerogen, Reuss lower bound is used (Reuss, 1929) to estimate the bulk modulus of the kerogen. This model resembles mechanical properties in mixtures, composed of soft components. Then I calculate the bulk modulus of the kerogen, $K_{kerogen}$, via

$$K_{test} = \frac{E_{test}^{*}}{3(1-2\nu_{test})}, \tag{4.4}$$

and

$$\frac{1}{K_{test}} = \frac{\phi_{k,pack}}{K_{air}} + \frac{1-\phi_{k,pack}}{K_{kerogen}}, \tag{4.5}$$

where K_{test} is the measured bulk modulus of the kerogen pack, K_{air} is the bulk modulus of air at a constant temperature, and $\phi_{k,pack}$ is the porosity of the kerogen pack, obtained from micro-CT images. Then, the shear modulus, $\mu_{kerogen}$, and Young's modulus, $E_{kerogen}$, of kerogen are calculated when kerogen pack porosity approaches zero, for each heat-treated sample, via

$$\mu_{kerogen} = \frac{3\upsilon_{kerogen} K_{kerogen}}{1+\upsilon_{kerogen}}, \tag{4.6}$$

and

$$E_{kerogen} = \frac{9K_{kerogen}\mu_{k\,erogen}}{3K_{kerogen}+\mu_{kerogen}}, \tag{4.7}$$

respectively.

4.2.5 Sensitivity analysis: Impact of thermal maturity of kerogen on effective elastic properties of organic-rich mudrocks

In the next section, I perform a sensitivity analysis using field data from Formation B, to quantify the impact of thermal maturity and elastic properties of kerogen on effective elastic properties of mudrocks. First, I conduct well-log interpretation for assessment of water saturation, total porosity, and volumetric concentration of minerals and kerogen. Well logs including gamma ray (GR), electrical resistivity, density, neutron porosity, photoelectric factor (PEF), elemental capture spectroscopy (ECS), and compressional-wave slowness are used as inputs for petro physical and compositional evaluation of a given formation. Then I cross-validate the

estimates of minerals concentrations using X-Ray Diffraction (XRD). Additionally, I cross-validate estimates of total organic content (TOC) using core measurements.

The next step includes assessment of elastic properties using effective media models, at different volumetric concentrations of kerogen. I use self-consistent approximation model (SCA) (Berryman, 1995) to estimate effective elastic properties in formation B at different depths. Effective bulk and shear moduli are calculated by simultaneously by solving

$$\sum_{i=1}^{N} x_i \left(K_i - K_{sc}^{*} \right) P^{*i} = 0, \tag{4.8}$$

and

$$\sum_{i=1}^{N} x_i \left(\mu_i - \mu_{sc}^{*} \right) Q^{*i} = 0, \tag{4.9}$$

where K_{sc}^{*} and μ_{sc}^{*} are effective bulk and shear moduli obtained from the self-consistent approximation model, respectively. N is the number of rock component, x_i is volumetric concentration of the ith rock component, μ_i is the shear modulus of the ith rock component and K_i is the bulk modulus of the rock component i. P^*_i and Q^*_i are shape factors, which are functions of the shape and aspect ratios of each rock component. The shape factors are expressed as

$$P_i^{*} = \frac{1}{3} T^{(i)}{}_{jjll}, \tag{4.10}$$

and

$$Q_i^* = \frac{1}{5} T^{(i)}{}_{jljl} - P_i, \tag{4.11}$$

where $T^{(i)}{}_{jjll}$ and $T^{(i)}{}_{jljl}$ refer to the two invariants of Wu's tensor (Wu, 1966), which is a homogenization tensor between the far-field strain of the formation and the strain of the individual rock components. Then depth-by-depth Young's modulus of the formation, E_{eff}, is estimated via

$$E_{eff} = \frac{9K_{sc}\mu_{sc}}{3K_{sc} + \mu_{sc}}, \tag{4.12}$$

This model uses a background to represent rock components with medium to high stiffness (e.g. quartz, calcite, and pyrite). The idealized ellipsoidal inclusions recreate the soft components (e.g. clay minerals and kerogen). Furthermore, the self-consistent approximation model assumes that the material is linear elastic and isotropic, with ellipsoidal inclusions which is used to represent the soft rock components.

Inputs of elastic properties of individual minerals, measured via nanoindentation (Chen Valdes and Heidari, 2016) and shown in Chapter 3, as well as measurements of elastic properties of kerogen from the outcomes of this study are used as inputs to the SCA model. I perform depth-to-depth assessment of effective elastic properties, using the values of elastic properties of kerogen measured via nanoindentation, at different levels of thermal maturity. Then, the variability in elastic properties of kerogen samples due to different levels of thermal maturity is used to evaluate their impact on effective elastic properties of the formation via

$$e_E = \left| \frac{E_{eff\_ht} - E_{eff\_nht}}{E_{eff\_nht}} \right| \times 100, \tag{4.13}$$

where E_{eff_nht} is the effective Young's modulus of the formation, which uses measurements of elastic properties of kerogen performed in non-heat treated kerogen samples as inputs to the SCA model. E_{eff_ht} is the effective Young's modulus of the formation, which uses as inputs measurements of elastic properties of kerogen samples heat-treated to 150ºC, 300ºC and 425ºC.

4.3 Results

In this section, I present the evaluation of Young's modulus performed on kerogen packs from organic-rich mudrocks A, B, C, and D. The relationship between Young's modulus, hydrogen index, and electrical resistivity in the kerogen packs. Finally, I use data from formation B to evaluate the impact of thermal maturity of kerogen on effective elastic properties of the formation.

4.3.1 Evaluation of mechanical properties of kerogen

Figure 4.3 shows Young's modulus of isolated kerogen samples as a function of heat-treatment temperature, in type II and type III kerogen samples from four organic-rich mudrocks, labeled as A, B, C, and D. Figure 4.3 also shows the Young's moduli of kerogen corrected for the impact of pyrite in all the formations. Micro-CT imaging provided an average initial porosity of 6% in the kerogen packs. Table 4.2 lists volumetric concentrations of pyrite in the kerogen packs from the four formations, estimated using XRF analysis. The relative difference between the initially measured

Young's modulus of kerogen and the one corrected for the impact of residual pyrite is less than 9% in all the cases. Figure 4.4 shows the corrected bulk modulus from the measurements obtained in the isolated and heat-treated kerogen samples. In formation A, the kerogen samples heat-treated to 300ºC and 425ºC exhibit an increase in Young's modulus, compared to the samples heat-treated to 150ºC. In the cases of formations B, C, and D the measured Young's modulus is larger in kerogen samples heat-treated at 425ºC. The increment in Young's modulus could be caused by increase in aromaticity and/or graphitization in the kerogen samples. Hence, I previously acquired transmission electron microscopy (TEM) images in the samples to detect structural transformation in the kerogen pack with increase in thermal maturity (Yang and Heidari, 2016b). **Figures 4.5a** and **4.5b** show transmission electron microscopy (TEM) images acquired from Formation B before and after synthetic maturation, respectively. Figure 4.5a shows a TEM image for a non-heat-treated compacted kerogen pack in which an amorphous structure is observed. Figure 4.5b shows a TEM image for a heat-treated kerogen sample in which short and discontinuous fringes smaller than 3 nm are present. These discontinued structures are basic structural units (BSU) that are composed of aromatic rings, which are evidence of graphitization caused by synthetic maturation. An increase in kerogen graphitization would increase the number of cyclical molecules, which are structurally more stable and therefore, will have higher stiffness compared to molecules with simpler structures and weaker bonds. Graphitization in a material (e.g. carbon alloys) is characterized by low ductility, low resistance to mechanical fatigue, and high brittleness. However, in the case of compacted kerogen samples where the particles are

not molten neither cemented, graphitization could potentially increase the stiffness in heat-treated kerogen due to crystallization which creates a more stable structure.

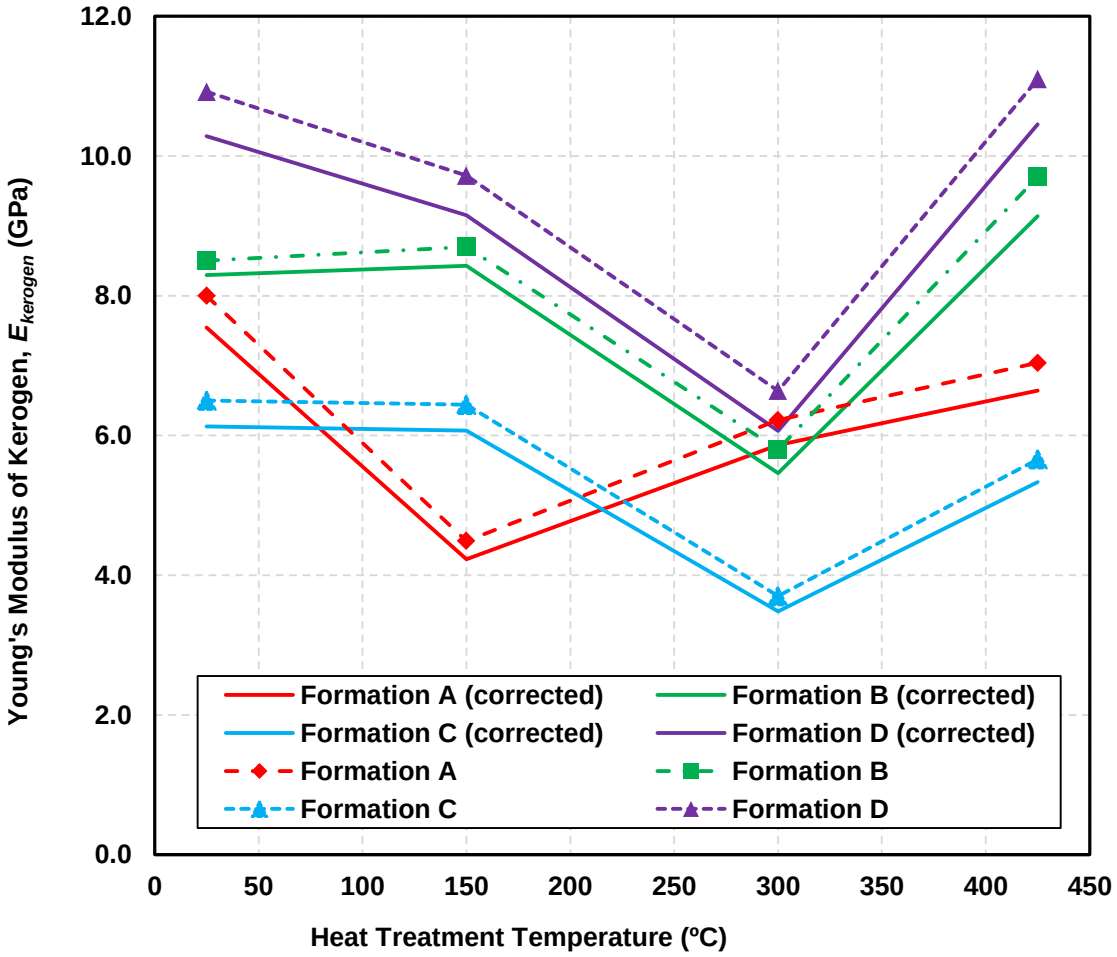

Figure 4.3: Measured Young's modulus $E_{kerogen}$, and corrected estimates in formations A, B, C and D, at room temperature- and in heat-treated samples at 150ºC, 300ºC, and 425ºC. The dotted lines represent measurements obtained via nanoindentation, and the solid lines represent the corrected Young's modulus after synthetic removal of pyrite and replacement with kerogen material.

Table 4.2: Volumetric concentration of pyrite mineral (FeS_2) present in the kerogen packs for formations A, B, C and D quantified via XRF analysis.

Formation ID	Volumetric Concentration of Pyrite (V/V)
A	0.12
B	0.07
C	0.14
D	0.04

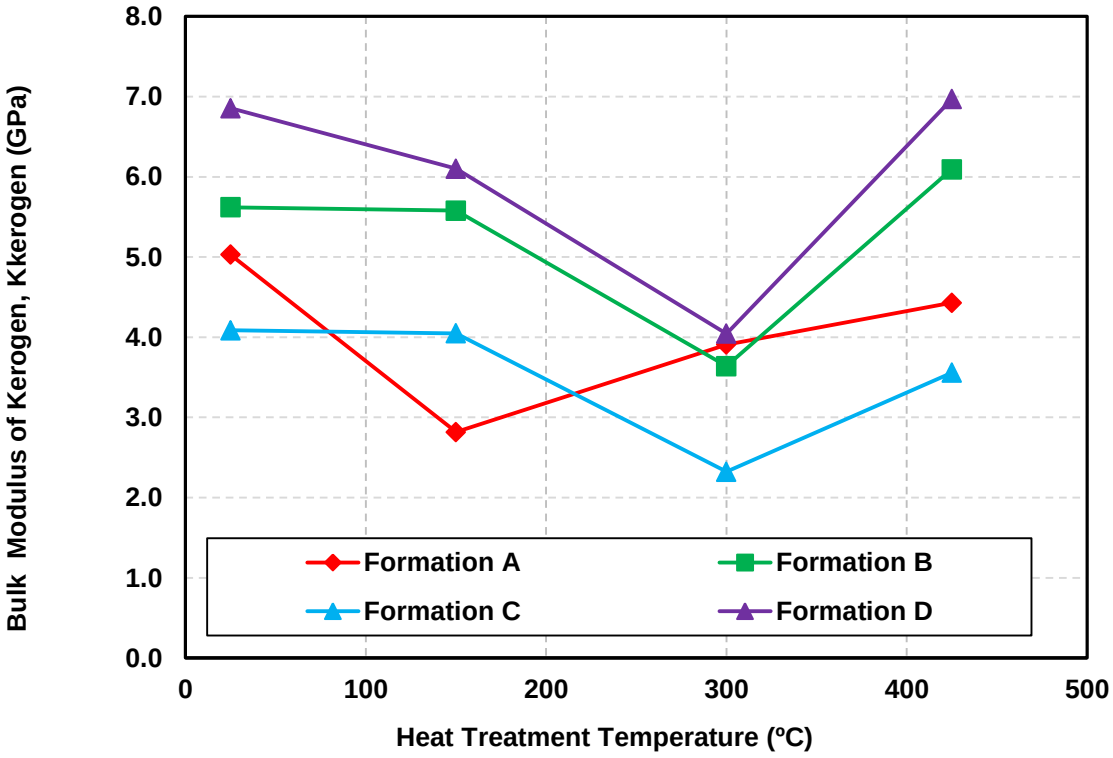

Figure 4.4: Estimated bulk modulus from the measurements performed on the isolated and heat-treated kerogen samples.

For all four formations, the compacted kerogen packs present the lowest Young's modulus at heat treatment temperatures with the highest electrical resistivity, as previously observed by Yang and Heidari (2016a), which are shown in **Figure 4.6**. In formation A, the value of Young's modulus *E* is lower for samples heat-treated to 150ºC, when compared to the values obtained a room temperature. This initial decrease in Young's modulus could be attributed to the loss of moisture due to evaporated water which was previously contained in conductive pathways. Consequently, the highest electrical resistivity is observed at this temperature. After water evaporates, the overburden load P that was previously carried by water and kerogen, is now only carried by kerogen. As a result, the pore space is larger in the contact area A_c, ultimately reducing the bearing capacity and stiffness in the compacted kerogen pack. In formations B, C, and D the measured Young's modulus is the lowest for samples heat-treated to 300ºC.

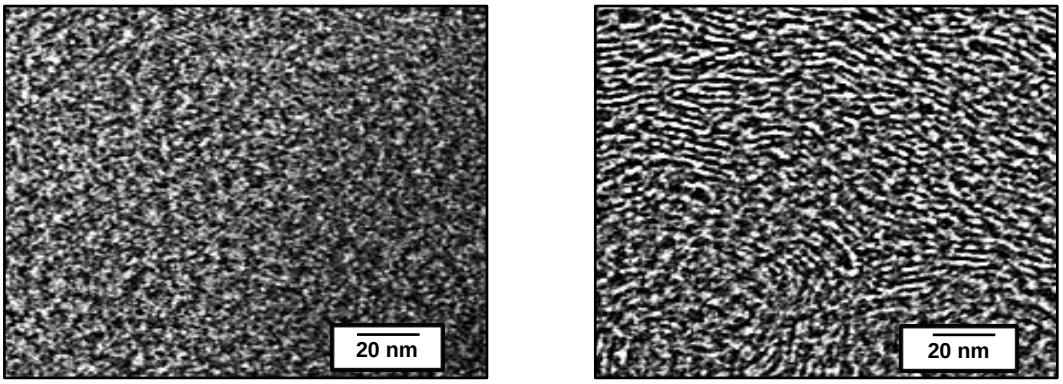

Figure 4.5: TEM images of isolated kerogen before graphitization and after graphitization, representing (a) amorphous carbon structures before graphitization and (b) graphite-like fringes after graphitization has occurred.

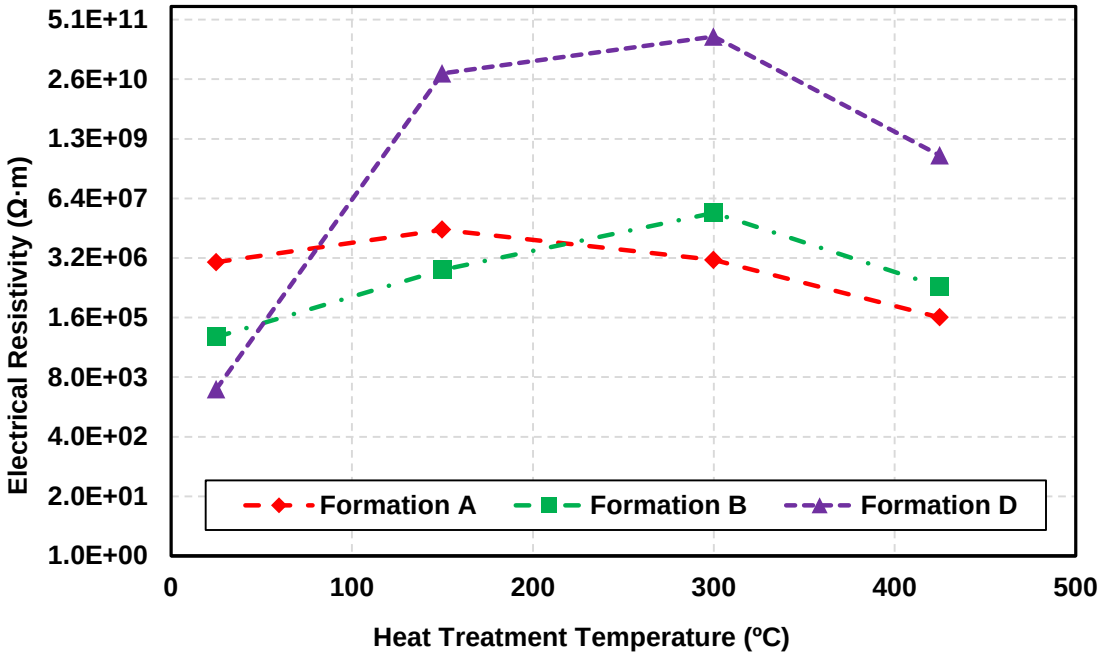

Figure 4.6: Measurements of electrical resistivity in formations A, B, and D, at room temperature, and in heat-treated samples at 150ºC, 300ºC, and 425ºC, as reported by Yang and Heidari (2016). They reported the highest resistivity values at a heat treatment temperature of 300ºC for samples of formations B and D, and at 150ºC for samples of formation A.

4.3.2 Sensitivity analysis: Impact of thermal maturity of kerogen on effective elastic properties of organic-rich mudrocks

I use the data from formation B for quantifying the sensitivity of the estimated elastic properties of the formation to kerogen elastic properties and thermal maturity. This field example presents a laminated mudstone facies, with parallel bedding composed of organic laminae, clay, bioclasts, peloids and detrital calcite. The depth intervals used in this dissertation are clay- and carbonate-rich, with porosity within the range of 1-8.5%, and total organic content of approximately up to 12.5%. I use the well-log-based estimates of mineral concentrations as well as measurements of elastic

properties of individual mineral components and kerogen from nanoindentation tests as inputs to calculate effective elastic properties at well-log domain.

I estimate effective Young's modulus via SCA model in an example from Formation B, at different volumetric concentrations of kerogen and thermal maturity. XRD and TOC analysis indicated that Formation B is composed of illite, chlorite, kerogen and quartz. **Table 4.3** lists the assumed Young's modulus for the aforementioned components, which are used as inputs to the self-consistent approximation model. The elastic properties of minerals are measured via nanoindentation at room temperature.

Table 4.3: Formation B: Young's modulus, *E*, and hardness, *H*, estimated using nanoindentation tests.

Rock Component	***E* (GPa)**
Calcite	71.6±1.1
Illite	13.1±1.1
Illite and Chlorite (intermixed layers)	6.6±1.7
Kerogen (non-heat treatment)	9.3±0.8
Quartz	81.5±2.7

Figure 4.7 shows the variability in estimates of effective Young's moduli in Formation B, obtained via self-consistent approximation. This example uses as inputs elastic properties of kerogen samples (a) measured at initial thermal maturity and (b) heat-treated up to 150ºC, 300ºC, and 450ºC. This sensitivity analysis is performed to

demonstrate the uncertainty in estimates of effective elastic properties of the formation when changes in elastic properties of kerogen due thermal maturity are not taken into account. The variability of elastic properties of kerogen, caused by thermal maturation (i.e. heat-treated kerogen samples), affects effective elastic properties of the formation. The results indicate that a 44% uncertainty in Young's modulus of kerogen (from measurements plotted in Figure 4.3), could affect the estimates for effective Young's modulus of the formation by 22%.

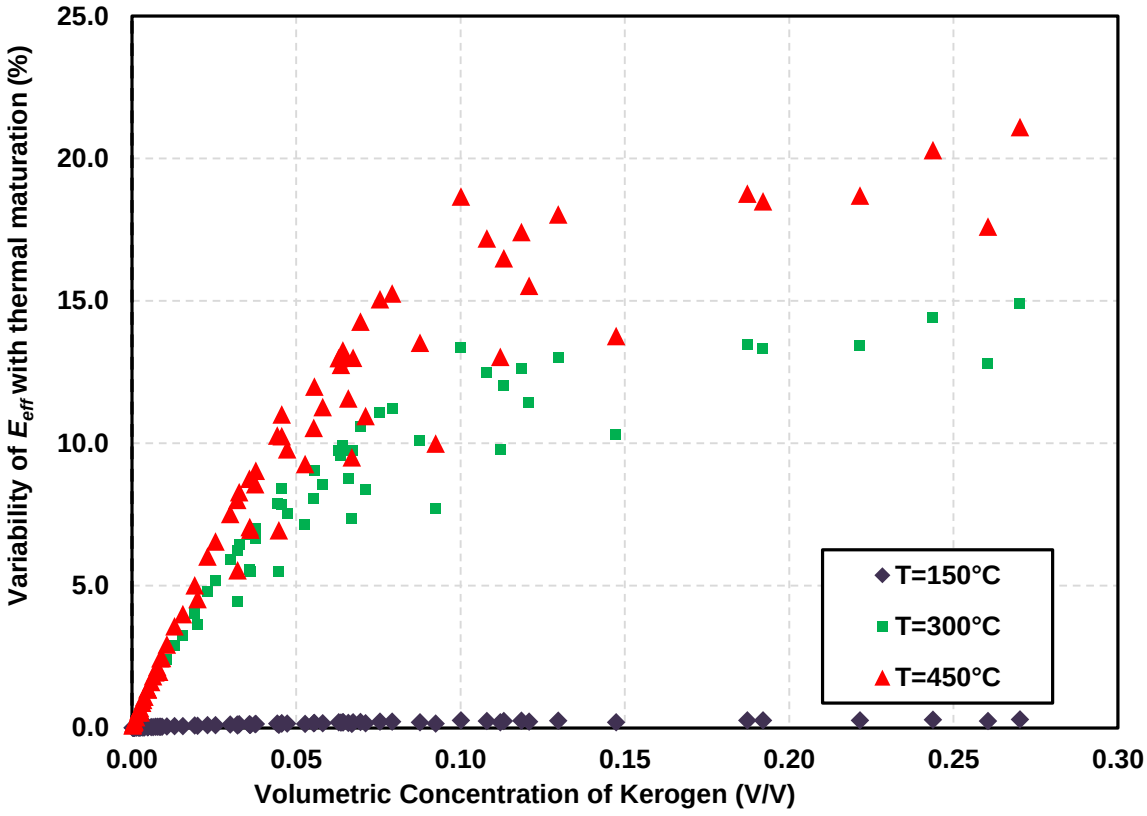

Figure 4.7: Variability of effective Young's moduli estimates using kerogen heat-treated kerogen samples at 150ºC, 300ºC, and 425ºC with respect to estimates performed using kerogen samples at room temperature.

4.4 Conclusions

In this chapter, I performed mechanical tests at the micron-scale level of investigation in compacted kerogen samples and evaluated the impact of thermal maturity on their elastic properties. I isolated and synthetically matured type II and type III kerogen and measured their elastic properties. The results showed that Young's modulus varies with thermal maturation of kerogen, where I observed that the measured values in heat-treated kerogen samples differ from the measurements carried out in untreated kerogen samples. I reported the lowest values of Young's modulus in the heat-treated kerogen samples in which the highest electrical resistivity and hydrogen index were reported. I attributed this behavior to a reduction in conductive pathways due to water evaporation. Consequently, the surface area previously occupied by water molecules will now contribute to the pore space. As a result, the load applied by the indenter tip is only transmitted to the kerogen particles, which results in a reduction of stiffness in the kerogen samples. At higher heat treatment temperatures, the stiffness is overcome due to changes in structures due to aromaticity and graphitization.

I also evaluated the impact of thermal maturity of kerogen in estimates of effective elastic properties of a formation by performing sensitivity analysis. The performed sensitivity analysis suggested that the level of thermal maturation of kerogen can potentially impact effective elastic properties in the formation. Effective Young's moduli of formation B varied up to 15% and 22% when elastic properties of kerogen heat-treated to 300ºC and 450ºC were used as inputs. This variability was more

noticeable at depths with higher volumetric concentrations of kerogen. Furthermore, the variability between estimates of effective elastic properties that used as inputs kerogen samples at room temperatures and heat-treated samples at 150ºC is very small (less than 0.5%).

To summarize, the results that I reported in this chapter enable a better understanding of the effects of thermal maturation of kerogen on its elastic properties. I have shown that measurements of elastic properties isolated kerogen in compacted packs could potentially be used as an alternative to measure elastic properties of kerogen using nanoindentation. Additionally, the elastic properties measured using nanoindentation could help to understand static elastic properties of kerogen at different burial depths and thermal maturation. Furthermore, the variability observed in elastic properties of kerogen caused by thermal maturation can potentially improve well-log-based assessment of rock mechanical properties in formations with high organic content.

CHAPTER V

SUMMARY, CONCLUSIONS AND RECOMMENDATIONS

This chapter summarizes the major contributions of the research that I carried out on the multi-scale characterization of mechanical properties in organic-rich mudrocks.

5.1 Summary

To improve completion design and geomechanical evaluation for stress estimates in organic-rich mudrocks, I investigated the impact of anisotropic poroelasticity in geomechanical evaluation of organic-rich mudrocks. This study evaluated the impact of anisotropic poroelasticity based on: a) mechanical anisotropy and b) vertical heterogeneity. The anisotropic poroelastic parameters were evaluated using laboratory experiments at the core scale and well-log measurements. The stress evaluation was performed using geomechanical analysis in a transversely isotropic media. I applied the described methods to field examples from the lower Eagle Ford, Haynesville, and upper Wolfcamp formations, and exposed the different impact of anisotropy poroelasticity, based on their different degrees of anisotropy and vertical heterogeneity.

I introduced a new technique to address the variability involved in multi-scale estimates of effective elastic properties at the micro-scale, core- scale, and well-log domains. I conducted laboratory mechanical experiments at the micro- and core- scale domains, combined with SEM and EDS analysis, and quantified the impact on the

estimates of effective elastic properties at the well-log domain. I reported that the variability of elastic properties in mudrock components at the micro-scale is associated with location and size of each component within the mudrock. Furthermore, they affect effective elastic properties of the formation at the well-log domain. The method introduced with this technique can help reduce the uncertainties in multi-scale evaluation of effective elastic properties. Furthermore, these techniques can potentially enhance assessment of effective elastic properties at the well-log domain, when core samples are not available, since cutting can be used in nanoindentation tests.

Finally, I investigated the variability of elastic properties of kerogen caused by different degrees of thermal maturation. I heat-treated and conducted experiments at the micro-scale domain of investigation via nanoindentation tests in compacted kerogen samples to observe the variability in their elastic properties. This investigation enables a better understanding of the effects of thermal maturation in the structure and therefore, mechanical properties of kerogen. The measurements of mechanical properties made can help create a compilation of data for elastic properties of kerogen at variable burial depths and thermal maturities. The outcomes from this investigation can also improve well-log-based assessment of effective elastic properties in formations with high organic content.

5.2 Conclusions

The following subsections summarize the conclusions obtained in each chapter of this dissertation.

5.2.1 Impact of anisotropic poroelastic parameters and anisotropic model approximations on stress predictions in organic-rich mudrocks

i. This study presented a technique that uses a reliable workflow to evaluate the effects of anisotropic poroelasticity based on different degrees of mechanical anisotropy and vertical heterogeneity in organic-rich formations. This technique integrates petrophysical, compositional and geomechanical analysis with principles of poromechanics to improve evaluation of stresses.

ii. The workflow executed along this study can improve stress predictions for elastic geomechanical characterization in mudrocks formations, by performing the appropriate evaluation of poroelastic parameters.

iii. This study, compared to previous workflows, includes the effects of Biot's anisotropic parameters of poroelasticity. It also helps to discern whether or not the application of anisotropic poroelastic is adequate for stress estimates.

iv. The workflow presented in this study was applied to field examples from the Haynesville, lower Eagle Ford and Upper Wolfcamp formations. This study quantified the effects of poroelastic parameters. Furthermore, it validates the choice of the VTI approximation models on the estimates of minimum horizontal stresses.

5.2.2 Application of nanoindentation for variability assessment of elastic properties in mudrocks at the micro-scale and well-log domains

i. The multi-scale assessment of effective elastic properties of mudrocks demonstrated that micro-scale experiments can be used to estimate effective elastic properties of mudrocks at the well-log domain.

ii. Nanoindentation experiments, SEM analysis, EDS analysis, and core measurements of elastic properties can be applied in joint well-log based interpretation to estimate elastic properties in mudrocks.

iii. Mechanical tests at the micro-scale can be used to demonstrate the variability in measurements of elastic properties of individual mudrock components, based on their location, size, and adjacent minerals in the formation.

iv. If core samples availability is limited, and only cuttings are recovered at depths object of investigation, micro-scale measurements of elastic properties can be used for mechanical characterization of the formation.

5.2.3 Quantifying the impact of thermal maturation on elastic properties of kerogen

i. The laboratory procedure performed in this study can be used to enhance the understanding of the effects of thermal maturation of kerogen on their mechanical properties. The protocol followed in this study demonstrates the variability caused by different levels of thermal maturation of kerogen caused by changes in moisture and physical structure due to chemical processes.

ii. This study evaluates the relationship between thermal maturation, electrical resistivity and hydrogen index. Electrical resistivity and hydrogen index could potentially be used for initial mechanical characterization of kerogen with thermal maturation.

iii. The results from the experiments performed in this study can be used to evaluate static elastic properties of kerogen at variable burial depths, hence, at different levels of thermal maturation.

iv. This study can be used to improve depth-by-depth well-log based assessment of effective elastic properties in organic-rich formations.

5.3 Limitations of this Research and Future Recommendations

The research that I presented in this dissertation, experimental techniques and the proposed applications withdrawn from this studies could enhance geomechanical analysis in organic-rich formations. The next section displays some limitations found on the presented studies. Furthermore, I provide recommendations that can potentially lead to technical contributions in the line of investigation presented in this dissertation.

5.3.1 Recommendations for the study of the impact of anisotropic poroelastic parameters and anisotropic model approximations on stress predictions in organic-rich mudrocks

i. Development of techniques that enable direct core measurements of Biot's parameters of poroelasticity in mudrocks. Factors such as real-time pore pressure monitoring and fully saturated conditions should be taken into account when developing new experimental technique. These improved measurements can improve geomechanical modelling calibration and therefore, stress prediction.

ii. Inclusion of transient tests such as Diagnostic Fracture Injection Testing (DFIT) in multiple zones of the formation, which inject small volumes of fluid to measure in-situ stresses.

iii. Use of adequate pore pressure prediction models, since it is a source of error in stress estimates when in-situ calibrations are not available.

iv. Incorporation of regional tectonic settings into elastic models for stress prediction could potentially improve stress prediction, since they define horizontal strains that otherwise are not taken into account. Furthermore, laboratory techniques (i.e. anelastic strain recovery and differential strain curve analysis) to obtain orientation of principal stresses should also be incorporated into the analysis.

5.3.2 Recommendations for the use of nanoindentation for the assessment of variability of elastic properties in mudrocks at the micro-scale and well-log domains

i. Post-indentation imaging in a major number of samples could potentially help to enhance the study of variability of elastic properties of individual mudrock components. Collection of more images could help identify further sources of variability of elastic properties of individual mudrock components due to their location within the rock. Furthermore, it is recommended that future work includes nanoindentation measurements from additional formations.

ii. All the nanoindentation experiments were performed in mudrock cutting in "as received" conditions. Similar experiments in the future should include the nanoindentation tests in fully saturated samples. This condition will help to investigate the impact of the presence of fluids in elastic properties of individual mudrock components and poromechanical response at the micro-scale domain.

iii. Incorporation of measurements of elastic properties at the core scale domain. Adding core measurements could help to further investigate and validate estimates and measurements of effective elastic properties of the mudrock at the micro-scale domain.

iv. Nanoindentation experiments in this study were performed perpendicular to the bedding of the formation. Additional experiments should be performed parallel to the bedding to target the interface between layers in layered formations. This could potentially study undesired fracture propagation along thin layers due to drilling vertical wells.

v. Results from nanoindentation experiments could be used as inputs to estimate effective elastic properties at the well-log domain using numerical methods, which could help reduce errors of estimates.

5.3.3 Recommendations for the study on quantifying the impact of thermal maturation on elastic properties of kerogen

i. It is recommended that further experiments are carried out in kerogen samples from additional kerogen types and at additional temperatures. Including additional measurements will increase the knowledge of elastic properties of kerogen at different levels of thermal maturation.

ii. Nanoindentation experiments carried out in this study were made in isolated kerogen samples. Possible sources of error include degree of compaction of the kerogen sample, variability in porosity of the kerogen, which can impact the measurements. Therefore, direct measurements of elastic properties of kerogen lenses within a mudrock sample could help reduce error measurements.

iii. Measurements of elastic properties were performed at room temperature, in previously heat-treated samples. It is recommended that future experiments are performed at desired temperature correspondent to thermal maturation, since it could improve measurements of elastic properties at any given temperature. It will also reduce potential variability in measurements that could be caused by structural changes in the kerogen sample undergone during heating and cooling off stages of the current procedure.

iv. Future development of numerical models to estimate elastic properties of kerogen at variable temperatures can be validated using measurements of elastic properties of kerogen carried out in this investigation.

REFERENCES

Allan, A., Clark, A., Vanorio, T., Kanitpanyacharoen, W., and Wenk, H. 2016. On the Evolution of the Elastic Properties of Organic-Rich Shale upon Pyrolysis-Induced Thermal Maturation. Geophysics 81(3): D263-281. doi: 10.1190/geo2015-0514.1.

Amadei, B., Swolfs, H.S., and Savage, W.Z. 1988. Gravity-Induced Stresses in Stratified Rock Masses. Rock Mechanics and Rock Engineering 21(1): 1-20.

Aranibar, A., Saneifar, M., and Heidari, Z. 2013. Petrophysical rock typing in organic-rich source rocks using well logs: Paper URTeC-1619574 presented at the Unconventional Resources Technology Conference, Denver, Colorado, USA, August12-14.

Berkovich, E.S. 1950. Three-Faceted Diamond Pyramid for Studying Micro Hardness by Indentation. *Zavodskaya Laboratoria* **13**(3): 345-347.

Berryman, J.G. 1995. Mixture Theories of Rock Properties. *Rock Physics and Relations: a Handbook of Physical Constants*. T. J. Ahrens, 205-228. Washington, DC: American Geophysical Union.

Biot, M.A. 1955. Theory of Elasticity and Consolidation for a Porous Anisotropic Solid. *Journal of Applied Physics* **26**(2): 182-185.

Chen Valdes, C. 2013. Characterization of Geomechanical Poroelastic Parameters in Tight Rocks. MS thesis, Texas A&M University, College Station, Texas (May 2013).

Chen Valdes, C., and Heidari, Z. 2016. An Experimental Multi-scale Approach for Assessment of Uncertainty in Elastic Properties of Organic-rich Mudrocks. Presented at the SPWLA 57th Annual Logging Symposium, Reykjavik, Iceland, June 25-29.

Cheng, A. H. 1997. Material Coefficients of Anisotropic Poroelasticity. *International Journal of Rock Mechanics and Mining Sciences* **34**(2): 199-205.

Constantinides, G., Ulm, F-J., and Van Vliet, K. 2003. On the Use of Nanoindentation for Cementitious Materials. *Materials and Structures* **36**(3): 191-196. doi: 10.1007/BF02479557.

De Block, M., Hofmann, A., Rigolet, C., and Ravestein, J. 2015. A new solution for the characterization of unconventional shales resources based on analysis of drill cuttings: Paper SPE-177601 presented at the Abu Dhabi International Petroleum Exhibition and Technology Conference, Abu Dhabi, UAE, November 9-12 .

Detournay, E. and Cheng, A.H. 1993. *Fundamentals of Poroelasticity*: Pergamon Press.

Dix, M.C., Spain, D., Walling, C., Sano, J., Casarta, N., and Richardson, A. 2010. Stratigraphy and Depositional Dynamics of the Haynesville Bossier Sequence: Inferences from Whole Rock Elemental Data: Presented at the Annual Convention and Exhibition, AAPG.

Durand, B., and Nicaise, G., 1980. *Kerogen: Insoluble Organic Matter from Sedimentary Rocks*, Institut Français du Pétrole, Chap. 2, 35-52. Paris: Éditions Technip.

Emmanuel, S., Eliyahu, M., Vanorio, T., Day-Stirrat, R., Hofmann, R., and Macaulay, C. 2016. Impact of Thermal Maturation on Nano-scale Elastic Properties of Organic Matter in Shales. *Marine and Petroleum Geology* **70**: 175-184. doi:10.1016/j.marpetgeo.2015.12.001.

Galford, J., Quirein, J., Westacott, D., and Witkowsky, J. 2013. Quantifying Organic Porosity from Logs. Presented at the SPWLA 54th Annual Logging Symposium, New Orleans, Louisiana, USA, 22-26 June.

Gathier, B. 2008. Multiscale strength homogenization: Application to shale nanoindentation. PhD dissertation, Massachusetts Institute of Technology, Cambridge, Massachusetts, USA.

Giannakopoulos, A. E., and Suresh, S. 1999. Determination of Elastoplastic Properties by Instrumented Sharp Indentation. *Scripta Materialia* **40**(10): 1191-1198.

Hammes, U., Hamlin, H.S., and Ewing, T.E. 2011. Geologic Analysis of the Upper Jurassic Haynesville Shale in east Texas and west Louisiana. *AAPG Bulletin* **95**: 1643-1666.

Hart, J. 2000. Laboratory Measurements of Poroelastic Constants and Flow Parameters and Some Associated Phenomena. PhD dissertation, University of Wisconsin-Madison, Madison, Wisconsin.

Havens, J. 2012. Mechanical Properties of the Bakken Formation. MS thesis, Colorado School of Mines, Golden, Colorado.

Higgins, S., Goodwin, S., Donald, A., Bratton, T., and Tracy, G. 2008. Anisotropic Stress Models Improve Completion Design in Baxter Shale. Presented at the 84th

Annual Technical Conference and Exhibition, Denver, Colorado, USA, 21-24 September. SPE-115736-MS. doi:10.118/115736-MS.

Holt, R. M., Fjaer, E., and Bauer, A. 2013. Static and Dynamic Moduli -So Equal, and Yet So Different. Presented at the 47th U.S. Rock Mechanics/Geomechanics Symposium, San Francisco, California, USA, 23-26 June.

Hornby, B. E., Schwartz, L. M., and Hudson, J. A. 1994. Anisotropic effective-medium modeling of the elastic properties of shales. *Geophysics* **59**(10): 1570-1583.

Horne, S. A. 2013. A Statistical Review of Mudrock Elastic Anisotropy. *Geophysical Prospecting* **61**(4): 817-826.

Katahara, K.W. 1996. Clay mineral elastic properties: Paper presented at the SEG Annual Meeting, Denver, Colorado, USA, November 10-15.

Kinghorn, R.R.F., and Rahman, M. 1980. The Density Separation of Different Maceral Groups of Organic Matter Dispersed in Sedimentary Rocks. *Journal of Petroleum Geology* **2**(4): 449-454. doi: 10.1111/j.1747-5457.1980.tb00972.x.

Kinghorn, R.R.F., and Rahman, M. 1983. Specific Gravity as a Kerogen Type and Maturation Indicator with Special Reference to Amorphous Kerogens. *Journal of Petroleum Geology* **6**(2): 79-194. doi: 10.1111/j.1747-5457.1983.tb00415.x.

Kumar, V., Curtis, Gupta, N. M., Sondergeld, C.H., and Rai, C.S. 2012. Estimation of Elastic Properties of Organic Matter and Woodford Shale Through Nano-indentation Measurements. Presented at the Canadian Unconventional Resources Conference, Alberta, Canada, 30 October- 1 November. SPE-162778-MS. doi: 10.2118/162778-MS.

Mavko, G, Mukerji, T., and Dvorkin, J., 2009. The Rock Physics Handbook Tools for Seismic Analysis in Porous Media. New York: Cambridge University Press, p. 245-264. http://dx.doi.org/10.1017/CBO9780511626753.011.

Mason, J., Curtis, Carloni, J., Zehnder, A., and Jordan, T. 2014. Dependence of micro-mechanical properties on lithofacies: indentation experiments on Marcellus shale: Paper URTeC-1922919 presented at the Unconventional Resources Technology Conference, Denver, Colorado, USA, August 25-27.

Mba, K. C., and Prasad, M., 2010. Mineralogy and its Contribution to Anisotropy and Kerogen Stiffness Variations with Maturity in the Bakken Shales. Presented at the SEG Annual Meeting, Denver, Colorado, USA, 17-22 October. SEG-2010-2612. doi: 10.1190/1.3513383.

Mokhtari, M., Alqahtani, A. A., and Tutuncu, A. N. 2013. Impacts of stress, natural and induced fractures on mechanical properties of organic-rich shales: Paper URTeC-1619158: Paper presented at the Unconventional Resources Technology Conference, Denver, Colorado, USA, August 12-14.

Ortega, J. A., Ulm, F. -J., and Abousleiman, Y. 2010. A Multi-scale micromechanics framework for shale using nano-tools: Paper presented at the 44th U.S. Rock Mechanics/Geomechanics Symposium, Salt Lake City, Utah, USA, June 27-30.

Ostadhassan, M., Zhengwen, Z., and Zamirian, S. 2012. Geomechanical modeling of an isotropic formation bakken case study: Paper presented at the 46th US Rock Mechanics/ Geomechanics Symposium, Chicago, USA, September 23-25.

Pal Bathija, A., Prasad, M., Liang, H., Upmanyu, M., Lu, N., and Batzle, M. 2008. Elastic properties of clay minerals: Paper presented at the SEG Annual Meeting, Las Vegas, Nevada, USA, November 9-12.

Passey, Q.R., Creaney, S., Kulla, J.B. , Moretti, F.J., and Stroud, J.D. 1990. A Practical Model for Organic Richness from Porosity and Resistivity Logs. *AAPG Bulletin* **74**(12): 1777–1794.

Podio, A.L., Gregory, A.R., and Gray, K.E. 1968. Dynamic Properties of Dry and Water Saturated Green River Shale Under Stress. *Society of Petroleum Engineers Journal* **8(**4): 389–404.

Prasad, M., Mukerji, T., Reinstaedtler, M., Bosch, R., and Arnold, W. 2009. Acoustic Signatures, Impedance Microstructure, Textural Scales, and Anisotropy of Kerogen-Rich Shale. Presented at the SPE Annual Technical Conference and Exhibition, New Orleans, Louisiana, USA, 04-07 October. SPE-124840-MS. doi: 10.2118/124840-MS.

Ren, Q., and Spikes, K. 2014. Anisotropic rock-physics modeling for the haynesville shale: Paper presented at the SEG Annual Meeting, Denver, Colorado, USA, October 26-31.

Reuss, A. 1929. Berechnung der Fliessgrenzen von Mischkristallen auf Grund der Plastizitatstsbedingungfur Einkristalle. Z. *Journal of Applied Mathematics and Mechanics* **9**(1): 49–58. doi: 10.1002/zamm.19290090104.

Richin, C. 1995. Effect of Stress Variation on Biot's Coefficient. MS thesis, University of Oklahoma, Norman, Oklahoma.

Romero-Sarmiento, M., J. N. Rouzaud, S. Bernard, D. Deldicque, M., Thomas, and Littke, R. 2014. Evolution of Barnett Shale Organic Carbon Structure and Nanostructure with Increasing Maturation. *Organic Geochemistry* **71**: 7-16.

Savage, W.Z., Swolfs, H.S. and Amadei, B. 1992. On the State of Stress in the Near-Surface of the Earth's Crust. *Pure and Applied Geophysics* **138**(2): 207-228.

Sayers, C.M. 1994. The Elastic Anisotropy of Shales. *Journal of Geophysical Research, Solid Earth* **99**(B1): 767–774.

Sayers, C.M., 2013. The Effect of Kerogen on the Elastic Anisotropy of Organic-Rich Shales. *Geophysics* **78**(2): D65–D74.

Schoenberg, M., Muir, F., and Sayers, C. 1996. Introducing ANNIE: A Simple Three Parameter Anisotropic Velocity Model for Shales. *Journal of Seismic Exploration* **5**(1): 35–49.

Serajian, V., and Ghassemi, A. 2011. Hydraulic Fracture Initiation from a Wellbore in Transversely Isotropic Rock: Paper presented at the 45th ARMA US Rock Mechanics/ Geomechanics Symposium, San Francisco, California, USA, June 26-29.

Shafer, J.L., Boitnott, G.N., and Ewy, R.T. 2008. Effective Stress Laws for Petrophysical Rock Properties. Presented at the SPWLA 49th Annual Logging Symposium, Austin, Texas, 25-28 May.

Shukla, P., Kumar, V., Curtis, M., Sondergeld, C.H., and Rai, C.S. 2013. Nanoindentation studies on shales: Paper presented at the 47th U.S. Rock

Mechanics/Geomechanics Symposium, San Francisco, California, USA, June 23-26.

Smith, M., Yu, G., Yang, W. and Pottorf, M. 2013. Shale Play Characteristics: A Case Study of Eagle Ford Shale. Presented at the 13th International Congress of the Brazilian Geophysical Society, Rio de Janeiro, Brazil, 26-29 August.

Song, L., and Hareland. G. 2012. Minimum Horizontal Stress Profile from Logging Data for Montney Formation of North East British Columbia. Presented at the SPE Canadian Unconventional Resources Conference, Calgary, Alberta, Canada, 30 October-1 November.

Spötl, C., Houseknecht, D. W. and Jaques, R. C. 1998. Kerogen Maturation and Incipient Graphitization of Hydrocarbon Source Rocks in the Arkoma Basin, Oklahoma and Arkansas: A Combined Petrographic and Raman Spectrometric Study. *Organic Geochemistry* **28**: 535-542.

Stow, D.A.V. 1981. Fine-Grained Sediments: Terminology. *Quarterly Journal of Engineering Geology* **14**(4): 243-244.

Suarez-Rivera, R., and Bratton, T. 2009. Estimating Horizontal Stress from Three-Dimensional Anisotropy: U.S. Patent No. 8,175,807.

Suarez-Rivera, R., Herring, S., Handweger, D., Marino, S., Petriello, J., and Stevens, K.. 2013. Integrated Analysis of Core Geology, Rock Properties, Well Logs, and Seismic Data Provides a Well-Constrained Geologic Model of the Bossier/Haynesville System: Paper SPE-167204 presented at the SPE

Unconventional Resources Conference, Calgary, Alberta, Canada, November 5-7.

Thiercelin, M. J. and Plumb, R.A. 1994. Core-based Prediction of Lithologic Stress Contrasts in East Texas Formations. *SPE Formation Evaluation* **9**(4): 251–258.

Vandenbroucke, M. 2003. Kerogen: From Types to Models of Chemical Structure. *Oil & Gas Science and Technology* **58**(2): 243-269. doi: 10.2516/ogst:2003016.

Vernik, L., Liu, X., and Nur, A. 1994. Effect of Kerogen on Velocity Anisotropy in Source Rocks. Presented at the SEG Annual Meeting, Los Angeles, California, USA, 23-28 October. SEG-1994-0323. doi: 10.1190/1.1932086

Vernik, L., and Nur, A. 1992. Ultrasonic Velocity and Anisotropy of Hydrocarbon Source Rocks. *Geophysics* **57**(5): 727-735. doi: 10.1190/1.1443286.

Vyzhva, S. A., Prodayvoda, G. T., and Vyzhva, A. S. 2014. Elastic properties of some clay minerals. *Nafta-Gaz* **70**(11): 743-756.

Westergaard, H. M. 1939. Bearing pressures and cracks. *Journal of Applied Mechanics* **6**(2): A49-A53.

Yan, F., and Han, D.H. 2013. Measurement of Elastic Properties of Kerogen. Presented at the SEG 83th Annual Meeting, Houston, Texas, 22-27 September.

Yang, A. and Heidari, Z. 2016a. An experimental Approach to Quantify the Impact of Kerogen Maturity on its Chemical Aromaticity and Electrical Conductivity. Presented at the SPWLA 57th Annual Logging Symposium, Reykjavik, Iceland, 25-29 June.

Yang, A. and Heidari, Z. 2016b. Experimental Quantification of the Impact of Thermal Maturity on Kerogen Density. Presented at the SPWLA 57th Annual Logging Symposium, Reykjavik, Iceland, 25-29 June.

Yang, A., Firdaus, G. and Heidari, Z. 2016. Electrical Resistivity and Chemical Properties of Kerogen Isolated from Organic-Rich Mudrocks. *Geophysics* 81: D643-D655.

Zargari, S., Prasad, M., Mba, K., and Mattson, E. 2011. Organic Maturity, Hydrous Pyrolysis and Elastic Property in Shales. Presented at the Canadian Unconventional Resources Conference, Alberta, Canada, 15-17 November. SPE-149403-MS. doi: 10.2118/149403-MS.

Zeszotarksi, J.C., Chromik, R. R., Vinci, R.P., Messmer, M. C., Michels, R., and Larsen, J. W. 2004. Imaging and Mechanical Property Measurements of Kerogen via Nano-indentation. *Geochimica Acta* **68**(20): 4113-4119. doi:10.1016/j.gca.2003.11.031.

Zhang, Z., and Jamili, A. 2015. Modeling the Kerogen 3D Molecular Structure. Presented at the SPE Unconventional Resources Conference, Calgary, Alberta, Canada, 20-22 October. SPE-175991-MS. doi: 10.2118/175991-MS.

Wu, T.T. 1966. The Effect of Inclusion Shape on the Elastic Moduli of a Two-Phase Material. *International Journal of Solids and Structures* **2**: 1-8.

APPENDIX A

LIST OF PUBLICATIONS

This appendix cites the articles included in conference proceedings and journal publications that present the research exposed in this dissertation. The articles listed below have been published or are in submission for peer reviewing.

A.1 Journal Publications

Chen Valdes, C., Aderibigbe, A. A., and Heidari, Z. 2015. Impact of Anisotropic Poroelastic Parameters Estimated Using Well Logs and Core Measurements on Stress Prediction in Organic-Rich Mudrocks. *Interpretation Journal* 4(3): T359-T372.

Aderibigbe, A. A., Chen Valdes, C., and Heidari, Z. 2015. Integrated Rock Classification in the Wolfcamp Shale Based on Reservoir Quality and Anisotropic Stress Profile Estimated from Well Logs. *Interpretation Journal 4*(2): SF1-SF18.

Chen Valdes, C. and Heidari, Z. 2017. Application of Nanoindentation for Uncertainty Assessment of Elastic Properties in Mudrocks at the Micro-scale and Well-log Scale. *Geophysics Journal*: Ahead of Print.

A.2 Conference Proceedings

Aranibar, A., Chen Valdes, C., and Heidari, Z. 2014. Well-Log-Based Assessment of Elastic Properties in Organic-Shale Formations. Paper presented at the Unconventional Resources Technology Conference, Denver, Colorado, USA, August 25–27.

Chen Valdes, C. and Heidari, Z. 2014. Experimental Assessment of Elastic Properties and Minimum Horizontal Stress in the Haynesville Shale-Gas Formation. Paper URTEC- 1922664 presented at the Unconventional Resources Technology Conference, Denver, Colorado, USA, August 25–27.

Chen Valdes, C., Aderibigbe, A. A., and Heidari, Z. 2015. Impact of Anisotropic Elastic and Petrophysical Properties on Stress Prediction in Organic-rich Mudrocks. Paper presented at the SPWLA 56th Annual Logging Symposium, Long Beach, California, USA, July 18–22. (Selected for the 2015-2016 SPWLA Distinguished Speaker Program).

Chen Valdes, C. and Heidari, Z. 2016. An Experimental Multi-Scale Approach for Assessment of Uncertainty in Elastic Properties of Organic-Rich Mudrocks. Paper presented at the SPWLA 57th Annual Logging Symposium, Reykjavik, Iceland, June 25–29.

Chen Valdes, C., Gonzalez, A. and Heidari, Z. 2017. Quantifying the Impacts of Thermal Maturity on Elastic Properties of Kerogen. Paper presented at the SPWLA 58th Annual Logging Symposium, Oklahoma City, Oklahoma, June 17–21.